Observations of damping and scattering of low mode internal waves in the ocean

Jonas Löb

Universität Bremen, 2020

Dissertation zur Erlangung des Doktorgrades am Fachbereich 1 Physik / Elektrotechnik der Universität Bremen

Observations of damping and scattering of low mode internal waves in the ocean

von
Jonas Löb

1. Gutachterin: Prof. Dr. Monika Rhein
2. Gutachter: Prof. Dr. Dirk Olbers

Eingereicht am: 13.10.2020
Tag des Promotionskolloquiums: 17.12.2020

Abstract

Internal gravity waves occur everywhere in the stratified ocean and can travel thousands of kilometers away from their generation site during which they transport energy before they break. The breaking of internal waves results in diapycnal mixing which plays an important role in different climate relevant processes such as the transport of heat, freshwater, nutrients, pollutants and dissolved gases. Moreover, understanding the temporal variability of internal waves is necessary to investigate their varying impact on these processes. Long-term observations of energy fluxes of internal waves are sparse. Especially the interpretation of their interactions with mesoscale flow is often based on theoretical and idealized studies or numerical models. It is necessary to investigate how well the temporal variability of in-situ measurements are represented in state-of-the-art global high-resolution ocean tide and circulation models because these models are often not energetically consistent, e.g. they produce mixing without considering the amount of kinetic energy available. This study focuses on the energy flux of internal waves since it is an important benchmark for these models as its divergence identifies sources and sinks of energy. Internal gravity waves can be grouped in different categories depending on their generation mechanism. I investigate the temporal variability of internal waves in the semidiurnal frequency M_2, generated by the barotropic tides flowing over rough topography, and the inertial frequency *f*, generated by wind in a region of high internal wave energy inside a tide beam south of the Azores Islands.

To conduct the measurements, an almost two-year long mooring was deployed which was designed to resolve the characteristics of the first two vertical modes of internal wave energy flux. The results of these in-situ observations were used to analyze changes in the amplitude, direction and coherence of the energy flux, the modal structure of the tide beam, and the impact of several events which occurred during these measurements. The events during the observation period include the presence of surface and subsurface intensified mesoscale eddies on the M_2 internal tide and a strong wind event on the near-inertial (*f*) internal waves. The gathered results of this analyses are compared with energy fluxes derived from a 1/10° ocean global circulation model (STORMTIDE2) and energy fluxes derived from satellite altimetry.

The energy flux of the internal tide derived from observations, model time series and satellite altimetry agree reasonably well in direction, deviations from its fixed phase relationship to astronomical forcing (coherence), and the modal composition. Whereby, model and satellite altimetry underestimate the total energy flux due to high damping or strong temporal and

spatial averaging. Moreover, in-situ observations and the model show a strong spring-neap variability of the energy flux of the internal tide, and all datasets, included the one from the satellite altimetry, are clearly dominated by mode one. Apart from the spring-neap variability, the main temporal variability of the internal tide energy flux in the in-situ observations occurs when an eddy pass by the mooring. Passing surface-intensified eddies damped the energy flux in the first two modes and decreased its coherence, while subsurface eddies decreased the energy flux mainly in the second mode. The energy flux time series of the near-inertial waves is not steady due to its intermittent nature in the forcing and it is neither dominated by mode one or mode two. It shows a peak induced by a distinct strong wind event which is directly linked to wind-power input into the mixed layer north-east of the mooring location, and allows a comparison between the wind event and a background state. Furthermore, indications of non-linear interactions of the near-inertial waves with the internal tides in the form of resonant triad interaction and self-interaction has been found. For the near-inertial waves, the model is underestimating the energy flux compared to the observations but show a similar variability in direction and mode composition.

The observations support the hypothesis that eddy interactions increase the incoherent part of the energy flux and transfer energy from low modes into higher modes which can lead to increased local dissipation. Therefore, it seems inevitable that future ocean models need an energetic consistent parameterization of interactions of internal tides with mesoscale flow to correctly represent the temporal variability of internal waves. In addition, ocean models need a sufficiently resolved of wind input into the mixed layer to adequately represent near-inertial waves during strong wind events. It still remains an open question, how much of the energy converted from lower to higher modes results in local dissipation, a crucial information for creating energetically consistent ocean or climate models. Nevertheless, this study provides a step towards understanding the role of the temporal variability of internal waves for global ocean mixing estimates.

Zusammenfassung

Interne Schwerewellen treten überall im geschichteten Ozean auf und können sich Tausende von Kilometern von ihrem Entstehungsort ausbreiten, wobei sie Energie transportieren bevor sie brechen. Das Brechen interner Wellen führt zu einer diapyknischen Vermischung, die bei verschiedenen klimarelevanten Prozessen wie dem Transport von Wärme, Süßwasser, Nährstoffen, Schadstoffen und gelösten Gasen eine wichtige Rolle spielt. Darüber hinaus ist das Verständnis der zeitlichen Variabilität interner Wellen notwendig, um ihre Auswirkung auf diese Prozesse zu untersuchen. Langzeitbeobachtungen der Energieflüsse interner Wellen sind spärlich. Insbesondere die Interpretation ihrer Wechselwirkungen mit mesoskaligen Strömungen basiert oft auf theoretischen und idealisierten Studien oder numerischen Modellen. Es muss untersucht werden, wie gut die zeitliche Variabilität von lokalen Messungen in modernen globalen hochauflösenden Gezeiten- und Zirkulationsmodellen des Ozeans dargestellt wird, da diese Modelle oft energetisch nicht konsistent sind. Sie erzeugen hierbei zum Beispiel Vermischungen ohne die Menge der verfügbaren kinetischen Energie zu berücksichtigen. Ich konzentriere ich mich auf den Energiefluss interner Wellen, da er eine wichtige Kenngröße für diese Modelle darstellt und seine Divergenz Energiequellen und -senken identifiziert. Interne Schwerewellen können je nach ihrem Erzeugungsmechanismus in verschiedene Kategorien eingeteilt werden. Ich untersuche die zeitliche Variabilität interner Wellen in der halbtägigen Frequenz M_2, die durch barotrope Gezeiten erzeugt werden und in der Nähe der durch Wind generierten internen Wellen nahe der Inertialfrequenz *f*, in einer Region mit hoher interner Wellenenergie innerhalb eines Gezeitenstrahls südlich der Azoren.

Zur Durchführung der Messungen wurde eine fast zwei jährige Verankerung eingesetzt, die die Eigenschaften der ersten beiden vertikalen Moden des internen Wellenfeldes auflösen kann. Die Ergebnisse dieser Beobachtungen wurden verwendet um Änderungen in der Amplitude, Richtung und Kohärenz des Energieflusses, der modalen Struktur des Gezeitenstrahls und die Auswirkungen mehrerer Ereignisse, die während dieser Messungen auftraten, zu analysieren. Zu den Ereignissen während des Beobachtungszeitraums gehören das Auftreten von mehreren mesoskaligen Wirbeln auf die M_2-Gezeit und ein starkes Windereignis auf die internen Wellen in der Nähe der Inertialfrequenz (*f*). Die gesammelten Ergebnisse dieser Analysen werden mit Energieflüssen aus einem 1/10° globalem Ozeanzirkulationsmodell (STORMTIDE2) und Energieflüssen aus der Satellitenaltimetrie verglichen.

Der aus Beobachtungen, Modellzeitreihen und Satellitenaltimetrie abgeleitete Energiefluss der internen Gezeiten stimmt in der Richtung, den Abweichungen von seiner festen Phasenbeziehung zum astronomischen Antrieb (Kohärenz) und der modalen Zusammensetzung relativ gut überein. Wobei Modell- und Satellitenaltimetrie den Gesamtenergiefluss aufgrund hoher numerischer Dämpfung oder starker zeitlicher und räumlicher Mittelung unterschätzen. Darüber hinaus zeigen die Beobachtungen und das Modell eine starke spring-nipp Variabilität des Energieflusses der internen Gezeiten und alle Datensätze, einschließlich des Datensatzes aus der Satellitenaltimetrie, sind eindeutig von der ersten Mode dominiert. Abseits der spring-nipp Variabilität wird die hauptsächliche zeitliche Variabilität des internen Gezeitenenergieflusses in den Beobachtungen festgestellt, wenn ein Wirbel an der Verankerung vorbeizieht. Vorbeiziehende oberflächenverstärkte Wirbel dämpfen den Energiefluss in den ersten beiden Moden und verringern seine Kohärenz, während innere Wirbel den Energiefluss hauptsächlich in der zweiten Mode verringern. Die Zeitreihe des Energieflusses der internen Wellen nahe der Inertialfrequenz ist aufgrund des unregelmäßigen Antriebs nicht konstant und wird weder von der ersten Mode noch von der zweiten Mode dominiert. Sie zeigt einen Spitzenwert, der durch ein ausgeprägtes Starkwindereignis induziert wird, das direkt mit dem Windeintrag in die durchmischte Oberflächenschicht nordöstlich des Verankerungsortes zusammenhängt. Das ermöglicht einen Vergleich zwischen dem Windereignis und einem Hintergrundzustand. Darüber hinaus wurden Hinweise auf nichtlineare Wechselwirkungen der internen Wellen nahe der Inertialfrequenz mit den internen Gezeiten in Form von resonanten Triaden und Selbstwechselwirkung gefunden. Bei den internen Wellen in der Nähe der Inertialfrequenz unterschätzt das Modell den Energiefluss im Vergleich zu den Beobachtungen, zeigt aber eine ähnliche Variabilität in Richtung und Modenzusammensetzung.

Die Beobachtungen unterstützen die Hypothese, dass Wechselwirkungen mit Wirbeln den inkohärenten Teil des Energieflusses erhöhen und Energie von niedrigen Moden in höhere Moden übertragen, was zu einer erhöhten lokalen Dissipation führen kann. Daher scheint es unvermeidlich, dass zukünftige Ozeanmodelle eine energetisch konsistentere Parametrisierung der Wechselwirkungen der internen Gezeiten mit mesoskaligen Strömungen benötigen, um die zeitliche Variabilität der internen Wellen korrekt darzustellen. Darüber hinaus benötigen Ozeanmodelle eine ausreichende Auflösung des Windeintrags in die Oberfläche, um interne Wellen nahe der Inertialfrequenz bei Starkwindereignissen adäquat darzustellen. Es bleibt eine offene Frage, wie viel der Energie, die von niedrigeren in höhere Moden umgewandelt wird, tatsächlich zu einer Erhöhung der lokalen Dissipation führt. Dies ist eine entscheidende Information für die Erstellung energetisch konsistenter Ozean- oder Klimamodelle, nichtsdestotrotz stellt diese Studie einen Schritt zum Verständnis der Rolle der zeitlichen Variabilität interner Wellen zur Abschätzung der globalen Ozeanvermischung dar.

Contents

1 Introduction

The oceans energy balance is driven by numerous different processes which exchange energy between all spatial and temporal scales. These processes are driven by a variety of different sources like the winds, tidal motion, evaporation and precipitation and heat exchange with the atmosphere and thereby supplying energy to the ocean's reservoirs. These reservoirs are among others the general circulation, mesoscale eddies, surface waves but also internal waves. Internal gravity waves are waves in the interior of the ocean which are induced by disturbances of the background stratification and are important for the horizontal and vertical transport of energy. Furthermore, internal waves affect a wide range of various ocean processes on different temporal and spatial scales such as the transport of heat, freshwater, nutrients (e.g. Sharples et al., 2007) pollutants and dissolved gases, underwater sound transmission (e.g. Worcester et al., 2013) and even affect the shape of the ocean floor by influencing sediment transports (Cacchione et al., 2002). Beside these environmental influences, the currents and isopycnal displacements associated with internal gravity waves affect also shipping, underwater navigation, and offshore engineering (Sarkar & Scotti, 2017; Wilson, 2003). It is widely accepted that internal waves provide significant mechanical energy for the abyssal ocean mixing and thereby being a main driver for the global Meridional Overturning Circulation (MOC) (Munk & Wunsch, 1998; Webb & Suginohara, 2001; Wunsch & Ferrari, 2004). The global MOC and the associated climate are sensitive to the magnitude and geography of diapycnal mixing induced by internal wave breaking (Jayne, 2009; Melet et al., 2013; Samelson, 1998; Simmons, Jayne, et al., 2004). Thus, it is important to better understand the generation, propagation and dissipation of internal waves, and it is necessary to study the physics that drives diapycnal mixing, to adequately represent the ocean's role in the climate system and to construct realistic climate models.

1.1 Generation of internal gravity waves

Internal gravity waves occur everywhere in the stratified ocean and are considered as a periodic motion that results from the vertical displacement of water parcels in a stratified environment. They cover a vast range of spatial and temporal scales with (horizontal) wavelengths raging from a few meters to a few hundreds of kilometers. The two restoring forces of internal waves are gravity (downward) and buoyancy (upward) much like a harmonic oscillator. The allowed frequency range for internal gravity waves is between the local inertial

frequency f and the buoyancy frequency N as $f \leq \omega \leq N$ due to the dispersion relation of internal waves using the Boussinesq approximation and the equations of motion (e.g. Olbers, 1983; Olbers et al., 2012). The dispersion relation is:

$$\omega_0^2 = \frac{N^2k^2 + f^2m^2}{k^2 + m^2} = N^2 \cos\theta + f^2 \sin\theta, \qquad [1.1]$$

where ω_0 is the internal wave frequency, k the horizontal and m the vertikal wavenumber. The local inertial frequency f is given by

$$f = 2\Omega \sin\phi, \qquad [1.2]$$

and the buoyancy frequency N^2 is given by

$$N^2 = -g{\rho_0}^{-1}\frac{\partial\bar{\rho}}{\partial z}, \qquad [1.3]$$

with the gravitational constant g, the background density $\bar{\rho}$ and a reference density ρ_0. At locations where the density gradient is small or depth dependent, the constraint of the allowed frequency range implies spatial constraints because it is related to the local stratification. Furthermore, the presence of the Coriolis force due to the earth's rotation leads to a deflection of water parcels which are affected by an internal gravity wave. **Figure 1.1** shows the different dynamic regimes in the oceans as function of wavenumber (space) and frequency (time), ranging from centimeters and seconds representative of small-scale turbulence to thousands of kilometers and years for the global overturning circulation. Mesoscale eddies are defined by length scales of a few tens of kilometers and usually last for several weeks. The internal gravity wave field lies between the large-scale flow and the small-scale turbulence, while spanning scales of four orders of magnitude. The grey box denotes the regimes which can currently be resolved in global ocean general circulation models, which covers only a small part of the internal wave field. In consequence, these small-scale turbulences such as a big part of the internal wave field have to be parameterized in these models.

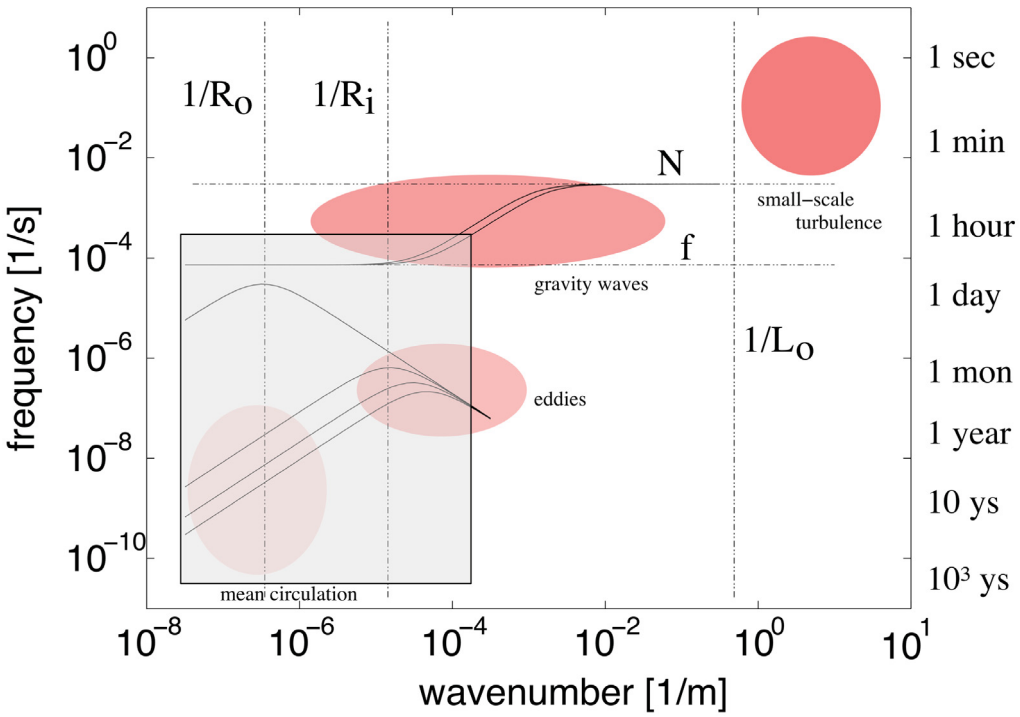

***Figure 1.1**: Schematic of different dynamical regimes in the ocean as a function of wavenumber and frequency. Solid lines display the most important linear wave solutions. Internal gravity waves occur between the Coriolis frequency f and the stability frequency N. The internal R_i or barotropic R_o Rossby radius characterizes the balanced flow at smaller frequencies and on spatial scales. Different solid lines denote different vertical modes or vertical wavenumbers. The Ozmidov scale L_o separates small-scale turbulence from waves. Grey box denotes scales currently covered by non-eddy-resolving or eddy-permitting ocean models. Figure adopted from Olbers et al. (2012) and Eden et al. (2014).*

For frequencies lower than N, the almost purely vertical motion of the parcel changes to an elliptical trajectory and approaches the horizontal inertial oscillation as it accesses the local Coriolis frequency *f* (**Figure 1.2**). Another consequence of the allowed frequency range is that near-inertial waves can only propagate equator ward, towards lower *f*. Poleward propagating waves will be reflected when their frequencies is equal to the local inertial frequency. The angle of the group velocity of internal gravity waves with respect to the vertical depends only on the local Coriolis and the local buoyancy frequency. Furthermore, the wavenumber vector is perpendicular to the group velocity, that means a downward propagating wave has an upward propagating phase (Leaman & Sanford, 1975).

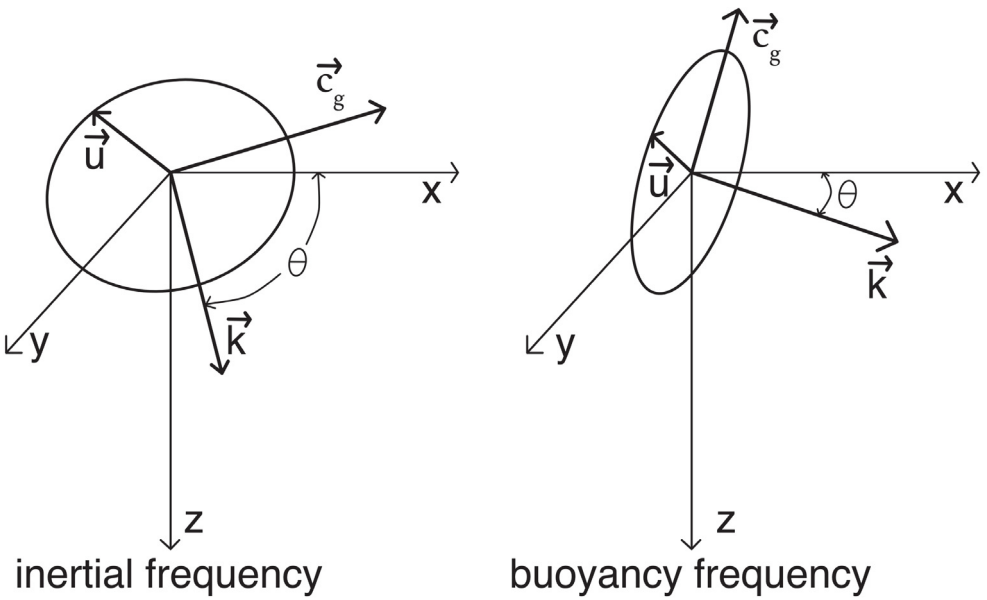

***Figure 1.2**: Wavenumber vector $\vec{k} = (k, m)$, group velocity $\vec{c_g}$, and the hodograph of the particle velocity $\vec{u}(t)$ near the inertial frequency f and the buoyant frequency N. Figure reproduced from Garrett and Munk (1979).*

Internal gravity waves can be grouped in different categories depending on their generation mechanism. The major generation mechanisms are:

- Interactions of the barotropic tide with the bottom topography, inducing internal (baroclinic) tides with tidal frequencies.
- Fluctuating wind stress at the ocean surface, inducing downward propagating, low frequency near-inertial (near the Coriolis frequency f) internal waves.
- Interaction of large-scale currents with the bottom topography, inducing lee waves which provide an upward transport of energy.

A schematic of internal wave processes are illustrated in **Figure 1.3**, where tidal motions are caused by the imbalance between the gravitational pull, which is exerted by the moon or the sun, and the centrifugal forces induces by the rotation of the earth-moon or earth-sun system around their common center of mass. The result are two tidal bulges on opposite sides of the earth (the semidiurnal lunar and solar tides, called M_2 and S_2), which are affected by the shape and tilt of the moon's and earth's orbit as well as by the form the ocean basins. The relative position of the moon to the sun leads to an approximate fortnightly variation in tidal amplitudes, which produces relatively large tide ranges when they are aligned and relatively small tide ranges when they are at right angle (spring-neap cycle). When barotropic tidal currents flow back and forth over rough topography at the seafloor, they cause undulations

in isopycnals that can radiate away as an internal gravity wave with a tidal frequency called baroclinic or internal tide. The different types of topography internal tides can radiate from include isolated features such as islands, ridges and trenches, but also more widespread regions of bottom roughness associated with the sea floor spreading away from mid-ocean ridges (Egbert & Ray, 2001; Garrett & Kunze, 2007). The strength of the barotropic to baroclinic energy conversion is set by the height and the slope pf the topographic obstacle, the barotropic current speed and the stratification (Bell, 1975a, 1975b; Llewellyn Smith & Young, 2002; Sarkar & Scotti, 2017).

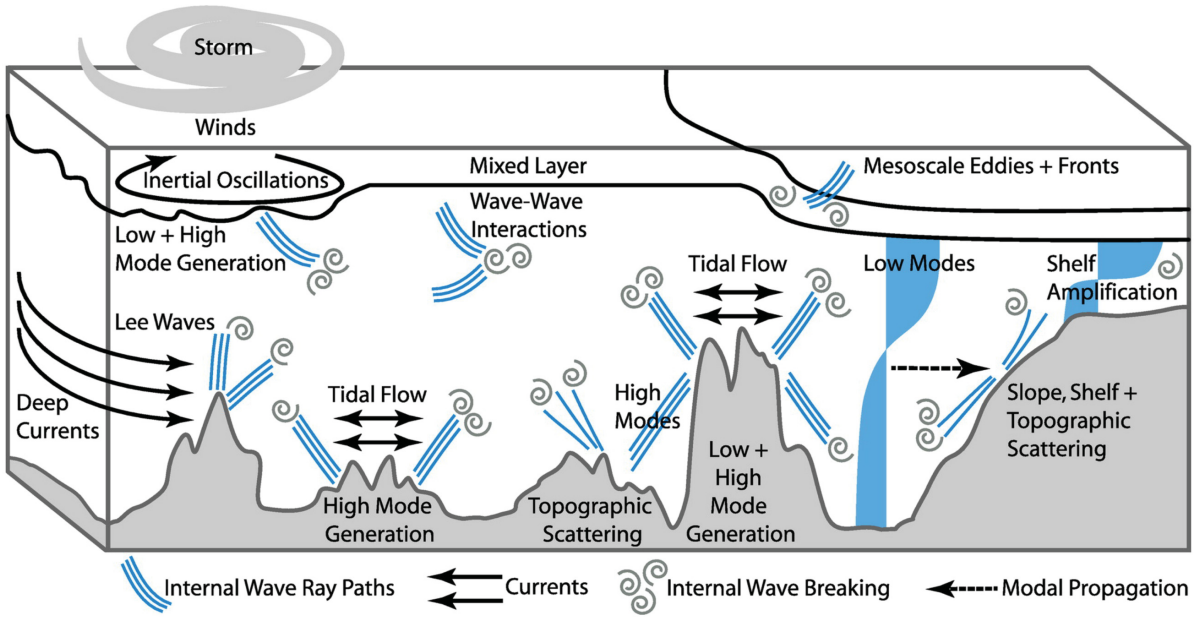

Figure 1.3*: Schematic of internal wave processes in the open ocean. Tides can interact with topographic features to generate high- and low-mode internal tides. Deep currents can generate lee waves by flowing over topography. Storms cause inertial oscillations in the mixed layer, which can generate both low- and high-mode internal waves. Internal waves can scatter off of rough topography and potentially interact with mesoscale fronts and eddies until they ultimately dissipate through wave–wave interactions in the open ocean. Internal waves that reach the shelf and slope can scatter or amplify as they propagate toward shallower water (Schematic taken from MacKinnon et al. (2017)).*

At the ocean surface, wind stress fluctuations can generate resonant inertial motions in the upper ocean, whereby the convergences and divergences of these near-inertial motions lead to pressure gradients at the mixes layer base, which generates internal waves at near-inertial frequency. But not only tides and wind generated near-inertial wavs, but also the mean flow and mesoscale eddies can interact with bottom topography to create internal gravity waves. This process is similar to the generation of internal tides, where the restoring force of buoyancy generates waves when a steady flow is passing over a topographic obstacle in a stratified fluid. This process radiates lee waves away from the sea floor, which transports energy and momentum upward and thus balancing the wave drag on the bottom, induced by

the pressure differences on both sides of the obstacle. Because of the spatially nonuniform deposition of horizontal momentum in the overlying fluid, these radiating lee waves cause near-inertial oscillations, which can in turn force internal gravity waves at frequencies close to the local inertial frequency, providing a secondary wave generation mechanism (Nikurashin & Ferrari, 2010). Other sources of internal gravity waves include the resonant interaction of surface waves (Haney & Young, 2017; Olbers & Eden, 2016), where internal wave motion is triggered by a vertical pumping at the mixed layer base induced by the triad interaction (cf. section 1.2) of two surface and waves and an internal wave, and the spontaneous emission from slow, balanced motion (Vanneste, 2013). In this Dissertation, I focus on the first two categories, the near-inertial internal waves generated by the wind and the semidiurnal internal tide M_2, because they contain most of the energy of the entire internal wave field.

Near-inertial internal waves share several important characteristics with internal tides, however there are some significant differences. Both, near inertial internal waves and internal tides have a comparable power input to them on the global scale (Alford, 2003b; Egbert & Ray, 2000) and therefore a comparable potential to contribute to the ocean variability and turbulent mixing (Alford et al., 2016). They can propagate far away from their generation site before they break (Alford, 2003b; Ray & Mitchum, 1996; Zhao & Alford, 2009). But the generation of near-inertial internal waves is much more intermittent (Fu, 1981), whereby more higher modes can directly be generated (Alford, 2010; Silverthorne & Toole, 2009) and near-inertial waves have a smaller vertical displacement for the same energy as internal tides. Furthermore, near-inertial internal waves have a comparatively slower group velocity which makes them more likely to interact than internal tides which further complicates their propagation path. Moreover, the generation of near-inertial internal waves lies not solely in wind induced disturbances of the mixed layer. Also, nonlinear interactions with waves of other frequencies, lee waves over bottom topography and geostrophic adjustments can generate near-inertial waves, whereby the partitioning among them is yet not fully known, although the wind generated ones are likely the most important. These attributes make near-inertial waves more difficult to observe than internal tides, which might be one of the reason why less is known about them (Alford et al., 2016). Albeit that upper ocean energy is usually predominantly downward and the bulk of the energy leaves wind generation regions in the form of low modes (Alford, 2003a, 2010; D'Asaro et al., 1995; Levine & Zervakis, 1995; Silverthorne & Toole, 2009), there is also a sizeable upward propagating high mode contingent (Alford, 2010). It is unknown whether these waves generate at the surface and are then being reflected from the bottom or if they are directly generated at the bottom via lee waves. Although, these high-wavenumber aspects of the near-inertial frequency band contain little energy compared with that in low modes, they are potentially important for mixing (Alford, 2010; Leaman & Sanford, 1975; Silverthorne & Toole, 2009). But the fact that the bulk of the

energy is in the low modes is important, because these waves can propagate for long distances before they break and can enhance remote mixing.

Away from their immediate generation sites, internal waves in the stratified ocean take the form of standing vertical modes (e.g. Anderson & Gill, 1979). The first baroclinic mode is characterized by a reversal of the horizontal flow direction in the depth of the thermocline while higher modes have a more complicated vertical structure. The phase and group speed of the internal waves decrease with increasing mode number. Low mode (often mode 1-2) motions contain appreciable energy depending on the spectral characteristics of the generating topography (e.g. de Lavergne et al., 2019) and quickly propagate away laterally up to thousands of kilometers from their generation sites, for example the Hawaiian Ridge (Alford, 2003b; Cummins et al., 2001; Dushaw et al., 1995; Nash et al., 2004; Zhao et al., 2016) or the seamount chain south of the Azores (Köhler et al., 2019) and usually do not dissipate locally. Low modes of internal tides are generated at topographic scales of 20 km to 100 km whereas higher modes are generated over rougher topography and dissipate more locally (St. Laurent & Garrett, 2002). Hence, mixing rates induced by internal tides can also show a spring-neap variability (Carter & Gregg, 2002; Klymak et al., 2006) or a tidal cycle (Walter et al., 2010). Higher modes contain much of the vertical shear in the ocean (Simmons & Alford, 2012) and dissipate close to their generation region, also owing to their slower group velocities. Internal tides radiate about 20 % - 80 % of their energy away as low mode internal waves with the remainder being dissipated by near-field tidal mixing (de Lavergne et al., 2019; MacKinnon et al., 2017).

Internal waves are an important link in the closure of the energy budget of the ocean circulation because they transport energy over both large physical and wavenumber scales. Satellite altimetry data show that a total of about 3.5 TW of barotropic tidal energy is dissipated in the ocean, which contains approximately 2.5 TW from the M_2 tide, and that about 25-30% of this dissipation occurs in the deep ocean. The remainder of the tidal energy dissipates through bottom friction in shallow seas and is therefore not available for deep ocean mixing (Egbert & Ray, 2000). Approximately 2 TW are needed to maintain the abyssal stratification of which internal tides contribute the main share, about 0.5 to 1.5 TW (Munk & Wunsch, 1998; Nycander, 2005; Waterhouse et al., 2014; Wunsch & Ferrari, 2004). The global conversion rate from barotropic to baroclinic tidal energy is estimated to be about 1 TW globally, which happens mainly over continental slopes, midocean ridges, and seamounts (Baines, 1982; Egbert & Ray, 2000; Morozov, 1995). For the share of the global wind energy input, several model studies tried to create different approximations (e.g. Alford, 2001, 2003a; Furuichi et al., 2008; Jiang et al., 2005; Rimac et al., 2013; Simmons & Alford, 2012; Watanabe & Hibiya, 2002). The obtained results range from 0.3 to 1.5 TW, but seems to be strongly dependent on the spatial and temporal resolution of the wind products used (Jiang et al.,

2005; Rimac et al., 2013). Typhoons and Hurricanes are thought to contribute an additional 10 % to these estimates (Alford, 2001; Alford et al., 2016). This is the same order of magnitude as estimates of the global power input from baroclinic M_2 tides, suggesting that wind generated near-inertial waves play a similarly important role in the global energy balance. Estimates for the global energy conversion from geostrophic motions (mean flow and eddies) into lee waves range between 0.2 to 0.75 TW (Nikurashin & Ferrari, 2011; Scott et al., 2011; Wright et al., 2014). However, all these estimates remain a challenge since their results show a large spread with wide errors and that the available data products are a significant source of uncertainty for estimates of internal gravity wave energy.

A relatively universal description of the energy spectrum in internal gravity waves was provided by Garrett and Munk (1972) and is widely used as a representation of the internal wave spectrum. They combined the available observations of that time into a spectral model (GM model or GM spectrum) for a horizontally isotropic and vertically symmetric wave field. Away from immediate internal wave sources the GM spectrum can be seen as an adequate but smoothed representation of the internal gravity wave field in the deep ocean. This suggest a universality of at least some of the dominant forcing mechanisms. But temporal and spacial characteristics of the internal wave field are shown to vary strongly due to local properties and different times. Therefore, the shape of the internal wave field in frequency and wavenumber space can differ significantly, for example the local buoyancy frequency influences the slope of the continuum spectrum (van Haren et al., 2002) and also the variation of the wind induces changes in the spectrum and can imprint a seasonal cycle with a maximum in winter (Alford, 2003a; Alford & Whitmont, 2007). The universal shape of the GM spectrum away from immediate generation sites is the result of resonant interactions between internal waves. These interactions redistribute internal wave energy and cause the relatively smooth internal wave spectrum.

1.2 Propagation and Interaction of internal gravity waves

After internal waves are generated they can undergo various propagation and interaction processes. These processes lead to a propagation of energy in wavenumber space towards smaller scales until the wave breaks which causes vertical mixing and dissipation. When internal waves travel through the ocean they radiate energy and momentum which changes the density field around them. These distortions, also called vertical displacements, can reach up to some hundred meters, depending on the local stratification and the energy of the internal wave. When Internal tides propagate through the ocean, they imprint a signature on

the sea level which is on the order of several centimeters, but do not necessarily maintain a fixed phase relation with the astronomical forcing (Ray & Zaron, 2011). Deviations from this phase relation are defined as incoherence. Internal tide incoherence is attributed to both modulations in the stratification at the generation sites (Kelly & Nash, 2010; Zilberman et al., 2011) and interactions between propagating internal tides and background variations of the low-frequency circulation (Chavanne et al., 2010; Rainville & Pinkel, 2006). In the first mechanism, the internal tide generation may vary in time with the tidal forcing due to local changes in the stratification and/or remotely generated incoherent internal tides (Kerry et al., 2014, 2016; Nash, Kelly, et al., 2012; Pickering et al., 2015). In the second mechanism, the associated spatial and temporal variability in stratification, currents and vorticity may cause time-variable refractions of the internal gravity wave field when internal tides propagate (Dunphy & Lamb, 2014; Kelly & Lermusiaux, 2016; Kelly et al., 2016; Park & Watts, 2006; Ward & Dewar, 2010; Zaron & Egbert, 2014). Incoherent tidal motions have already been observed in coastal tide gauge records by Munk et al. (1966), but also in velocity and density records from moorings (Ansong et al., 2017; Kelly et al., 2015; Nash, Kelly, et al., 2012; R. Stephenson Jr. et al., 2015; van Haren, 2004; Wunsch, 1975; Zaron & Egbert, 2014; Zilberman et al., 2011) and satellite altimetry (Ray & Zaron, 2011; Zaron, 2017; Zhao et al., 2016), whereby globally up to 44 % of the total semidiurnal internal tide signal is incoherent (Zaron, 2017). Satellite altimetry does not easily allow estimations of the incoherent tidal amplitude because of their sampling times, in contrast to eddy-resolving numerical models with realistic forcing (Kerry et al., 2014; Savage et al., 2017; Shriver et al., 2014; Zaron & Egbert, 2014). These models show that close to the generation site, the internal tides are mostly coherent, and they become more incoherent as they propagate away.

Another aspect which is important for the propagation of internal waves are critical layers. There are two types of critical layers with different responses of the internal waves. First, internal waves can reach a depth where its frequency is equal to the local buoyancy frequency N. Here, the vertical wavenumber and the group velocity c_g approaches zero and the internal wave is reflected or can even be trapped, when in the local buoyancy frequency profile, a local maximum is reached. Second, when the group velocity c_g of the internal waves is equal to the velocity of the geostrophic mean current. Here, the intrinsic frequency ω_0 will decrease when an internal wave group propagates through an increasing background velocity field and can even reach $\omega_0 = f$. Then the vertical wavenumber tent to infinity and the group velocity goes towards the horizontal velocity. This effect depends on the Richardson number of the background flow and can either enhance or absorb the internal waves (Jones, 1968; Munk, 1981). Here critical layers act like a valve, which allows waves approaching from one direction to penetrate into the critical layer, while waves approaching from the opposite direction are absorbed (Olbers, 1981).

When internal waves radiate away from their generation site, they can transfer energy to waves of other frequencies via wave-wave interactions, interactions with fronts, eddies, or topography and ultimately deposit their energy in form of turbulent mixing. The strength of the mixing induced by the breaking of internal waves depends on the energy in the internal wave field. Interactions between internal waves, mesoscale eddies and currents are inevitable because of the large distance that low mode internal waves are able to propagate. This makes a significant fraction of the internal wave field unpredictable because these interactions can modify propagation directions, adjust propagation speeds, change the coherent fraction of the energy flux, lead to wave deflection and increase dissipation (Alford, Mickett, et al., 2012; Kelly & Lermusiaux, 2016; Kelly et al., 2016; Nash, Shroyer, et al., 2012). The presence of mesoscale eddies is assumed to be the main driver of temporal variability in the energy contained in the internal wave field apart from the changes in the energy of the internal tide that are induced by the spring-neap cycle in its forcing (Ponte & Klein, 2015; Whalen et al., 2018; Zaron & Egbert, 2014). Mesoscale eddies often have a barotropic or mode 1 baroclinic vertical structure (McWilliams, 1985) and their length scale, typically in the order of 100 km (Eden, 2007; Krauss et al., 1990) is comparable to that of the low mode internal waves.

This makes them a potential partner for interaction according to the resonant triad theory where the eddy contains energy at the required wave number to complete resonant triads between mode 1 and mode 2 internal tides (Olbers, 1976). The result might be an enhancement of the energy cascade, represented by a downscale transfer of energy into higher modes which increases the local dissipation at the expense of less dissipation at remote locations. The non-linear resonant triad interaction of internal waves can occur if their frequencies and wavenumbers underlay the conditions of resonant interactions:

$$\omega_1 = \omega_2 \pm \omega_3, \qquad \overrightarrow{k_1} = \overrightarrow{k_2} \pm \overrightarrow{k_3}. \qquad [1.4]$$

These interactions can be grouped in three different processes: the induced diffusion, the elastic scattering and the parametric subharmonic instability (McComas & Bretherton, 1977) and are seen in **Figure 1.4**. In the case of the induced diffusion (**Figure 1.4** a), a wave with a high frequency/high wavenumber interacts with a wave of low frequency/low wavenumber. The wave with the high frequency/high wavenumber propagates through a shear-field whose scales are much larger than the wave packet which induces a diffusion of the wave action along constant horizontal wavenumbers k and in the direction of increasing vertical wavenumbers m. During this process the energy interacts with the wave that has a low frequency/low wavenumber and the energy is not conserved. In the case of elastic scattering (**Figure 1.4** b), a high-frequency wave is scattered by a low-frequency wave at the near-inertial

frequency with about twice the vertical wave number. A wave with almost the opposite vertical wave number is induced. For all but near-inertial frequencies, this results in an almost balanced vertical energy transport. Furthermore, this also means that if an asymmetry in vertical energy propagation is observed at higher frequencies, the source of these waves must be in close proximity. In the case of the parametric subharmonic instability (**Figure 1.4** c), energy is transferred from a wave with low wavenumber to two waves with higher wavenumber but with half of the frequencies of the first wave. This process primarily generates waves with near-inertial frequencies with a high wavenumber because the internal wave action is distributed almost equally along the three waves.

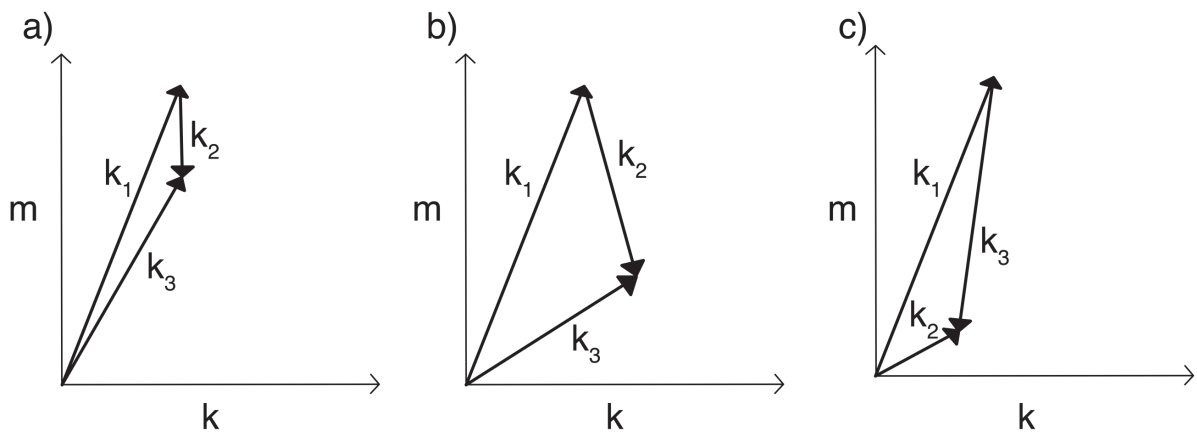

Figure 1.4: *Wavenumber vectors for resonant triad interaction. a) induced diffusion, b) elastic scattering, c) parametric subharmonic instability. The ratio m/k corresponds to a fix frequency ω following the dispersion relation for internal gravity waves. Figure adopted from (Garrett & Munk, 1979)*

Another form of interaction undergoes internal waves which are propagating in strong mean currents $\vec{u}$. This can result in a doppler shift of the internal wave and changes the internal wave frequency such that the intrinsic frequency ω_0 is given by

$$\omega_0 = \omega - \vec{u}\vec{k}. \qquad [1.5]$$

1.3 Global maps of internal gravity waves

Global maps of modeled and observational energy flux provide further insight on major generation site of near-inertial internal waves and internal tides. **Figure 1.5** shows a global map of the depth integrated near-inertial energy flux from the Generalized Ocean Layer Dynamics (GOLD) model (blue arrows) together with mooring observations (red arrows)

(Alford, 2003b; Simmons & Alford, 2012). It displays the long-range swell of internal waves generated by ocean storms and show strong inputs in the western portion of the ocean basins in mid latitudes with peaks in winter (inset **Figure 1.5**). This confirms that the bulk of the wind work onto the mixed layer comes indeed from midlatitude storms. The general distribution of wind work also matches closely the observed near-inertial energy in the mixed layer from observations with drifters (Chaigneau et al., 2008). The general direction of the model energy flux is equatorward, whereby within the area of enhanced wind work between 30°S and 60°S the energy propagates to the west, in the opposite direction to the weather systems. The spatial distribution of the annual mean wind work follows closely the common storm tracks. The wind work in the southern Hemisphere is about a factor of two stronger than in the norther Hemisphere (Simmons & Alford, 2012).

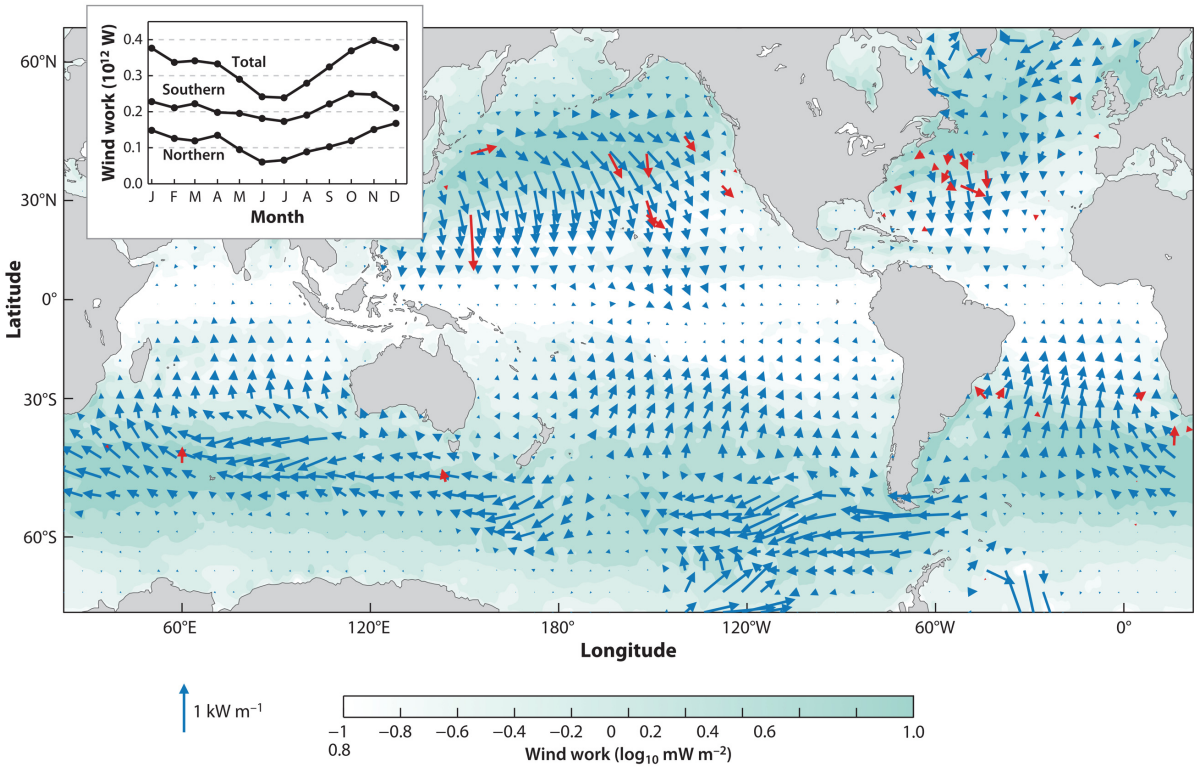

***Figure 1.5**: Modelled (blue arrows) and observed (red arrows) horizontal mode 1 energy fluxes. Inset shows the hemispherically and globally integrated wind work computed from the GOLD model. The background color shows the annual-mean distribution of the wind work, illustrating the enhancement under storm tracks. Figure taken from Alford et al. (2016), modified from Simmons and Alford (2012).*

The global maps of the mode 1 internal tide from the STORMTIDE model in **Figure 1.6** (M. Müller et al., 2012) and from satellite altimetry in **Figure 1.7** (Zhao et al., 2016) show that M_2 internal tides are ubiquitous in the world oceans and that they are geographically inhomogeneous. Strong generation regions of internal tides have been identified in barotropic tide divergence (Egbert & Ray, 2000), linear theory (Nycander, 2005), and numerical models

(e.g. Arbic et al., 2010; Simmons, Hallberg, et al., 2004). The main generation regions are steep ocean topography such as the Hawaiian Ridge, Tahiti, the Macquarie Ridge, the seamount chain south of the Azores Islands and the Luzon Strait or the Walvis Ridge. Although internal tides are generated over most submarine topographic features, few strong generation sites account for the bulk of the global internal tide generation (Simmons, Hallberg, et al., 2004). In general, the energy flux decreases from their generation sources. Relatively quiet regions are the eastern equatorial Pacific Ocean, the Southern Ocean, the equatorial Indian Ocean as well as the Labrador and Nordic Seas.

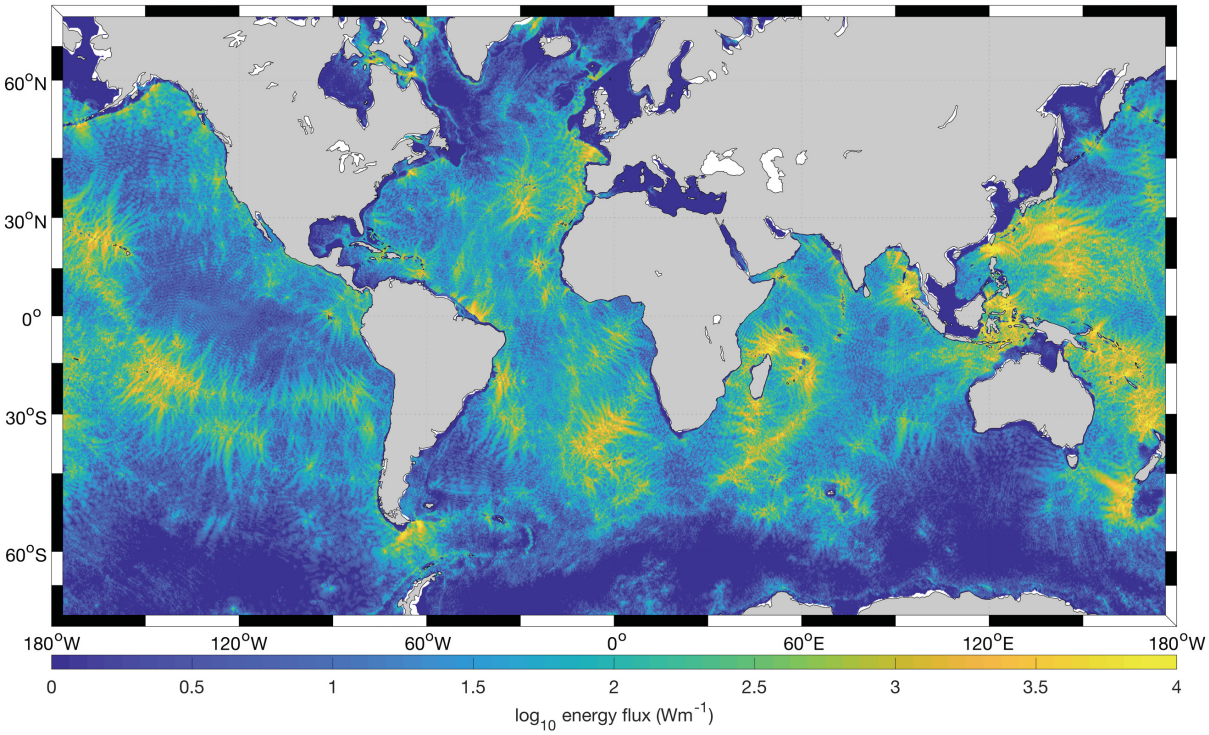

***Figure 1.6**: Global mode 1 M_2 internal tide from the STORMTIDE model (Müller 2012). The main generation sites are over steep ocean topography, and agree with the main generation sites from satellite altimetry (**Figure 1.7**). Whereby few strong generations regions account for the bulk of the global internal tide generation.*

The main generation regions of internal tide energy flux inferred from satellite altimetry agrees with the results from the STORMTIDE model but, due to the coarser resolution of the altimetry data, they show a more smeared picture. Here the black areas mask regions where due to high mesoscale activity (eddies) the tidal signal cannot be correctly separated from the sea surface height signal, and white areas are methodically excluded due to the insufficient satellite coverage or a too steep topography. The detection of internal tides via satellite altimetry is further limited by the loss of coherence. A comparison of mode 1 and mode 2 internal tides via satellite altimetry shows that their generation hot spots do not always overlap with each other and that their propagation directions can be different. This suggest

that the internal tide generation is complicated and the multimodal distribution varies spatially (Zhao et al., 2016).

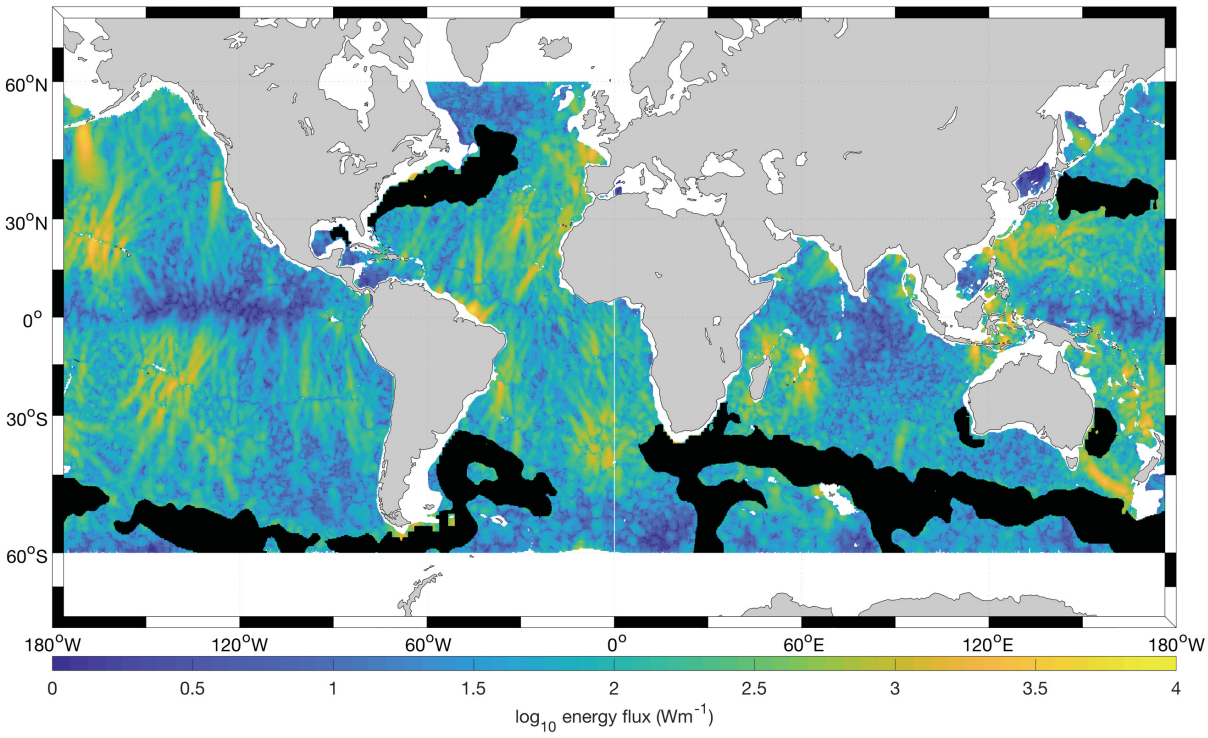

***Figure 1.7**: Global mode 1 M_2 internal tide inferred from satellite altimetry (Zhao 2016). The main generation sites are over steep ocean topography, and agree with the main generation sites from the STORMTIDE model (**Figure 1.6**). Black areas masks regions with high mesoscale activity (Eddies) where the detection of mode 1 energy flux via satellite altimetry cannot be performed. White areas are methodically excluded by either the detectability of the internal tide signal from the satellite or by a too steep topography.*

Global maps of internal tides reveal that the interference pattern of internal tides can form beam like structures. In these beams the phase of the internal tides increases linearly with their propagation. Most of the globally observed internal tide beams do not spread much with propagation and their widths are typically in a range of 100-300 km. Only few beams spread radially in propagation which is usually associated with point generation sources (Zhao et al., 2016). Several internal tide beams travel across the ocean basin and reach the opposite continental slopes. This implies a dissipation on the continental slope or a loss of coherence when they refract of a fraction of the internal tide energy (Alford & Zhao, 2007a, 2007b; Nash, Kelly, et al., 2012). On global average, the M_2 internal tide dissipates within 400 km (from satellite data in Zhao et al. (2016)), some long-range internal tide beams can transport the tidal energy over 3000 km. Mode 2 beams of internal tides are shorter and narrower than mode 1 beams. Hence, mode 2 waves rarely reach the opposite continental slope and with satellite altimetry mode 2 beams can be tracked for O (100 km) (Zhao, 2018).

1.4 Modelling of internal gravity waves

The modelling of fluid dynamical systems is one of the most commonly used techniques in modern geophysical research. With increasing computational power, there are numerous ways to set up and run simulations, also with the implementation of internal gravity waves (Griffies et al., 2000). Thereby many decisions about the model have to be made, like the complexity of the physics, the horizontal, vertical and temporal resolution or the implementation of parameterizations of unresolved processes below the grid size (Griffies, 2004; Haidvogel & Beckmann, 1999). This results in a big variety of different models with different strengths to answer various scientific questions. Whereby some models focus on very specific problems, ocean general ocean circulation models (OGCMs) try to simulate the ocean as close as possible to nature. When these models are used to simulate time series of decades to millennials in a global setup they are often called climate models and are usually used for climate predictions like in the Intergovernmental Panel on Climate Change (IPCC) reports. The understanding of ocean processes, such as the propagation and dissipation of internal waves, which are often too simply parameterized in numerical ocean models, is necessary in order to make these models energetically more consistent. Up to now ocean models are for the main part not energetically consistent, e.g. they produce mixing without considering the amount of kinetic energy available (Eden et al., 2014). The energy flux is an important benchmark for these models because its divergence identifies sources and sinks of energy. Up to now, it is still a challenge to observe and realistically include internal tides in ocean general circulation models (OGCMs) and the implementation of near-inertial waves is even more rare. High-resolution concurrent simulations of circulation and tides have become an important tool to study internal tides in the ocean. This has been done for example with the GOLD model (Simmons, Jayne, et al., 2004; Waterhouse et al., 2014), the 1/12.5° HYCOM model (Arbic et al., 2012; Arbic et al., 2010), the MITgcm (Savage et al., 2017), and with the 1/10° MPIOM (STORMTIDE) (Z. Li et al., 2015, 2017). While the MITgcm (e.g. Kelly, 2019) and the successor of STOMRTIDE, STORMTIDE2 also include near-inertial internal waves. It is furthermore necessary to investigate how well such models are able to simulate internal wave energy fluxes. Theoretical and idealized studies, as well as in-situ studies with a regional focus are the main source of information regarding internal wave energy fluxes and their temporal variability. When comparing pointwise observations with models, the complex interference patterns of baroclinic energy fluxes of multiple waves needs to be considered.

1.5 Dissertation overview

The observation of internal waves is a challenging task for several reasons. First, mode 1 internal waves have a wavelength between 100-200 km with higher modes having shorter wavelengths. In addition, with their rich vertical modal structures a high vertical and horizontal resolution is required to quantify internal waves. Second, the usual occurrence of internal waves by different sources are forming a complicated interference pattern which makes it difficult to interpret point-wise measurements (Terker et al., 2014). Third, the internal wave field is temporally variable because the generation and propagation of internal waves are affected by ocean parameters such as stratification, currents and mesoscale eddies, which vary over time (Mitchum & Chiswell, 2000; Nash, Kelly, et al., 2012; Zaron & Egbert, 2014; Zilberman et al., 2011).

Several studies have been carried out to investigate the spatial and depth distribution of internal wave energy (e.g. Alford et al., 2006; Dushaw et al., 2011; Garabato et al., 2004; Hendry & Charnock, 1977; Jayne & St. Laurent, 2001; Köhler et al., 2019; Kunze et al., 2002; Nikurashin & Ferrari, 2011; Polzin et al., 1997; Scott et al., 2011; Wunsch, 1975; Zhao, 2018; Zhao et al., 2016) but beside seasonally and tidally induced changes most knowledge about the temporal variability of internal waves comes from theoretical studies or idealized models because of few in-situ measurements due to their expensiveness and logistical difficulties.

In this study I investigate the temporal variability of the energy flux within a tide beam south of the Azores using in-situ observations. The temporal and directional variability of the energy flux of internal waves as well as the variations of its modal composition and its coherence with barotropic forcing (only internal tides) are studied and compared to their representation in a state-of-the-art ocean model and satellite altimetry. The issues that arise are:

- How does the temporal variability of internal waves look like in a tide beam? What is the main driver of the temporal variability and how does its characteristics change over time?
- How important are single events (eddies, storms) in comparison to the temporal mean of the energy flux of internal waves at the study site?
- How well are the in-situ measurements represented in global datasets of internal wave energy fluxes in a state-of-the-art OGCM and data from satellite altimetry?

The seamount chain south of the Azores, which has been earlier identified by Köhler et al. (2019), is considered to be one of the main generation sites for internal tides in the North Atlantic (M. Müller et al., 2014; Zhao et al., 2016). To answer those key questions, I analyze the interactions of surface and subsurface intensified eddies present in the observational record with the semidiurnal internal tide energy flux calculated from mooring measurements, and study the impact of a strong wind event onto the near-inertial internal waves. Furthermore, I compare how well the global datasets of M_2 internal tide energy fluxes from STORMTIDE2 and satellite altimetry represent the results of our direct in-situ measurements. STORMTIDE2 is a global 1/10° resolution ocean general circulation model (OGCM) with realistic wind and tide forcing.

This work was carried out in the framework of an integrated effort to improve the energy cycle in climate models (DFG CRC181, Energy Transfers in Atmosphere and Ocean). The dissertation is structured as follows: In chapter 2 I introduce the data sets used in this study which are the mooring observations, the STORMTIDE2 model and measurements of internal tide energy fluxes using satellite altimetry. In chapter 3 the methods used to analyze these datasets are explained. Thereafter, I present the temporal variability of the energy flux of internal tides in chapter 4 with a special focus on the interaction of internal tides with mesoscale eddies. In chapter 5 the temporal variability of near-inertial waves with a special focus on a strong wind event in compare to a background state is presented. In chapter 6 I evaluate how well the results of the in-situ measurements are represented in the STORMTIDE2 model and in satellite altimetry. A summary of the results and the conclusions are presented in chapter 7.

2 Data

In the following section I present all dataset used for the analysis of the temporal variability of internal wave energy fluxes. First, I present the mooring, deployed in a tide beam, which gives the foundation of all analyses in this work followed by a presentation of the model STORMTIDE2. STORMTIDE2 is a state-of-the-art global 1/10° resolution ocean general circulation model (OGCM) with realistic wind and tide forcing whose principals are also used in coupled climate models. It is used to analyze how the energy flux in strong generation regions of internal tides is representing the in-situ measurements. Afterwards, I introduce the internal tide energy flux data derived from satellite altimetry.

2.1 Mooring

The location of the in-situ measurements was chosen based on considerations regarding the importance of different aspects of the propagation of internal tides. The seamount chain south of the Azores Islands offers excellent conditions to study internal tides (**Figure 2.1**). Beside the strong baroclinic tides in this region, it has relatively low wind variations, the seafloor south of the seamounts is relatively flat, the eddy variability is low and beside the Azores current there are no known large-scale currents in this area. The Azores Current is part of the subtropical North Atlantic gyre and originates near the Great Banks of Newfoundland where the Gulf Stream splits into the northern branch becoming the North Atlantic Current (NAC) and the eastward flowing Azores Current (B. Klein & Siedler, 1989). The Azores Current whose main share continues between the Azores Islands and the seamount chain south of the Azores is not to be expected to play a major role in the in-situ measurements. The further absence of larger ocean currents and the relatively constant wind conditions help to avoid possible intrusions of near-inertial internal waves and internal lee waves onto the internal tide spectrum and reduces possible misinterpretations of the internal tide energy even when the Coriolis frequency is about two times the M_2 frequency at this latitude, $f \approx 2M_2$. Steady wind conditions generated by the Trade Winds in this region, with usually few storm events per year and coming from north-east direction, are assumed to generate weak near-inertial internal waves in compare to the amplitude of the internal tides in this region. A flat seafloor is an important boundary condition to treat internal waves as a superposition of discrete standing vertical modes. In contrast to studies with idealized models where the seafloor can easily set as flat, the seafloor in reality is never totally flat. Therefore, the steepness of the

seafloor always needs to be considered when analyzing in-situ measurements by modal decomposition. Furthermore, a low eddy activity in this area leads to fewer biases regarding the propagation of internal tides, at the same time a clear allocation of the eddy effect onto the internal tide spectrum is expected if an eddy is present. The exact position of the mooring was chosen based on maps of low mode internal tide energy flux from the STORMTIDE model (M. Müller et al., 2012) and from satellite altimetry (Zhao et al., 2016). At this location the internal tides generated from the seamounts northern from the mooring location form a strong beam-like structure in south-west direction due to the interference pattern of different waves from different places.

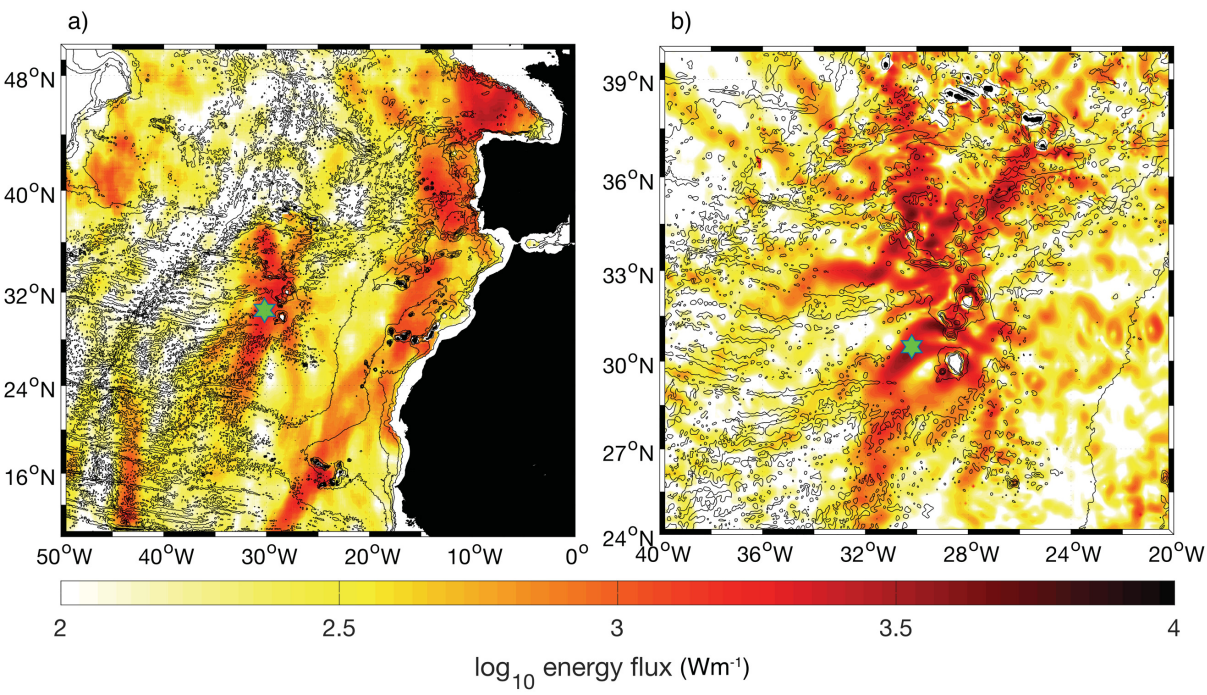

***Figure 2.1**: Mooring position in relation to mode 1 internal tide energy flux derived from satellite altimetry (a) and the STORMTIDE2 model (b) south of the Azores Islands denoted by the green star. Black contour lines represent the bathymetry contoured every 1000 m. The seamount chain south of the Azores are a major generation site for internal tides in the North Atlantic and offer very good monitoring conditions.*

The first phase of the mooring (ET-1) was deployed at 30.4840°N and 30.1950°W on 8 August 2017 during a research cruise with the German research vessel R/S Poseidon with the number POS516 (Walter et al., 2018) and recovered on 10 May 2018. The mooring was redeployed in a second cruise with the same research vessel as ET-2 on 18 May 2018 at 30.4893°N and 30.1977°W during POS523 (Walter et al., 2019) and recovered on 29 March 2019 during the cruise POS533/2 (Köhler & Löb, 2019). This results in a total of 20 consecutive months of in-situ mooring measurements. The distance between the two deployment periods is about 600 m. Because they are so close to each other and significant shifts in the water properties

between the two places are not to be expected. They can be considered as one time series with two deployment periods at the same location.

The mooring layout was designed to resolve mode 1 and mode 2 of the internal wave energy flux (Nash et al., 2005). A comprehensive list of all instrument pairs with their corresponding depth, sampling interval and sampling accuracy is given in **Table 2.1**. The ET-1 mooring was equipped with three Seabird SBE56 temperature loggers, five Sea-Bird SBE39plus temperature loggers, an upward looking 150 kHz Teledyne RD Instruments (TRDI) Quartermaster acoustic Doppler current profiler (ADCP) and seven Nortek Aquadopp current meters. The ET-2 mooring was equipped with an additional current meter (TRDI Doppler Volume Sampler, DVS) which had to be removed from the calculations because of unknown uncertainties during post-processing. The eight temperature loggers measured with a sampling interval of one minute, the ADCP and current meters recorded horizontal and vertical velocity with a sampling interval of 10 minutes. The blank distance of the ADCP was 3.5 m, with the first bin being 12.3 m, and all consecutive bins having a length of 8 m.

The given accuracies of the velocity sensors (**Table 2.1**) are a compromise between the sampling interval of the measurements and the battery life for each instrument, whereby for the ADCP also the bin length needs to be taken into consideration. Hereby, the focus on the instrument setting was strongly influenced by the resulting accuracies with the sampling interval being chosen as small as possible without simultaneously worsening the resulting accuracy. The lower accuracy of the ADCP was compensated by averaging the five bins closest to the instrument during the calculation process. This is possible by considering each bin of the ADCP as individual measurements. The resulting accuracies are sufficient enough to extract the baroclinic signal necessary to calculate internal wave energy fluxes by modal decomposition. The expected horizontal velocities are in the order of few centimeters per second, and the expected vertical velocities are in the order of few millimeters per second. The temporal resolution of the measurements is an important factor by resolving the internal tide and near-inertial frequencies of the internal wave spectrum. The difference in the sampling interval between temperature and velocity sensors are not important and are both sufficient enough for this approach. The temporal resolution necessary to resolve the internal wave signals depends on the frequency of the wave measured. According to NASH 2005, the minimum temporal resolution to extract an unbiased semidiurnal energy flux estimate can be computed from 4 measurements over 12 hours (every 3 h). In general, one can say that the higher the sampling accuracy and the lower the sampling interval the better, but these factors strongly depend on the available batterie capacity of each instrument.

The depths of the individual instruments changed slightly between the two deployment periods to have a better resolution close to the surface during the second deployment period. The vertical mooring motions were small with a maximum displacement over the entire

deployment period of 51 m, and typical values between 10 m and 20 m in a period of about 6 hours. The resulting velocities from these mooring motions are usually less than 1 mm s^{-1}, because of these relatively low velocities induced due to the weak mooring motions further corrections of the velocity data seem not necessary.

#	Instrument type	Depth during ET-1 (m)	Depth during ET-2 (m)	Sampling interval (min)	Sampling accuracy	Mean zonal velocity (m s^{-1})	Mean meridional velocity (m s^{-1})	Mean temperature (°C)
1	ADCP	335	130	10	± 1.2 cm s^{-1}	-0.014	-0.019	
	SBE56			1	± 0.002 °C			17.374
2	Current meter	609	550	10	± 5 mm s^{-1}	-0.016	-0.019	
	SBE56			1	± 0.002 °C			12.567
3	Current meter	1027	960	10	± 5 mm s^{-1}	-0.006	-0.018	
	SBE56			1	± 0.002 °C			8.757
4	Current meter	1426	1370	10	± 5 mm s^{-1}	-0.004	-0.013	
	SBE39plus			1	± 0.002 °C			6.340
5	Current meter	2053	1995	10	± 5 mm s^{-1}	-0.009	-0.011	
	SBE39plus			1	± 0.002 °C			4.065
6	Current meter	2889	2840	10	± 5 mm s^{-1}	-0.007	-0.005	
	SBE39plus			1	± 0.002 °C			2.906
7	Current meter	3729	3670	10	± 5 mm s^{-1}	-0.005	-0.002	
	SBE39plus			1	± 0.002 °C			2.544
8	Current meter	4566	4510	10	± 5 mm s^{-1}	-0.004	0.000	
	SEB39plus			1	± 0.002 °C			2.462

***Table 2.1**: Instrument pairs of current and temperature sensors, their depth, sampling interval, sampling accuracy, mean zonal and meridional velocities and mean temperatures used at ET-1 mooring location 30.4840°N, 30.1950°W and ET-2 mooring location 30.4893°N, 30.1977°W. SBE56 and SBE39plus: temperature loggers. Current meters: Acoustic current meters from Nortek. ADCP: 150 kHz Teledyne RD Instruments Quartermaster. The given accuracy and sampling intervals are sufficient enough to calculate internal wave energies by a modal decomposition.*

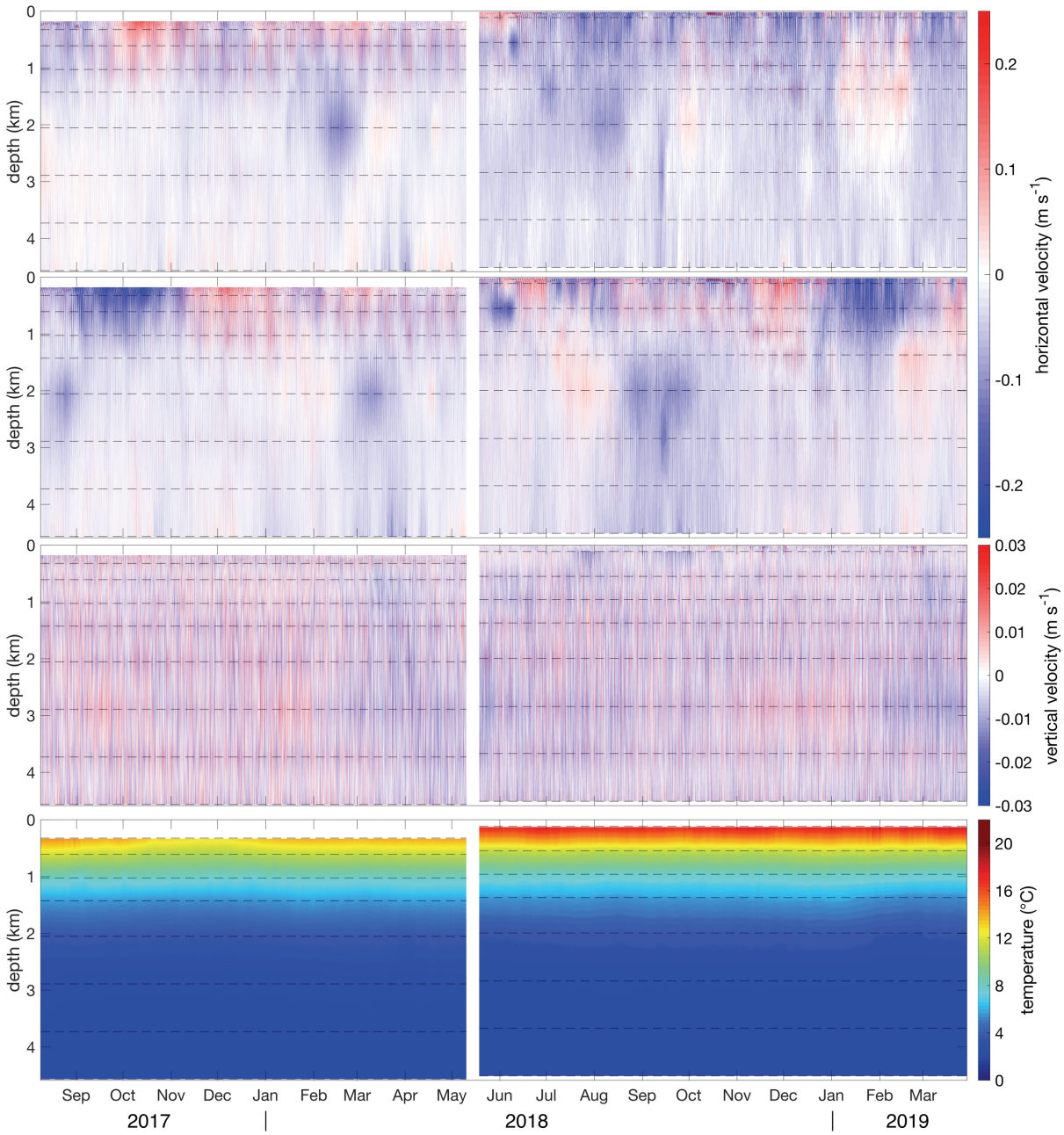

***Figure 2.2**: The time series of horizontal (upper panel u component, second panel v component) and vertical velocities (third panel), and temperature (lowest panel) of the in-situ measurements south of the Azores, display a striped picture as well indications for the presence of mesoscale eddies. Dashed lines represent instrument depths.*

The raw data of the velocity and temperature time series measured by the instruments attached to the mooring are shown in **Figure 2.2**. There are some prominent features that can be observed, for example a striped picture in the data as well indications for the presence of mesoscale eddies. The striped picture in the velocities data is most visible in the vertical component, but can also be seen in the horizontal component and in the temperature data. It suggests a semidiurnal cycle, likely generated by the tides, which seems to be the dominant

factor in the temporal variability in these variables. The time series of the horizontal velocities shows in the upper part of the water column an enhancement in the beginning of the measurements. The flow direction of these enhanced velocities is changing over time, which is an indicator for the presence of a surface intensified mesoscale eddy. During the remainder of the time series this pattern is repeated another three times. Two times in the interior of the ocean - at a depth between 2000 and 3000 m, and another one at the surface, indicating further eddies during the deployment of the mooring. The observed horizontal mean velocities show relatively low values in southwest direction and do not imply a strong mean current in this region (as expected beforehand). In this area the density profile is dominated by temperature, with salinity playing a minor role. The mean temperature profile of 11 repeated CTD (Conductivity Temperature Depth instrument) casts close the mooring location, together with the resulting stratification profile is shown in **Figure 2.3**. This data reveals a mixed-layer depth of about 37 m, defined here as the maximum of $\frac{\partial T}{dz}$. More details about these features will be discussed in the following chapters.

2.2 STORMTIDE2 model

A run of an ocean circulation model which has the skill to simulate low mode internal tides and near inertial waves was created to answer a variety of different research questions in the framework of the Collaborate Research Centre 181 (CRC181). The available model output is used to compare the energy flux and its variability from the in-situ observations to understand how well the in-situ observations are represented in a numerical state-of-the-art ocean model. For this, the STORMTIDE2 model was used, which is a successor of the STORMTIDE simulation (M. Müller et al., 2012). It is a global high-resolution ocean tide and circulation model with an embedded thermodynamic sea-ice model. STORMTIDE2 is forced by the full lunisolar tidal potential to excite the generation of tides, therefore hundreds of tidal constituents are explicitly taken into consideration and the resultant energy flux is expected to show a spring-neap variability. It has 40 unevenly distributed vertical layers ranging from 10-70 m (in the uppermost 500 m) to 500-600 m (in the deep ocean), and a horizontal nonsymmetric tripolar spherical grid with an almost uniform resolution of 0.1° that is about 10 km at the equator. It has two poles in the northern and one in the southern hemisphere. Consequently, the grid size decreases toward the south pole, whereas it remains more or less uniform north of the equator. A climatological forcing is used as a surface forcing for the spin up period of 33 years until the ocean reaches a quasi-equilibrium state. It is then switched to 6-hourly wind forcing (from National Centers for Environmental Prediction Clime Forecast System, NCEP) at the ocean surface instead of the climatologic wind forcing used in

STORMTIDE. The model was integrated for the years 1981-2012 and the temporal resolution of the output used for the calculation is one hour.

For reasons of available memory space and high computational costs, only four month of model data could be saved with this temporal resolution. The saved variables in the model output are the three velocities components (*u,v,w*), temperature, and salinity. I analyzed the four months of the model data output of the last simulation year (2012), where I considered one month per season, to cover possible seasonal changes, especially in the mixed layer. The different years between model output and in-situ observations have an influence on the comparability, especially in the near-inertial band but lesser for the internal tides. I use statistical properties of the energy flux which can be compared between model and the in-situ observations, since the underlying numerical principals remain the same, even when both datasets do not cover the same time period. The comparability between in-situ measurements and STORMTIDE2 is further examined in chapter 6.

A subsampling of the vertical model layers towards the number of current meters in the mooring is not expected to significantly change the resultant energy flux calculations compared the full resolution (Ansong et al., 2017). The model is capable to resolve low mode internal waves: a comparison between the co-tidal charts from STORMTIDE2 and the global tide model TPXO9, as well as between the mean temperature (*t*) and the stratification profiles (N^2), used for the energy flux calculations from STORMTIDE2 and the in-situ observations is shown in **Figure 2.3**. TPXO is a series of fully-global models of ocean tides and offers complex amplitudes of sea surface elevations and transport/currents for primary, long period and non-linear harmonic constituents. Here, the 1/6° resolution tidal model TPXO9 (Egbert & Erofeeva, 2002) is used. One can identify higher amplitudes in the M_2 barotropic tide of STORMTIDE2 compared to TPXO9 especially at the seamounts south of the Azores, which are strong conversion regions of barotropic to baroclinic energy. The strong barotropic velocities in these regions in STORMTIDE2 can be connected with the relatively high resolution of the model, which simulates higher tidal velocity over high narrow ridges and high small-scale seamounts than a lower resolution model does. It might be possible, due to the lower resolution of TPXO9, that the barotropic velocities in regions with rapidly-changing and small-scale topography are underestimated in TPXO9 (von Storch, pers. comm.). Furthermore, a too weak conversion rate from barotropic to baroclinic energy of STORMTIDE2, together with too strong dissipation, could lead to an underestimation of the low mode internal tide energy flux, even when the barotropic tide is strong.

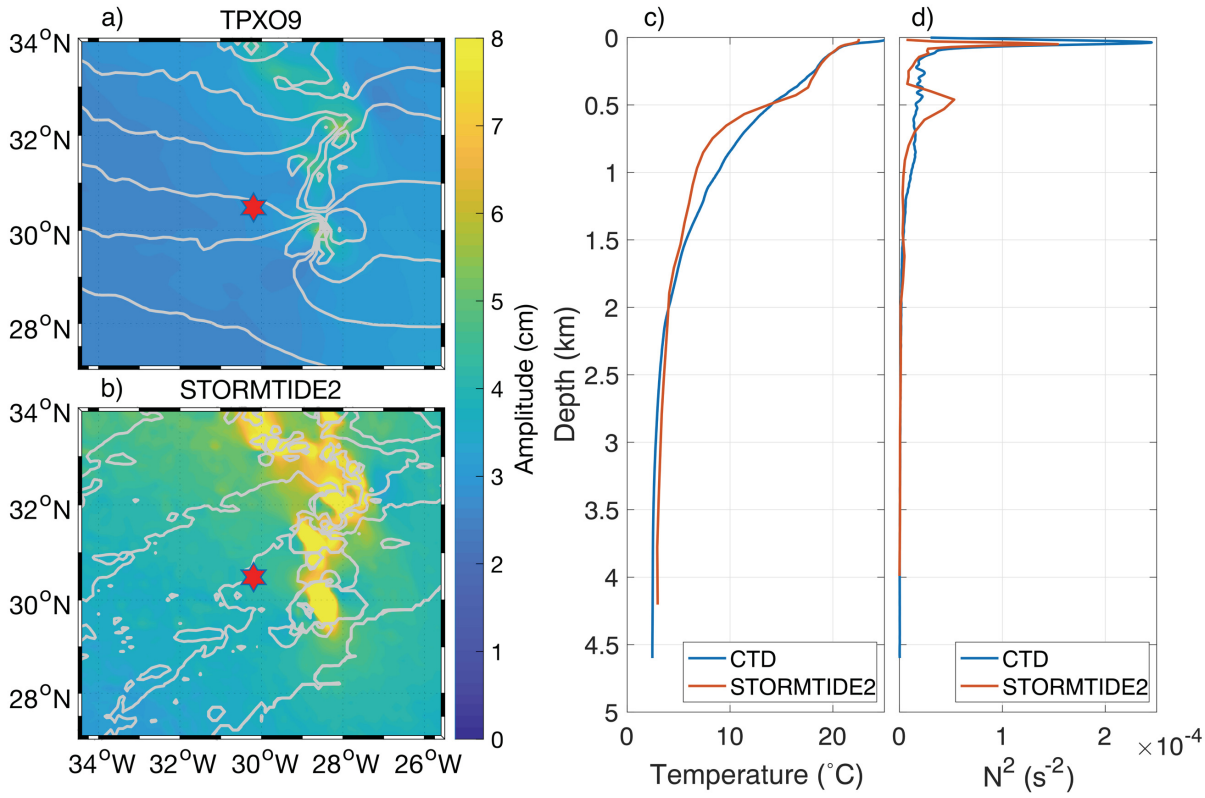

***Figure 2.3**: Co-tidal charts of a) TPXO9 and b) STORMTIDE2, and mean profiles of c) temperature and d) stratification. Grey contour lines in a) and b) represent the phase of the amplitude in 5° steps; red stars indicate the position of the mooring.*

The difference in the amplitude between STORMTIDE2 and TPXO9 at the mooring location is about 1.3 cm, which is still a reasonable value for the open ocean. The phase of the M_2 barotropic tide is in good agreement with TPXO9. The comparison of the mean temperature and stratification profiles between in-situ measurements from CTD (Conductivity Temperature Depth sensor) and STORMTIDE2 (**Figure 2.3** c, d) confirms a realistic realization of the in-situ observations by the model. The differences in the stratification should have a negligible impact when comparing vertically integrated energy fluxes from STORMTIDE2 with mooring results.

2.3 Energy flux from satellite altimetry

The relative sparse in-situ observations of internal tides can partly be compensated by their observation from satellite altimetry by the detection of their centimeter-scale sea surface height (SSH) fluctuations (Munk et al., 1965). Satellite altimetry provides a technique to observe global internal tides from space (Ray & Mitchum, 1996). Earlier estimates of internal tides by satellite altimetry, where the global distribution of the M_2 internal tide energy is

integrated to 50 PJ (Kantha & Tierney, 1997), lack information on the internal tide's spatial propagation such as phase, horizontal propagation direction and energy flux. These quantities are included in the studies performed by Zhao et al. (2016) and Zhao (2018). The general problem of observing internal tides by satellite altimetry lies in the coarse sampling in time and space, and by the complex nature of the global internal tide field. These issues have been addresses by developing a two-dimensional plane wave fit method (Ray & Cartwright, 2001; Zhao & Alford, 2009; Zhao et al., 2011), but one problem remains, only the coherent component can be considered as in all other satellite altimetric internal tide products (Dushaw et al., 2011; Egbert & Ray, 2017; Kantha & Tierney, 1997; Ray & Cartwright, 2001; Ray & Zaron, 2015). Therefore, the observation of internal tides by satellite altimetry can only complement in-situ observations.

Global maps of internal wave energy fluxes in the semidiurnal M_2 band for the first and second mode were obtained from satellite altimetry by Zhao et al. (2016) and by Zhao (2018). To obtain the energy fluxes, expressions of Sea Surface Height (SSH) from multiple altimeter satellites, namely the European Remote Sensing Satellite 2 (ERS-2 (E2)), Envisat (EN), TOPEX/ Poseidon (TP), Jason-1 (J1), Jason-2 (J2), and Geosat Follow-On (GFO) are used. The SSH measurements are along four sets of satellite ground tracks (**Figure 2.4**), and cover a time period of about 20 years from 1992 to 2012. All SSH measurements have been processed by applying standard corrections for atmospheric and geophysical effects as well as surface wave bias. The barotropic tide and the tide loading was corrected using the global ocean tide model Global Ocean Tide 4.7 (GOT4.7; Ray, 2013). Zhao et al. (2016) further developed a two-dimensional plane wave fit method to extract internal tides (Ray & Cartwright, 2001; Zhao & D'Asaro, 2011).

Plane wave fitting is a variant of traditional point-wise harmonic analysis, whereby all the available SSH measurements in a small window (160 x 160 km for mode 1, 120 x120 km for mode 2) are taken into consideration (**Figure 2.4**, gray boxes). At each along-track point, tidal constants can be derived by point-wise harmonic analysis, while internal tides at off-track points must be inferred from neighboring on-track measurements (**Figure 2.4** c, d). Internal tide parameters (amplitude and phase) are determined using a least square fit in each direction by fitting a plane wave to the satellite SSH time series. An internal wave appears as a lobe when the resultant amplitudes are fitted as a function of direction in polar coordinates. The amplitude and direction of a M_2 wave are then determined from this lobe. Afterwards, the gathered signal is removed from the original SSH data and the above procedure is repeated two more times from the resultant SSH data. A superposition of the three obtained M_2 internal tide waves gives the final internal tidal solution. The nontidal noise in the altimeter data prevents the extraction of more waves because their amplitude is lower than the 95% confidence level. The first three tidal waves account for about 95 % of the total SSH variance

(Zhao et al., 2016). The internal tide solutions are discarded in areas where the bottom slope is steeper than an empirical threshold of 6/1000 and where the noise on the continuum spectrum due to mesoscale eddies are overwhelming. A global map of the resulting mode 1 internal wave energy fluxes can be seen in **Figure 1.7**.

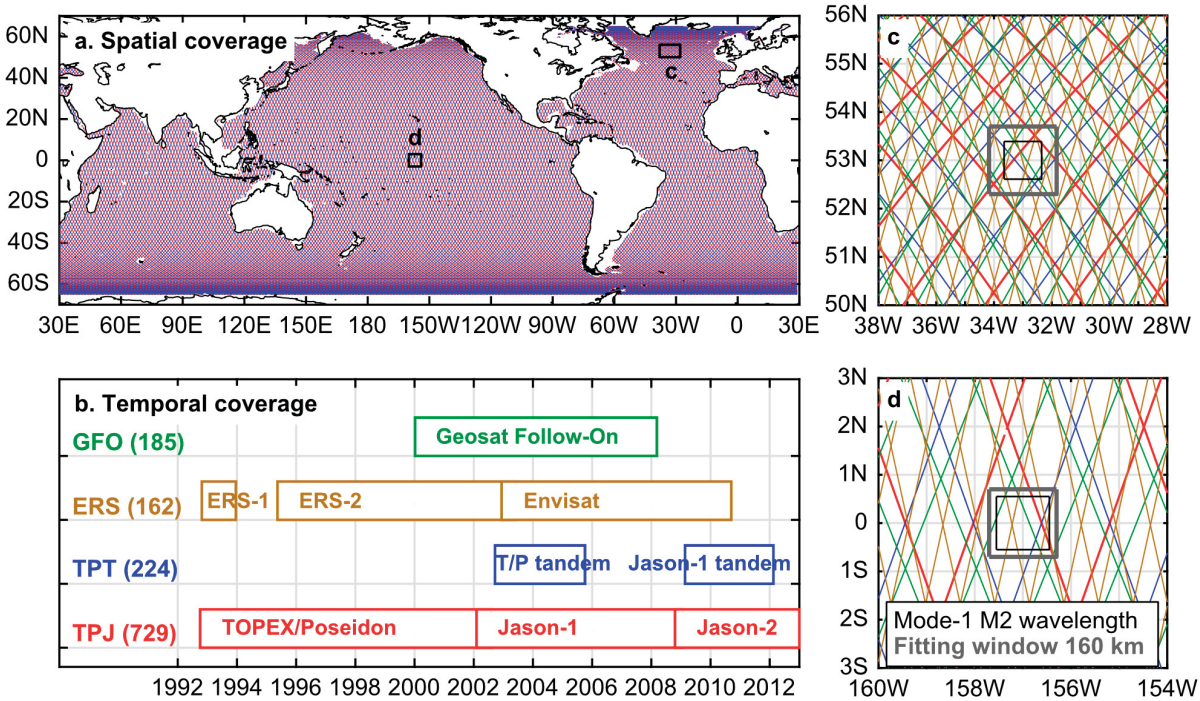

***Figure 2.4**: Spatial and temporal coverage of multi satellite altimeter data. The spatial coverage is shown in (a), (b) and (c), whereby (a) displays the global coverage and (c) and (d) display the sub regions at high and low latitudes respectively. Ground tracks of ERS (brown) and GFO (green) are not shown in (a). Black boxes indicate one wavelength of the local mode 1 M_2 internal tide and the gray boxes the 160 km fitting windows for mode 1. The temporal coverage is shown in (b), here the numbers of accumulated repeat cycles are given in parentheses. Figure taken from Zhao et al. (2016).*

3 Method

In the following section the methods used for data analyses and comparisons are explained in detail. First, I explain the method to calculate internal wave energy fluxes and energy density from moorings, which are also applied for the model data in section 3.1. These calculations of internal wave energy fluxes are adapted from Alford and Zhao (2007a) and Nash et al. (2005). Then I present the split of internal wave energy flux in a coherent and an uncoherent part, followed by the methods to calculate wind power, frequency spectra and the consistency check r_ω in sections 3.2 to 3.5.

3.1 Energy flux and energy density calculation

The energy flux calculations are the same for the STORMTIDE2 model and for the mooring measurements, whereby for the model each vertical layer is treated as if it would be a single point instrument in a mooring. The ADCP in the mooring recorded 19 bins with a length of 8 m each. For consistent non-biased data, the five bins closest to the ADCP were averaged to one data point (cf. section 2.1). The background stratification profile for the mooring measurements was calculated as the mean of 11 repeated CTD casts close to the mooring location that were measured directly before the mooring deployment during cruise POS516 (Walter et al., 2018). The background stratification profile for the STORMTIDE2 model is the mean stratification over all available model months. In the following sections 3.1.1 to 3.1.3 I discuss the necessary steps needed to be able to calculate the energy flux and energy density explained in section 3.1.4 and 3.1.5 respectively. A discussion of the methodical errors and an example time series for the calculation steps are presented in section 3.1.6.

3.1.1 Filtering

The velocity and temperature data from the in-situ measurements and the STORMTIDE2 model are filtered with a 4th-order butterworth filter with zero-phase response for the semidiurnal component M_2 and the near-inertial frequency f in the bandwidth ($c^{-1}\omega, c\omega$), with c = 1.25. The semidiurnal frequencies M_2 and S_2 are too close to be separated via bandpass

filtering, therefore the filtered variables are expected to show a spring-neap variability. The bandwidth parameter *c* was chosen narrow enough to maximally isolate the M_2 frequency, while being wide enough to avoid filter ringing (Alford & Zhao, 2007a).

To be able to use the velocity data of the Quartermaster (ADCP), its vertical component needed to be filtered for diurnal plankton migration because the migration of large zooplankton species is a common phenomenon in various regions of the ocean and can alter significantly the measured velocities. The filter used was adopted from Fischer and Visbeck (1993) and its effect can be seen in **Figure 3.1**. This filter calculates an average daily variation over 7 days (current day, 3 days backwards, 3 days forwards) and adapts itself to the data of the current day. One can see a clear bidaily response of the velocities when the plankton is moving up or down the water column in the red dots. The blue dots show the vertical velocity after applying the plankton filter once the bidaily migration is removed.

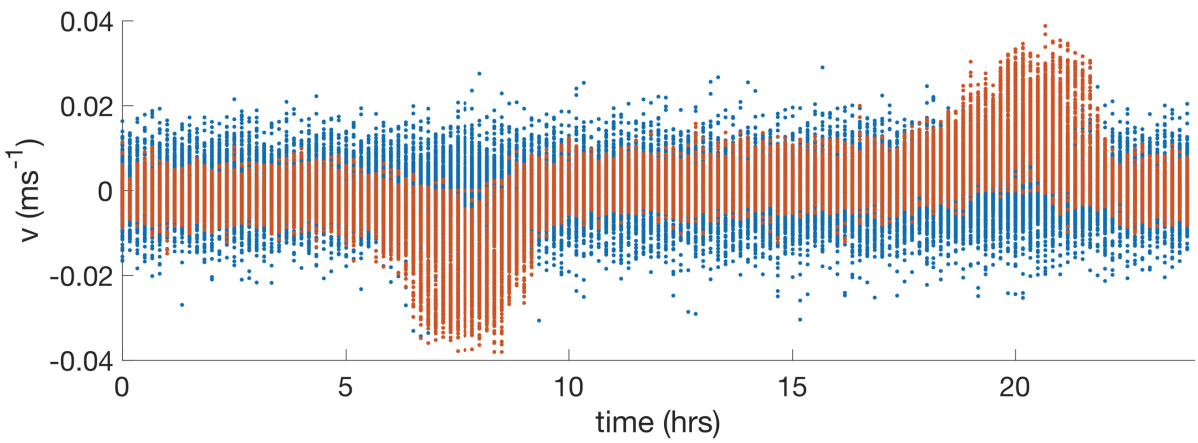

***Figure 3.1**: Effect of plankton filter on the vertical velocities of the ADCP. It removes the bidaily migration pattern of zooplankton; red: unfiltered data, blue: data after applied plankton filter.*

3.1.2 Vertical displacement

Internal waves induce a vertical displacement over the entire water column which is used in the following calculations. Generally, it is possible to calculate the vertical displacement either directly via the vertical velocities or via density variations. In this study, the density profile is strongly dominated by temperature, with salinity playing a minor role, therefore the density displacement can be thought to be equivalent to the displacement by the temperature itself. For the in-situ measurements the calculation of vertical displacements via temperature is usually more accurate due to a higher precision of the temperature sensors in compare to the direct measurements of the vertical velocity. For the model, it is known that the calculation

of the vertical displacement either via temperature or via the vertical velocities does not show any differences.

The vertical displacement is calculated at each depth layer of STORMTIDE2 for the M_2 and near-inertial frequency band as well as for the mooring time series at each instrument depth for the near-inertial band using the temperature gradient via the relation:

$$\eta(z_i, t) = T(z_i, t)/T_z(z_i) \qquad [3.1]$$

The vertical temperature gradient $T_z(z_i)$ for the model is computed as the mean of the entire model time series and for the mooring the mean of 11 repeated CTD casts before the mooring deployment. $T(z_i,t)$ is the bandpass filtered temperature measured at depth z_i and time t. The temperature gradient is assumed to be relatively constant over time and its minor variations are likely to have a negligible impact on the further calculation process (cf. temperature time series in section 2.1 and comparison of eddy induced variations on the stratification and the resulting mode shapes in section 4.2.2).

The stratification of the mooring time series in the lower part of the water column is too weak to calculate a vertical displacement for the M_2 frequency band from the in-situ temperature, as its gradient $T(z)$ falls below the threshold of 3×10^{-5} m^{-1} as given in Alford and Zhao (2007a). Thus, the displacements from the deepest two sensors for this calculation should be removed. To avoid this, the vertical displacement at all depths for the M_2 frequency band of the mooring time series is directly calculated from the M_2 filtered vertical velocities. Unfortunately, it is not possible to calculate the vertical displacement for the near-inertial frequency band of the mooring time series also via the vertical velocities. This is because the accuracy of the instruments, when filtered for the near-inertial frequency f, is not sufficient enough, since the magnitude of the vertical displacement of near-inertial waves is smaller as for an internal tide with the same energy. I therefore removed the lowest two sensors for the near-inertial energy flux calculation. Fortunately, the calculation of internal wave energy flux via mode separation is highly surface intensified, thus a reduction of the resolution in the lower part of the water column is less critical (Nash et al., 2005).

3.1.3 Modal decomposition

Over a flat seafloor the vertical structure of internal waves can be represented by a superposition of discrete vertical modes which depend only on the buoyancy frequency $N(z)$ and are defined as solutions of the eigenvalue problem

$$\frac{\partial^2}{\partial z^2}\eta(z) + \frac{N^2(z)}{c_n^2}\eta(z) = 0, \qquad [3.2]$$

with the boundary conditions $\eta(0) = \eta(H) = 0$, mode number *n*, water depth *H*, eigenspeed c_n, buoyancy frequency $N(z)$ and the vertical displacement $\eta(z)$ at depth *z*. The structure of mode 1 and mode 2 were calculated using iModes, a MATLAB toolbox for the modal solutions of the internal wave field (Haji, 2015; Saidi, 2011). This toolbox easily provides solutions to the Storm-Liouville eigenvalue problem with a Runge-Kutta scheme. The profiles of filtered horizontal velocities and vertical displacements were projected onto a linear combination of these modes with a least square fit, thus obtaining a full depth-profile. The boundary condition of a flat bottom is in the real ocean regularly violated. Nevertheless, at our mooring location the ocean floor is relatively flat, in other words the steepness of the ocean floor in comparison to the overall water depth is low. Hence, the criterion can be considered to be met. It is an ongoing discussion in the scientific community on when the ocean floor should be considered as too steep, but it seems that in the real ocean the method is not very sensitive to it.

3.1.4 Energy flux

The depth integrated horizontal energy flux for each mode can then be obtained from the covariance of the modal velocity $\vec{u}(z')$ and baroclinic pressure anomaly $p'(z')$ with

$$F = \int_{-H}^{0} \langle \vec{u}(z')p'(z') \rangle \, dz', \qquad [3.3]$$

where $\langle \quad \rangle$ is the average over one wave period. For each mode the baroclinic pressure anomaly $p'(z)$ is calculated via the vertical displacement and the buoyancy frequency $N(z)$ (Kunze et al., 2002), for each mode n ($n = 1,2$) as

$$p'_n(z) = \overline{\rho} \int_{-z}^{0} N^2(z')\,\eta_n(z')\, dz' - \overline{p_n}, \qquad [3.4]$$

with

$$\overline{p_n} = \overline{\rho} \int_{-H}^{0} N^2(z')\,\eta_n(z')\, dz'. \qquad [3.5]$$

where $\bar{\rho}$ is the vertically averaged density, $N(z)$ is the buoyancy frequency and $\eta(z)$ is the vertical displacement.

Following Zhao et al. (2010), the bandpassed semidiurnal internal tide is decomposed into a coherent and an incoherent component for each mode. M_2 and S_2 signals are harmonically fitted using the T_TIDE analysis software (Pawlowicz et al., 2002). The T_TIDE toolbox uses harmonic analysis to estimate tidal constituents (e.g. amplitude and phase) and their uncertainties of a time series which are then projected onto a sinus wave.

For each component (M_2 and S_2) the energy flux of the internal tide is calculated following the procedure described above and the total energy flux of the semidiurnal internal tide is defined as

$$F_{semi} = F_{M2} + F_{S2} + F_{in}, \qquad [3.6]$$

where F_{semi} is the energy flux for the bandpass filtered semidiurnal component, F_{M2} and F_{S2} are the harmonically fitted coherent parts of the energy flux for M_2 and S_2 respectively, and F_{in} the incoherent part of the energy flux. Important to note is that the variance in the incoherent tides increases with record length (Ansong et al., 2015; Nash, Kelly, et al., 2012), which leads to an underestimate of the multi-decadal incoherent tide if it is calculated over only a few months.

3.1.5 Energy density

The depth integrated energy density *E*, is calculated for each mode and each frequency band as the sum of the horizontal kinetic energy density (*KE*) and available potential energy density (PE) via:

$$KE = \frac{1}{2}\bar{\rho}\int_{-H}^{0} |\vec{u}^2(z)|\, dz, \qquad [3.7]$$

and

$$PE = \frac{1}{2}\bar{\rho}\int_{-H}^{0} N^2(z)\eta^2(z)\, dz, \qquad [3.8]$$

where $\bar{\rho}$ is the vertically averaged density, $N(z)$ is the buoyancy frequency and $\vec{u}(z)$ and $\eta(z)$ are the full depth profiles of velocity and displacement.

3.1.6 Errors and example time series

The error of calculating modal internal wave energy flux and energy density lies mainly on the depth distribution of the instruments in the water column, but also their sampling interval, their accuracy, as well as the resolution of the stratification profile can influence the result. As stated before the sampling interval and the accuracy of the instruments as well as the stratification profile is highly sufficient to resolve low mode internal waves and should therefore have minor importance. Hence, the error is mainly based on the number and the vertical distribution of instruments and following the estimates given in Nash et al. (2005), I consider the systematic error to be <5 % for the energy fluxes from the mooring data and <1 % for the STORMTIDE2 data. For the measured and modeled time series, given confidence intervals of the mean values are calculated as 95% bootstrapped confidence intervals with 10^4 repetitions. Due to the shape of the modal structure big gaps close to the surface have a higher impact onto the results whereby data gaps closer to the seafloor are less important.

A close up of the sum of mode 1 and mode 2 meridional velocity, vertical displacement and pressure anomaly, as well as the resulting vertically depth integrated energy fluxes and potential and kinetic energies are shown in **Figure 3.2** for the mooring time series in the semidiurnal and near-inertial frequency band. The modal solutions of horizontal velocities and vertical displacement are in general representative for the discrete filtered data. The velocity data, of which the barotropic component was removed, are surface intensified owing to the weaker stratification at the bottom. Large shallow values of the vertical displacement cannot be represented by a sum of mode 1 and mode 2, and are therefore absent. The baroclinic pressure anomaly reveals values of about 350 Pa for the semidiurnal band and about 40 Pa for the near-inertial band, which results in surface elevations of about 3.5 cm and 4 mm respectively, which agrees with data from satellite altimetry. The resultant energy flux is the covariance of velocity and pressure anomaly and is therefore strongly surface intensified (Alford & Zhao, 2007a).

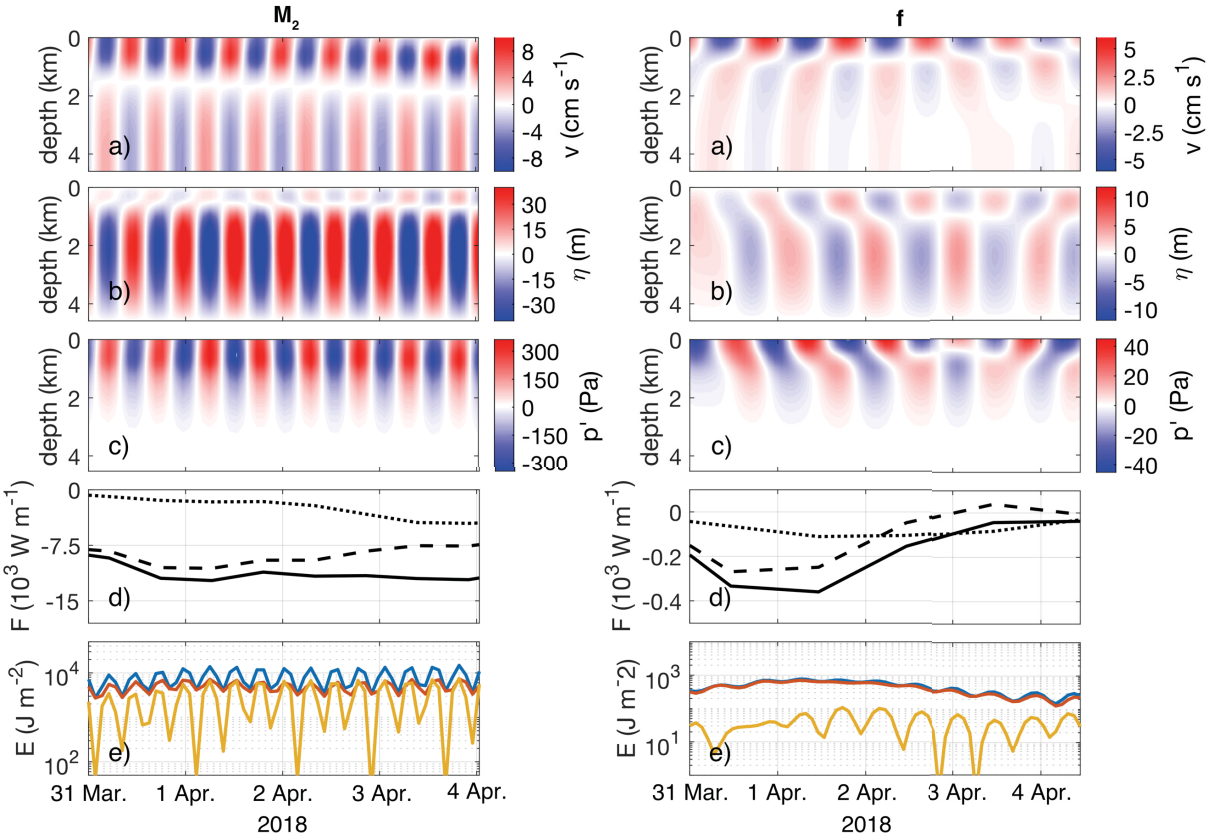

***Figure 3.2**: Details of the energy flux calculations from mooring time series; a) sum of the mode 1 and mode 2 meridional velocity for the first peak in the spring neap cycle during April; b) sum of mode 1 and mode 2 vertical displacements; c) sum of mode 1 and mode 2 pressure anomaly; d) depth integrated meridional energy flux mode 1 (dashed line) mode 2 (dotted line) and their sum (solid line); e) Energy density (blue) as sum of kinetic energy (red) and potential energy (yellow).*

3.2 Wind power

The mechanical energy input to the ocean by atmospheric winds is a major source for driving the large-scale ocean circulation (e.g. Ferrari & Wunsch, 2009). Power input to the ocean can be regarded as a transfer of atmospheric kinetic energy into the ocean, reflected in the wind stress bulk formula,

$$\tau = \rho_a c_d |U_{10} - u_o|(U_{10} - u_o), \qquad [3.9]$$

where τ is the surface wind stress, ρ_a is the density of air at sea level; c_d is the drag coefficient, u_o is the ocean surface velocity and U_{10} is the wind speed at 10 m above the surface. One consequence of the quadratic dependence of the wind stress on the wind itself is that the high

frequency wind does not simply average out but contributes to the time averaged wind stress (e.g. Thompson et al., 1983).

To estimate the impact of the wind into the mixed layer and the resulting near-inertial oscillations the near-inertial wind power W_I is computed as follows:

$$W_I = \vec{\tau}\vec{u} \qquad [3.10]$$

Where $\tau = (\tau_x, \tau_y)$ is the surface wind stress at the ocean surface 10 m above the sea surface and $u = (u, v)$ are the sea surface velocities. **Figure 3.3** illustrates the mechanical damping effect by the wind. When the wind is aligned with the current, the stress is smaller and hence the wind does less positive work. When the wind opposes the current, the stress is larger and hence does more negative work. Therefore, positive fluxes (energy transferred from the atmosphere to the ocean) results when the wind is aligned with the current, tending to further accelerate. Of the wind energy input into near-inertial motions, it is estimated that about 75-90 % dissipate in the upper ocean, while the rest can radiate into the ocean interior in the form of internal gravity waves (Crawford & Large, 1996; Rimac et al., 2016). But also, parameters such as the mixed layer depth, or the dominant wavenumber of the wind stress spectrum influence the amount of near-inertial energy which is dissipating within the mixed layer.

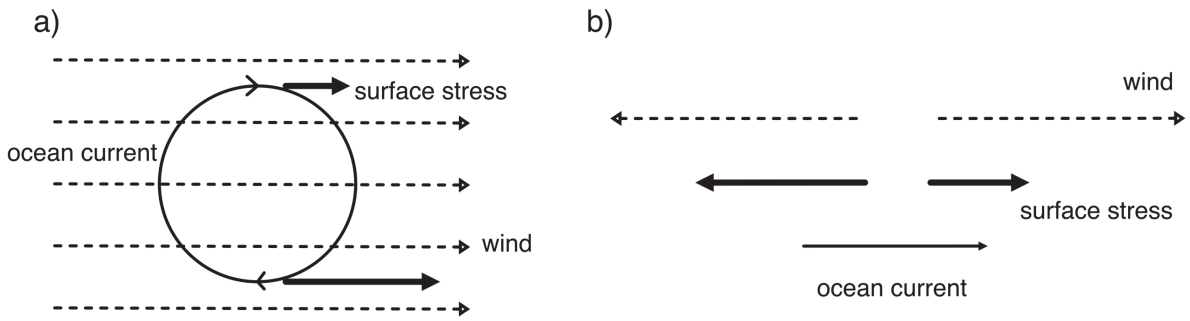

***Figure 3.3**: Illustration of the mechanical damping by the wind. The surface stress depends on the relative motion between the air and the surface ocean. a) The wind blows over an eddy. The stress on the upper side is smaller because wind and current are aligned to each other. The stress on the lower site is higher because wind and current oppose each other. b) as in a), but for a steady current. Figure adopted from (Zhai et al., 2012).*

3.3 Frequency spectra

To further investigate the influence of mesoscale eddies and storm events on the background flow field, spectra of unfiltered vertical (*w*) and horizontal (*u*, *v*) baroclinic velocities of the

measured time series were calculated by projecting them onto the corresponding mode structure with a least square fit. From the resulting full depth modal velocities, the Power Spectra Density (PSD) was estimated for each mode using half-overlapping one-week segments with the build in MATLAB function pwelch.

The Welch method computes a periodogram for each segment and then averages these estimates to produce and estimate of the total power density. These periodograms represent uncorrelated estimates of the power spectrum density because the process is wide-sense stationary and the method uses estimates of different segments of the entire time series. Thereby, further averaging reduces the variability. The segments are multiplied by a Hamming window. Data at the beginning and at the end of the segment are tapered by the window function and occur away from the ends of adjacent segments because of the overlap of each individual segment. This protects against the loss of information caused by the window function.

3.4 Consistency check r_ω

The ratio of kinetic (KE) and potential energy (PE) can be used as a consistency check for a freely propagating internal tide with that intrinsic frequencies can be detected. The ratio is defined as:

$$r_\omega = \frac{\langle KE \rangle}{\langle PE \rangle} = \frac{\omega^2 + f^2}{\omega^2 - f^2} \qquad [3.11]$$

where $\langle \quad \rangle$ is the average over one wave period with the wave frequency ω (here M_2) and f is the local inertial frequency. The right side of the equation gives the theoretical ratio between kinetic and potential energy for the hydrostatic case. By bandpass filtering the initial velocity data for calculating the energy components, some variations around the theoretical value can be expected beforehand.

4 The temporal variability of the M_2 internal tide in a tide beam and its interaction with eddies

There is an existing lack of long-term observations of internal tides in a tide beam. The 20 consecutive months of mooring observations in the tide beam south of the Azores, gives the opportunity to investigate this temporal variability. The goal is to study how the temporal variability of internal gravity waves in a tide beam generally looks like and what its influencing factors are. Furthermore, how its characteristics, like the coherence of the energy flux or the ratio between different modes, are changing over time especially in the context of eddy events. In this chapter, I look at the time series of the magnitude and the direction of the energy flux, the time series of the kinetic and the potential energy, changes in the coherent part of the energy flux and its modal composition. Additionally, the time series is checked for the intrusion of other frequencies, and frequency spectra during eddy event periods are performed. In section 4.1 I present the results of the in-situ measurements, that are discussed in section 4.2.

4.1 Results

The following result section is split into section 4.1.1 presenting the general observations of the temporal variability of internal tide energy flux during the mooring deployment and section 4.1.2 which presents the observations regarding interaction of internal tides with the occurrence of mesoscale eddy events during the in-situ measurements. A comprehensive list of all internal tide energy fluxes, kinetic and potential energy which are discussed in the following section is given in **Table 4.1**

.

	Semidiurnal flux (kW m^{-1})			M2+S2 Coherent flux (kW m^{-1})			M2 coherent flux (kW m^{-1})			Kinetic energy (kJ m^{-2})			Potential Energy (kJ m^{-2})			r_ω
	Mode 1	Mode 2	**total**	Mode 1	Mode 2	**total**	Mode 1	Mode 2	**total**	Mode 1	Mode 2	**total**	Mode 1	Mode 2	**total**	
Mooring total	8.10 ±0.28 [0.04]	0.80 ±0.04 [0.05]	**8.91 ±0.29 [0.03]**	7.60 ±0.03	0.42 ±0.01	**8.02 ±0.03**	6.96 ±0.02	0.28 ±0.01	**7.24 ±0.02**	2.34 ±0.08	0.56 ±0.03	**2.90 ±0.08**	1.55 ±0.07	0.43 ±0.02	**1.98 ±0.07**	**2.25 ±0.15**
Mooring no eddy	8.62 ±0.41 [0.05]	1.09 ±0.09 [0.08]	**9.71 ±0.45 [0.05]**	8.03 ±0.11	0.82 ±0.04	**8.85 ±0.14**	7.44 ±0.10	0.75 ±0.04	**8.19 ±0.13**	2.00 ±0.09	0.73 ±0.06	**2.73 ±0.12**	1.88 ±0.12	0.55 ±0.05	**2.43 ±0.13**	**1.38 ±0.07**
Mooring surface eddy 1	6.57 ±0.70 [0.11]	0.60 ±0.08 [0.13]	**7.16 ±0.73 [0.10]**	5.83 ±0.03	0.28 ±0.003	**6.11 ±0.03**	5.17 ±0.01	0.21 ±0.001	**5.39 ±0.01**	2.66 ±0.31	0.43 ±0.05	**3.09 ±0.31**	0.98 ±0.11	0.34 ±0.06	**1.32 ±0.12**	**3.17 ±0.48**
Mooring surface eddy 2	6.56 ±0.71 [0.11]	0.58 ±0.05 [0.09]	**7.14 ±0.73 [0.10]**	5.45 ±0.01	0.15 ±0.002	**5.60 ±0.01**	5.25 ±0.01	0.10 ±0.001	**5.35 ±0.01**	2.36 ±0.16	0.42 ±0.04	**2.78 ±0.19**	1.11 ±0.17	0.34 ±0.04	**1.45 ±0.17**	**3.83 ±0.65**
Mooring subsurface eddy 1	8.80 ±0.99 [0.11]	0.75 ±0.12 [0.16]	**9.55 ±1.01 [0.11]**	8.21 ±0.03	0.39 ±0.004	**8.60 ±0.03**	7.36 ±0.02	0.35 ±0.001	**7.71 ±0.02**	2.70 ±0.28	0.47 ±0.07	**3.18 ±0.31**	1.46 ±0.19	0.42 ±0.07	**1.89 ±0.21**	**2.06 ±0.26**
Mooring subsurface eddy 2	9.46 ±0.73 [0.08]	0.76 ±0.11 [0.14]	**10.22 ±0.77 [0.08]**	8.75 ±0.02	0.10 ±0.002	**8.85 ±0.02**	8.17 ±0.02	0.07 ±0.001	**8.24 ±0.02**	2.55 ±0.17	0.59 ±0.07	**3.14 ±0.21**	1.87 ±0.17	0.38 ±0.07	**2.25 ±0.21**	**2.01 ±0.29**

Table 4.1*: Mean energy flux of the mooring in the semidiurnal band the M_2+S_2 coherent and M_2 coherent part, kinetic and potential energy and the ratio r_ω for the entire deployment period and eddy events. Distortion parameter d in square brackets for the semidiurnal energy flux.*

4.1.1 Time series of the M_2 internal tide

The semidiurnal energy fluxes calculated from equation [3.3], as the covariance of the modal velocity and baroclinic pressure anomaly, show a strong spring-neap variability, especially in the first mode but to a lesser degree also in the second mode. The amplitude of the total energy flux is clearly dominated by mode 1 which is often indistinguishable from the total energy flux. **Figure 4.1** shows the development of the energy flux in the first two modes during the mooring deployment as well as the barotropic tide from TPXO9 at the mooring location. One can see that the peaks of the energy flux follow in general the forcing of the barotropic tide with few exceptions.

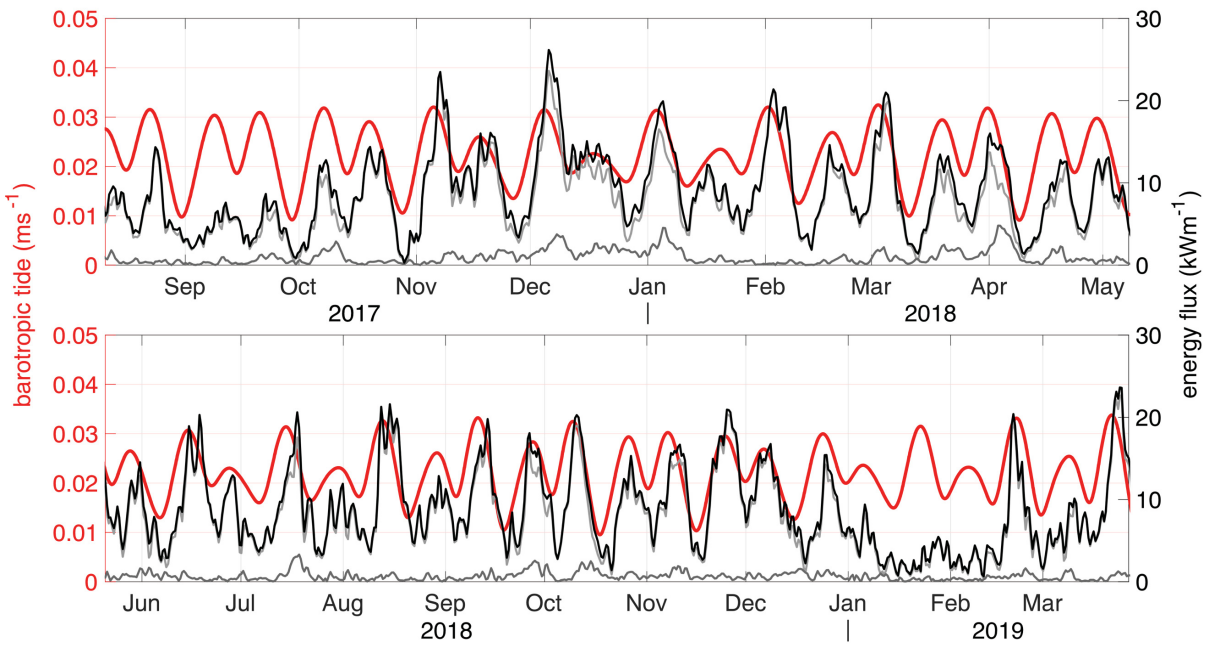

***Figure 4.1**: Time series of internal tide energy flux in relation to the barotropic tide from TPXO9. The energy flux is dominated by mode 1 and shows a clear spring-neap variability. Black: Sum of mode 1 and mode 2 of semidiurnal energy flux from the mooring observations. Light grey and dark grey are the first and second mode of the semidiurnal energy fluxes respectively; red: amplitude of the barotropic tide as the sum of the first 4 (M_2, S_2, N_2, K_2) semidiurnal tidal constituents from TPXO9 at the mooring location.*

The total mean of the amplitude of the semidiurnal energy flux (sum of mode 1 and mode 2) in the mooring observation is 8.91±0.29 kW m^{-1} (8.10±0.28 kW m^{-1} for mode 1, 0.80±0.04 kW m^{-1} for mode 2) with peaks up to 26.17 kW m^{-1}. The coherent fraction of the energy flux of the sum of modes 1 and 2 during the whole deployment period is 81 %, while the rest is

incoherent. In mode 1 94 % of the energy flux is coherent, whereby in mode 2 only 53 % of the energy flux is coherent.

The peaks in the measured energy flux lag those of the barotropic tide from TPXO9 (**Figure 4.1**). This time lag can be used for a rough estimation of the possible generation site using the group speed of mode 1 and mode 2 waves to infer the covered distance (e.g. Holloway & Merrifield, 2003). This was done for five representative peaks for mode 1 and three representative peaks for mode 2. The distance for mode 1 ranges from 124 km up to 451 km with a mean of 266 km. The distance for mode 2 ranges from 128 km up to 235 km with a mean of 185 km. These distances in combination with the mean direction of the energy flux point towards the seamount chain south of the Azores as generation site for the observed internal tides, confirming the earlier study by Köhler et al. (2019).

The steadiness of the energy flux at the mooring location is demonstrated by its direction and the ratio between the first and second mode in the time series in **Figure 4.2**. In general, the direction of the energy flux does not vary much in time, with few exceptions, and is steadily pointing in southwest direction, away from its generation site. These exceptions occur between August and November 2017, January and March 2018, Mai and September 2018 and January and March 2019. They are more prominent in mode 2, with sometimes pointing even in northward direction. The mean direction of the total semidiurnal mode 1 energy flux is 226°±2°, whereas the mean direction of mode 2 energy flux is at 193°±3°. Time periods with a higher variability, or generally more mode 2 seem to coincide with the exceptions in the time series of the direction. The fraction of the first mode in relation to the total energy flux is 89.6±0.5 %, and range between 44.6 % and 99.9 %. In the coherent part of the energy flux the fraction of the first mode changes to 94.8±0.1 %.

Figure 4.3 displays the time series of potential and kinetic energy for the first and second mode. The time series shows the means over one wave period and would otherwise display semidiurnal fluctuations. In the M_2 frequency band the kinetic energy (KE, green line) generally exceeds the potential energy (PE, purple line) while both energy flux (F) and energy density (E) are highly variable and rise and fall together over time. The total mean of the amplitude of KE as the sum of mode 1 and mode 2 is 2.90±0.08 kJ m^{-2} (2.34±0.08 kJ m^{-2} for mode 1 and 0.56±0.03 kJ m^{-2} for mode 2). The total mean of the amplitude of PE as the sum of mode 1 and mode 2 is 1.98±0.07 kJ m^{-2} (1.55±0.07 kJ m^{-2} for mode 1, 0.43±0.02 kJ m^{-2} for mode 2).

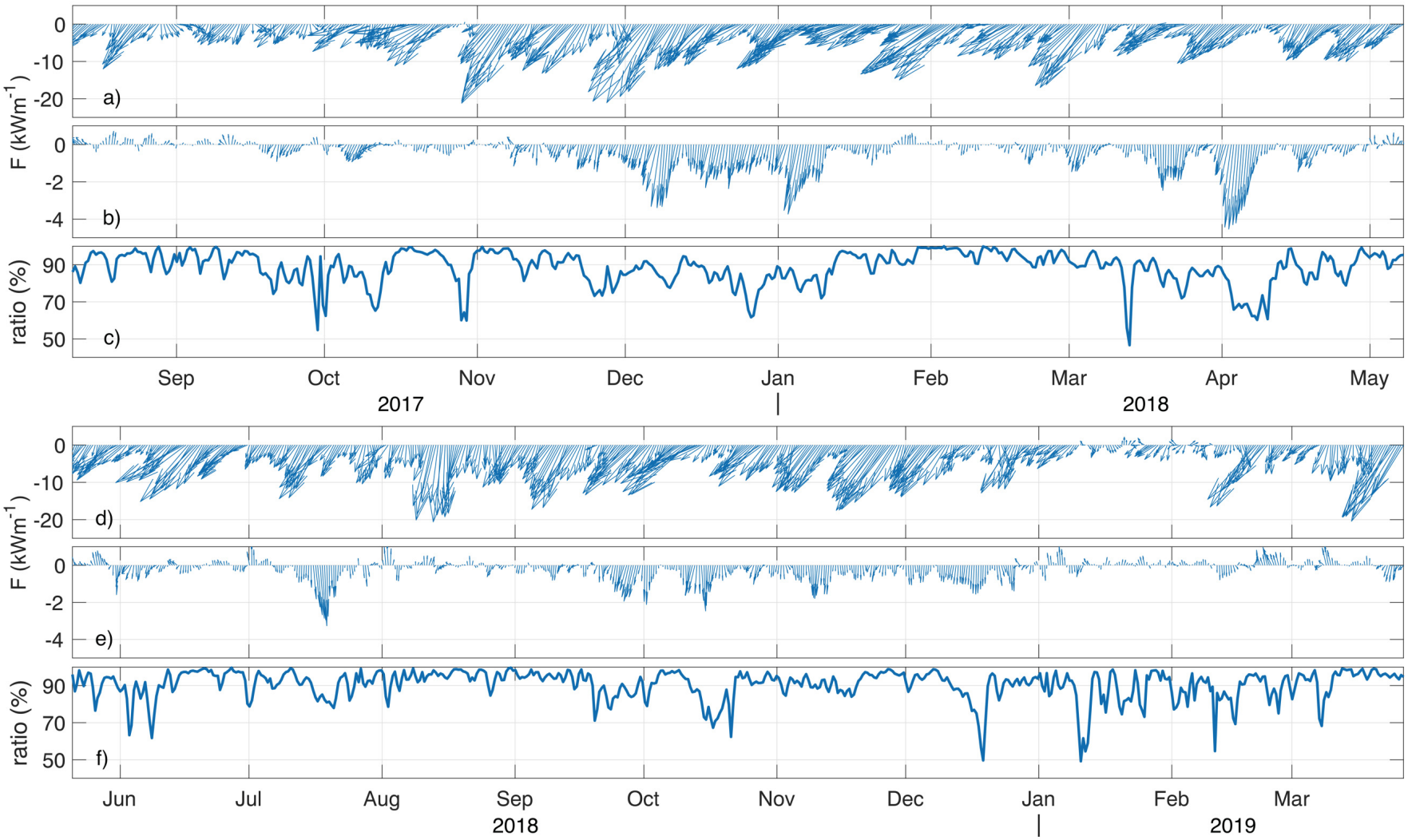

***Figure 4.2**: Directional variability and magnitude of the semidiurnal energy flux for mode 1 (a, d) and mode 2 (b, e) from the mooring time series; note the different scaling of the y-axis for mode 1 and mode 2; ratio between first and second mode of energy fluxes(c, f); 80 % means that the combined mode 1 and mode 2 flux consists of 80 % mode 1 and 20 % mode 2 at the corresponding time.*

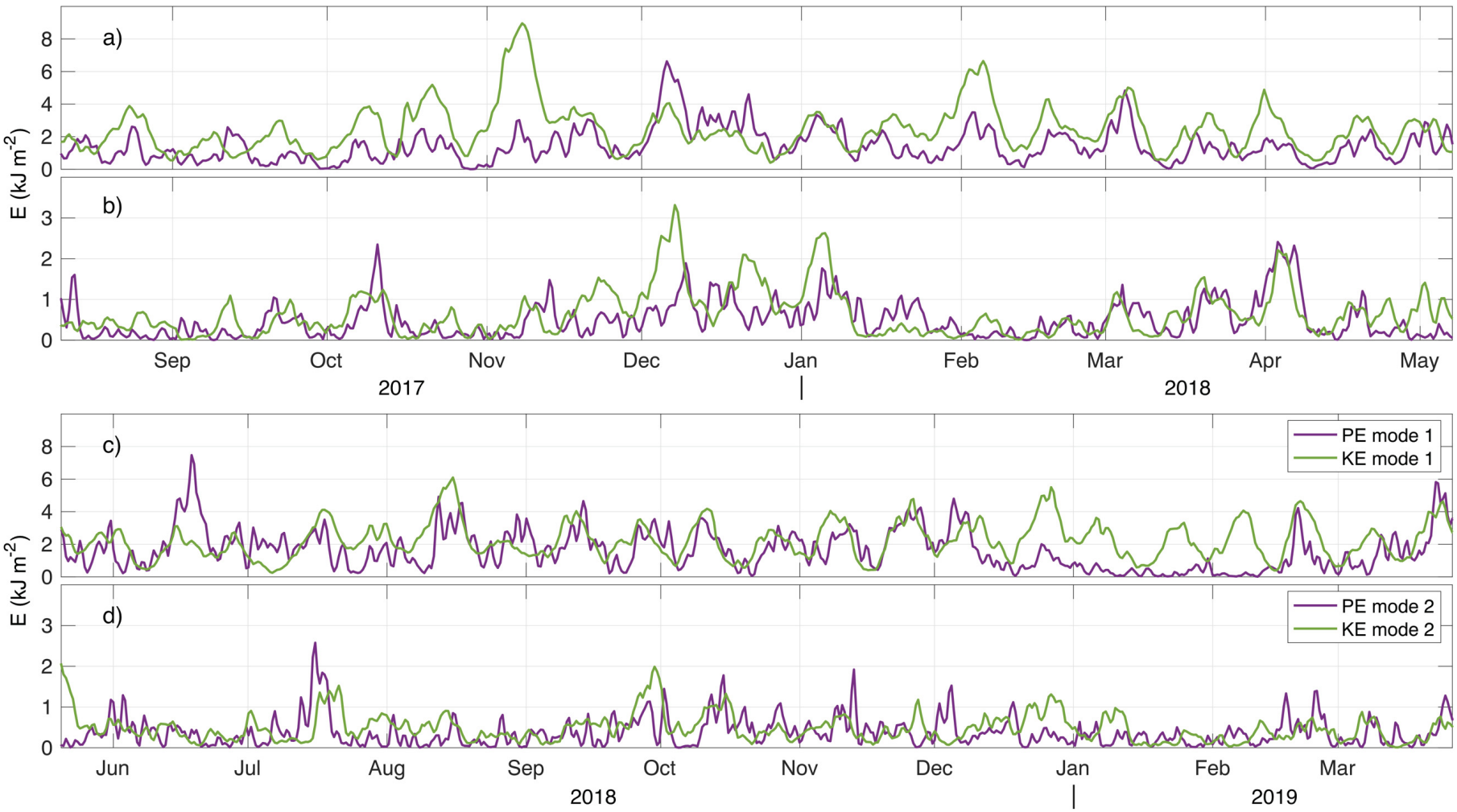

***Figure 4.3**: Time series of potential (PE, purple) and kinetic energy (KE, green) of the in-situ measurements for the first and second mode in the semidiurnal frequency band as means over one wave period. Note the different scaling of the y-axis for mode 1 and mode 2.*

To investigate possible intrusions of intrinsic frequencies the ratio r_ω between kinetic and potential energy was calculated with equation [3.11] and can be seen in **Figure 4.4** in perspective to the theoretical value. The mean ratio r_ω is 2.25±0.15 while the theoretical value is 1.82. as shown with the red line. As expected due to the initial bandpass filtering one can see variations around the theoretical value, but four periods are more elevated: one between September and November 2017, one between February 2018 and March 2018, one between July 2018 and August 2018 and finally one between January 2019 and February 2019.

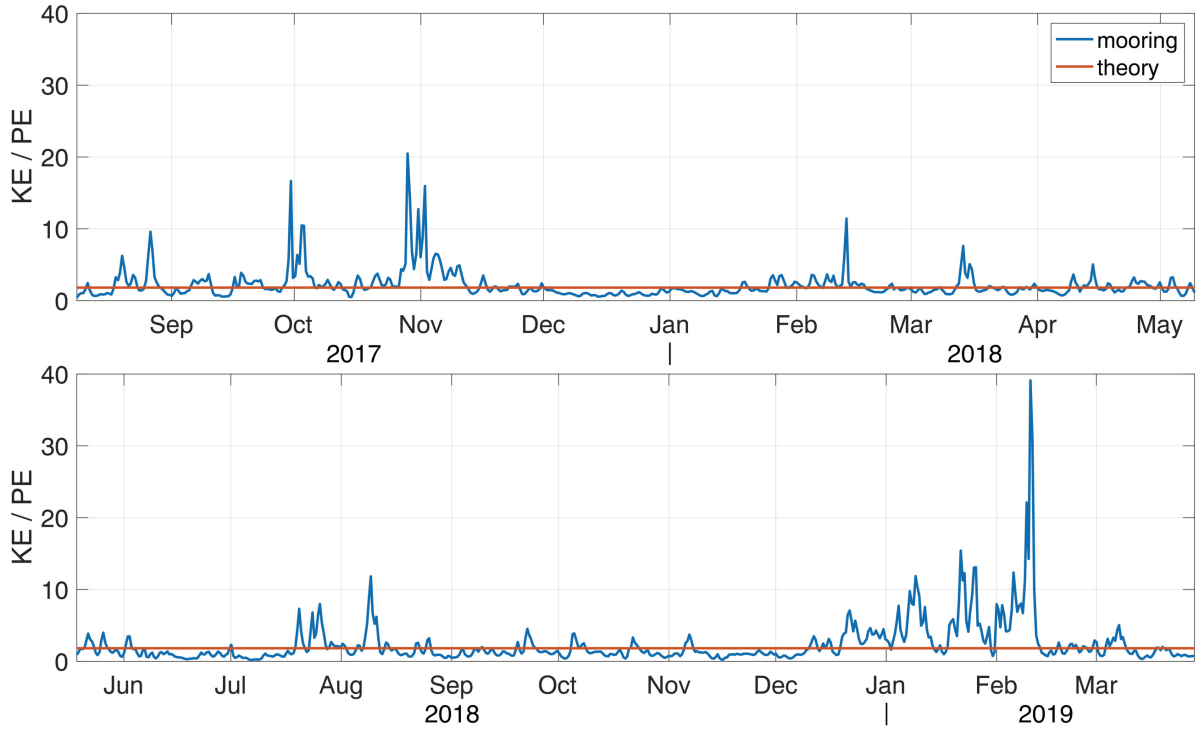

***Figure 4.4**: Ratio r_ω of kinetic energy (KE) to potential energy (PE) from the mooring time series (blue) and the theoretical value (red). One can identify four elevated periods of r_ω between September to November 2017, February to March 2018, July to August 2018 and January to February 2019, indicating the intrusion of intrinsic frequencies in the M_2 frequency band.*

The background internal wave field can be distorted by interactions with mesoscale flow, e.g. by inducing changes in propagation directions and by the exchange of energy. To quantify these distortions, I calculated a distortion metric (*d*) following Dunphy et al. (2017), who analyzed the propagation of internal tides through a turbulent eddy field in numerical experiments and analyze the consistency ratio r_ω for intrinsic frequencies. *d* is defined as the standard deviation of the energy flux normalized by the mean of the energy flux (**Table 4.1**, square brackets). For the semidiurnal component this yields 0.03 for mode 1+2 (0.04 mode 1 and 0.05 mode 2 separately) during the total observation period. The fluctuations in the energy flux, its modal composition, its direction and the changes of the distortion parameter *d* and the consistency ratio r_ω by interactions of eddies is further examined in section 4.2.1.

4.1.2 Eddy event observations within the M_2 internal tide time series

At the beginning of the time series, between August and November 2017, and in the end of the time series, between December and March 2019 the observed energy flux of the internal tide is notably lower compared to the remaining months (**Figure 4.1**). My hypothesis is that the observed decrease of the energy flux is caused by interactions with mesoscale features in the ocean. To verify this hypothesis, I calculated eddy kinetic energy (EKE) from the current meter time series, as well as from the geostrophic velocities taken from a Copernicus Marine Environment Monitoring Service (CMEMS) satellite altimetry dataset called SEALEVEL_GLO_PHY_L4_REP_OBSERVATIONS_008_047 (**Figure 4.5**). The dataset contains multimission altimeter satellite gridded sea surface heights and derived variables computed with respect to a twenty-year mean. All satellite missions are homogenized with respect to the reference mission OSTM/Jason-2. The data processing removes any residual orbit error, long wavelength error and large biases and discrepancies between various data flows. After a cross validation, the Sea Level Anomaly (SLA) is sub-sampled. Geostrophic currents are then derived from the SLA data.

To infer a potential influence of changes by the background flow field on the internal wave energy flux, the EKE from 40h low-pass filtered horizontal velocities (*u,v*) of all current meter time series at all instrument depths, and from the CMEMS dataset are calculated using the following relation:

$$EKE = \frac{u^2 + v^2}{2} \tag{4.1}$$

The EKE measured by the current meters shows in the first deployment period higher values between the end of September and mid of October 2017 in the upper ocean and between February and April 2018 at about 2000 m (green line in **Figure 4.5** a). During the second deployment period the EKE calculated from the current meter records show generally higher values in the upper ocean than during the first deployment period with a similar elevation as in the first deployment period at about 2000 m between mid of July 2018 until October 2018 and a stronger EKE elevation between mid of November 2018 until March 2019. With the EKE calculation in total four different Eddy periods are defined, which agree with the periods of a

higher directional variability in mode 2 (**Figure 4.2**), and the elevated periods in the r_ω time series (**Figure 4.4**).

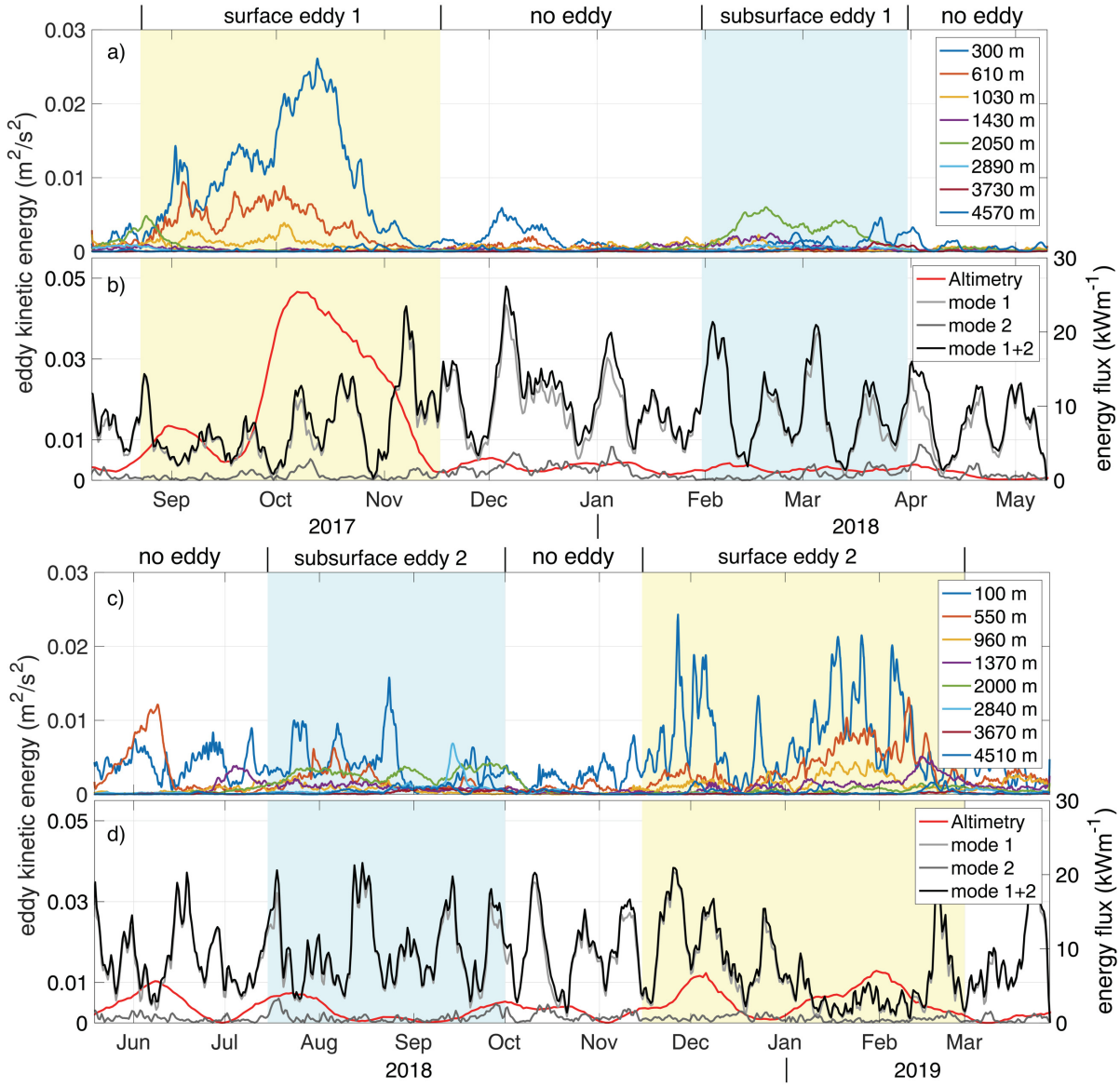

***Figure 4.5**: Definition of surface and subsurface intensified eddy phases during the mooring deployment. a) and c) Eddy kinetic energy (EKE) at the mooring location from the moored current meters. b) and d) EKE from satellite altimetry (red line) and observed energy flux of the semidiurnal internal tide (black and grey lines). Different background colours indicate eddy activity: yellow = surface eddy; blue = subsurface eddy; white = no eddy. Note the different scaling of the y-axis of the EKE between a) and b), as well as c) and d).*

The EKE from the CMEMS dataset aligns with the EKE from the mooring close to the surface, confirming the presence of two surface intensified mesoscale eddies in the beginning and at the end of the time series (**Figure 4.5**, yellow background). In the second half of the mooring deployment the EKE from the moored current meters as well as the CMEMS dataset show a

higher variability than in the first phase of the mooring deployment (**Figure 4.5**, panel c, d). But the strength of the second surface intensified eddy at the end of the time series is higher in the measurements from the current meters than in the CMEMS dataset albeit still visible. While the elevation of EKE under the water surface cannot be detected by data from satellite, the presence of two surface intensified eddies as well as two subsurface intensified eddies can also directly be seen in the 40-hours lowpass filtered meridional velocity data in **Figure 4.6**, as indicated in **Figure 3.2** as enhancements of the horizontal velocity components. With these information, I split the measured energy flux time series of the mooring in different time periods defined with the presence/absence of surface/subsurface eddies to further investigate the influence of these eddies on the variability of the energy flux time series: two surface eddy periods (surface eddy 1 and surface eddy 2), two subsurface eddy periods (subsurface eddy 1 and subsurface eddy 2) and one no-eddy period, defined as in between the eddy periods.

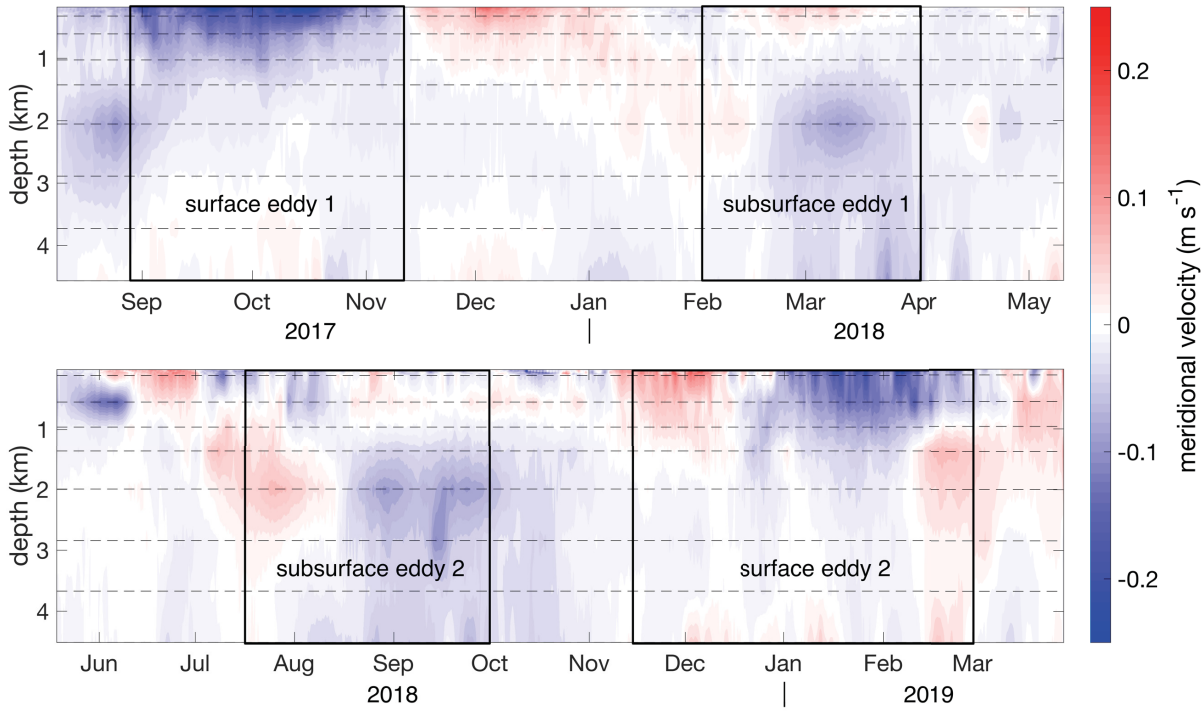

***Figure 4.6**: 40-hours low pass filtered meridional velocities (v) of the in-situ measurements. Black Boxes indicate phases of elevated EKE – defining the different eddy phases.*

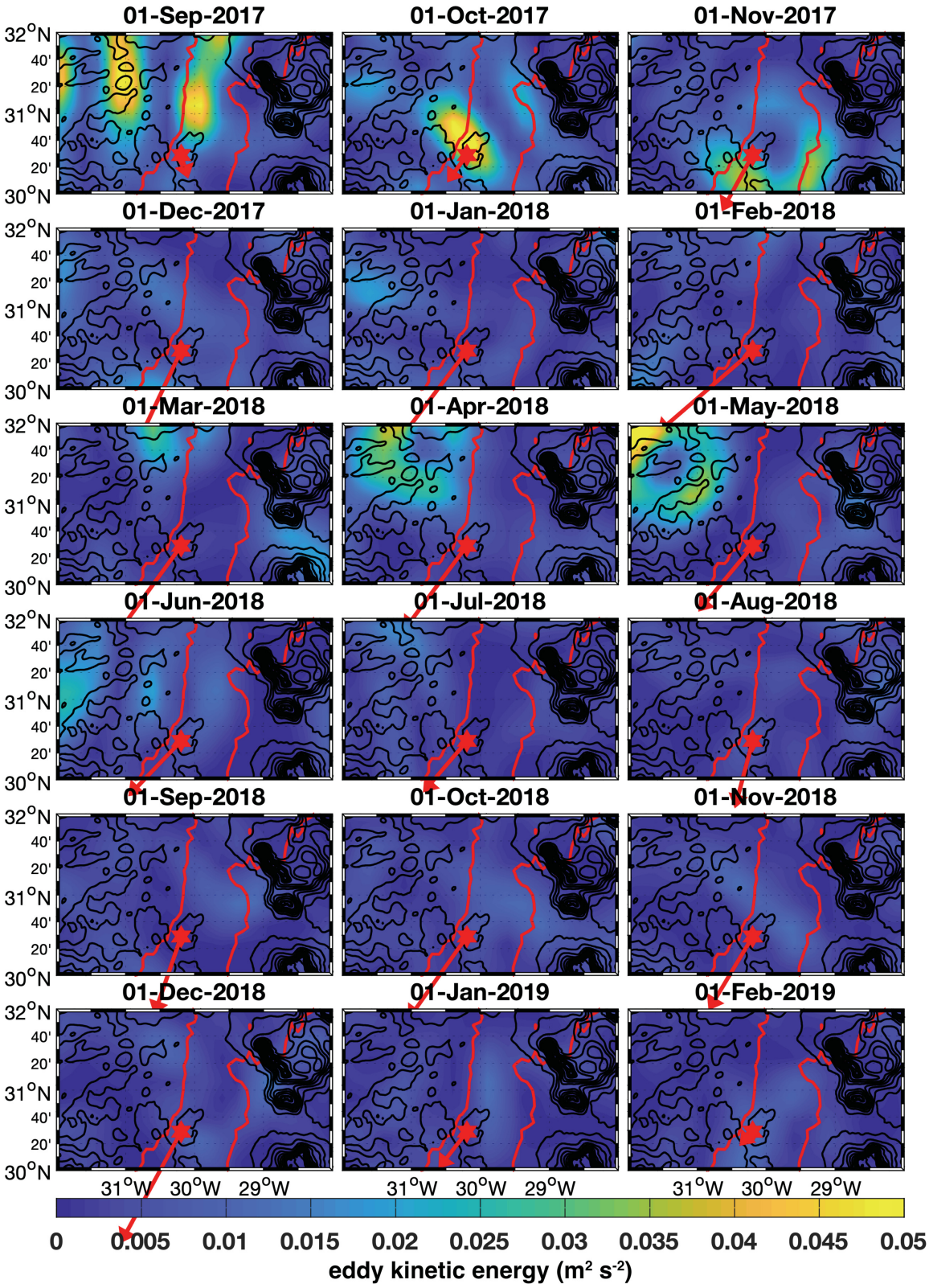

***Figure 4.7**: Eddy kinetic energy (EKE) at selected times during the mooring deployment calculated from satellite altimetry. Red star and arrow: Mooring location and the total semidiurnal energy flux as the mean of the given day ±10 M2 periods (approx. 5 days). Red contour line: 1.8 kW m-1 contour line of mode 1 and mode 2 energy flux from satellite altimetry (as shown in Figure 2.1 a) as an indicator for the tide beam. Black contour lines of bathymetry for every 100 m in the upper 1000 m and every 500 m for the rest of the water depth.*

During the remaining time of the in-situ measurements, except the four eddy periods, there was always some elevation of EKE from CMEMS at the mooring location. But another distinct surface intensified eddy could not be detected at the mooring location, or inside the tide beam between mooring location and the generation site of the internal tides. This is important because interactions between internal tides and mesoscale motions would happen also at these 'upstream' locations which would lead to biased measurements at the mooring. Thus, this elevation of the surface EKE is considered as natural variability of the ocean state. Further subsurface eddies cannot be excluded as they are not detectable by satellites. The EKE from CMEMS in the region between the generation site of internal tides and the mooring location is show in **Figure 4.7**. Here the surface intensified eddy in the beginning of the time series can clearly be seen as a *"ring"* with further EKE elevations in the remaining time period.

During the periods when the eddies were present at the mooring location, the characteristics of the internal tide energy flux changed considerably, indicating an interaction between the mesoscale structures and the internal tide. The semidiurnal energy fluxes in the first and second mode during surface eddy 1 are about 26 % lower (-24 % for mode 1, -45 % for mode 2) than during the time period when no eddy is present (**Table 4.1**), and similar to this the energy fluxes during surface eddy 2 are also about 26 % lower (-24 % for mode 1, -47 % for mode 2). The subsurface eddies seem to affect mainly the second mode, leaving the first mode almost intact. Here the calculated energy fluxes in the first and second mode for the semidiurnal band during subsurface eddy 1 are about 2 % lower (+2 % for mode 1, -31 % for mode 2) than during the time period when no eddy is present. While during subsurface eddy 2 the energy flux is in total even 5 % higher (+10 % for mode 1, -30 % for mode 2), with the second mode intermittently reaching almost zero during both subsurface eddy periods.

The direction of the semidiurnal energy flux has a higher variability during the eddy periods than during the no eddy period. This can be observed in **Figure 4.2** (a, b, d, e) in the presented mean values which are calculated over the above defined eddy periods. The direction of the mean amplitude during the no eddy period for mode 1 is 230°±2° and 207°±5° for mode 2. The direction changes during surface eddy 1 to 217°±7° for mode 1 and 187°±7° for mode 2, and during surface eddy 2 to 218°±7° for mode 1 and 178°±8° for mode 2. During the subsurface eddies this effect is even more pronounced on the second mode with 225°±3° for mode 1, 199°±11° for mode 2, and 235°±7° for mode 1, 185°±9° for mode 2 during subsurface eddy 1 and subsurface eddy 2 respectively.

With the varying decrease of the semidiurnal energy flux between the different modes also the fraction between first and second mode is changing which can be seen in **Figure 4.2** (c, f). The fraction of the first mode in relation to the total energy flux changes from 88.0±0.9 % during the no eddy period to 89.7±1.4 % during surface eddy 1 and 88.5±1.3 % during surface

eddy 2. During the subsurface eddy 1 period the ratio changes to 90.8±1.6 %, and to 92.2±0.9 % during subsurface eddy 2.

Comparing the ratio of coherence of the time series, it is observed that the ratio between the M_2 coherent and the semidiurnal part of the energy flux goes from 84 % (86 % mode 1, 69 % mode 2) during the no-eddy period down to 75 % (79 % mode 1, 35 % mode 2) during surface eddy 1, and to 75 % (80 % mode 1, 17 % mode 2) during surface eddy 2 (**Table 4.1**). During the subsurface periods the ratio of coherence is 81 % (84 % mode 1, 47 % mode 2) and 81 % (86 % mode 1, 9 % mode 2) for subsurface eddy 1 and subsurface eddy 2 respectively. The decrease of coherence and simultaneous increase of incoherence during eddy periods in comparison to the no-eddy periods is particularly pronounced in the second mode but can also be identified in the first mode.

Focusing on the M_2 coherent part of the energy flux, it is 34 % lower for the sum of modes 1 and 2 (-31 % for mode 1 and -72 % for mode 2) during the surface eddy 1 period compared to the no-eddy period and 35 % lower (-29 % for mode1, -87 % for mode 2) during the surface eddy 2 period compared to the no-eddy period (**Table 4.1**). Comparing the subsurface eddy periods with the no-eddy period results in a 6 % lower (-1 % for mode 1, -53 % for mode 2) and a 1 % higher (+10 % for mode 1, -91 % for mode 2) M_2 coherent energy flux for the subsurface eddy 1 and subsurface eddy 2 period respectively. The fraction of the first mode of the M_2 coherent part in relation to the total M_2 coherent part of the energy flux is 91.16±0.35 % during the no eddy period. The fraction of the first mode increases during eddy interaction periods to 96.06±0.0004 % during surface eddy 1 and to 98.01±0.008 % during surface eddy 2. During subsurface eddy 1 the fraction is 95.48±0.007 %, and during subsurface eddy 2 the fraction is 99.15±0.003 %.

To quantify the distortion caused by the individual eddies, the distortion parameter *d* was computed for each individual eddy period. It is 0.05, for the sum of mode 1 and mode 2 (0.05 and 0.08 for modes 1 and 2, resp.) during the no eddy period (**Table 4.1**). It increases during the surface eddy period 1 to 0.10 (0.11 for mode 1, 0.13 for mode 2) and to 0.10 (0.11 for mode 1, 0.09 for mode 2) during the second surface eddy period. It further increases during the subsurface eddy period 1 to 0.11 (0.11 for mode 1, 0.16 for mode 2) and to 0.08 (0.08 for mode 1, 0.14 for mode 2) during the second subsurface eddy period. For comparison, in Dunphy et al. (2017) the distortion metric increases from 0.08 to 0.21 in the zonal component and from 0.04 to 0.50 in the meridional component from mode 1 of the energy flux by interaction with a quasigeostrophic turbulent field in numerical experiments.

Regarding the changes in potential and kinetic energy during the different eddy phases one can identify a decrease of potential energy and an increase of kinetic energy when eddies are present in comparison to periods where no clear eddy activity can be identified for the sum

of mode 1 and mode 2 **Table 4.1**. Whereby the increase in kinetic energy during eddy periods lies solely in the first mode compared with the no eddy period, while in the second mode one can identify lower kinetic energy during all eddy events compared to the no eddy period. The decrease of potential energy during eddy events compared to the no eddy period can be detected during all eddy events and can be seen also in both modes.

The periods of elevation in the ratio r_ω between potential and kinetic energy fit together with the defined eddy periods. Especially in the surface eddy periods r_ω has a higher mean and a higher variability, indicating an intrusion of other frequencies. r_ω is higher during the eddy periods than during the periods where no eddy is present (**Figure 4.4**). During the no-eddy period r_ω is 1.38±0.07 and therefore lower than the theoretical value of 1.82. During the first surface eddy period r_ω is 3.17±0.48 and 3.89±0.65 during the second surface eddy period, with peaks up to almost 40. In the subsurface eddy 1 period r_ω is 2.06±0.26 and 2.01±0.29 during the subsurface eddy 2 period.

4.2 Discussion

The following discussion is split into section 4.2.1 where I give an overview of the temporal variability of the internal tide energy flux for the entire observation period. While in section 4.2.2. I discuss the time series in relation to the eddy events which were defined in section 4.1.2.

4.2.1 Overview of the internal tide variability

The strength of the energy flux, their steady direction away from the generation site, the presence of a spring-neap variability and the dominance of mode 1 are comparable with other in-situ measurements of semidiurnal internal tides. For example, Alford and Zhao (2007a) found in 80 historical mooring measurements energy fluxes in the order of 1 kW m^{-1}, while in the Luzon Strait internal tide energy fluxes of more than 60 kW m^{-1} were observed (Alford et al., 2011). The dominance of the mode 1 energy flux is consistent with findings by Vic et al. (2018) and by open-ocean mooring estimates of energy flux from the Internal Waves Across the Pacific experiment (IWAP, Zhao et al., 2010). This dominance of the first mode might be expected given the strong weighting of baroclinic pressure anomaly toward low modes (Nash et al., 2005). In comparison to Vic et al. (2018), I do not find a high directional variability of internal tides which they linked to multiples sources around their mooring. This is likely due to the position of the mooring where the interference pattern of different waves from

different sources form a beamlike structure with a distinct direction. The directional variability on short time scales might be attributed to reflection, scattering and interferences between waves from different sources (Zaron & Egbert, 2014). About 81 % of the sum of mode 1 and mode 2 energy flux is M_2 coherent (86 % for mode 1, 35 % for mode 2), this agrees with observations by Liu et al. (2016), who found a fraction of 35 % coherent motion in the semidiurnal internal tides. The higher coherence of the mode 1 internal tides is most likely due to the position of the measurements inside a tide beam because interferences enhances coherent motions of semidiurnal internal tides (B. Li et al., 2020). Internal tides are most coherent in internal tide beams, and right near the generation site, and more incoherent elsewhere. This means, that a linear superposition of internal tide energy fluxes does not cause a loss of coherence and that as soon as one moves away from the main beams (also close to the generation site) the incoherence increases (Buijsman et al., 2017). Therefore, internal wave interference should equally affect the magnitudes of both, the entire semidiurnal internal tide and its coherent part.

The observations of the spring-neap-variability in the internal tide energy flux agree with modeling results from Holloway and Merrifield (2003) inside a tide beam at the Hawaiian Ridge. They observed in their numerical simulations that energy fluxes at spring tides are substantially stronger than the sum of M_2 and S_2 fluxes and that baroclinic velocities vary in amplitude over the spring-neap cycle by approximately 50 %, but that the overall structure of the tide beam maintains. Depending on the covariance in the energy flux equations, the energy flux at baroclinic spring tides can be substantially greater than the sum of the M_2 and S_2 components. However, averaged over a spring-neap cycle the energy flux equals the sum of M_2 and S_2 when neglecting incoherent components. As close to the Hawaiian Ridge, the M_2 and S_2 tidal components are the two dominant constituents of the internal tide south of the Azores with the N_2 and K_2 tidal components playing a lesser role but still causing variations in the spring-neap amplitudes. The mean meridional barotropic velocities at the mooring location during the entire deployment period of the mooring from the TPXO9 dataset are 1.41 cm s^{-1} for M_2, 0.44 cm s^{-1} for S_2, 0.31 cm s^{-1} for N_2 and 0.11 cm s^{-1} for K_2. This means that there are small modulations of the spring tide amplitudes resulting from the difference between $M_2 + S_2$ and $M_2 + S_2 \pm N_2 \pm K_2$. Diurnal components of the energy flux are neglected in this study and are weak in compare to semidiurnal components. For example, the K_1 baroclinic energy flux generated between the islands of Oahu and Kauai is about 7 % of the energy flux of the M_2 component (Holloway & Merrifield, 2003). The variability between spring and neap tides could be expected to arise from the different wavelengths of the M_2 and S_2 internal tides. This leads to slightly different ray paths for each tidal constituent in the tide beam. However, these differences are expected to produces insignificant changes to the beam pattern within a couple of wavelengths from the generation site because they are only a few kilometers compared to their overall wavelength (Holloway & Merrifield, 2003). The

modulations in energy flux are strong and are in better agreement with observations from Alford and Zhao (2007a), where the spring magnitude is exceeding that at neap by a factor of 5-10. In general, the temporal agreement between the fortnightly phasing of lagged barotropic forcing and both energy and energy flux is good when energy and flux are strong. At weaker signals the energy and energy flux at moorings are usually still in phase with each other but are not necessary in phase with the forcing. The strength of the individual spring tides appears not always to be simply related to the forcing, which could be consistent with low-frequency related modulations of the generation process (Mitchum & Chiswell, 2000). These modulations are due to the varying internal tide amplitude when the stratification changes. One can expect that changes in the stratification, that act to deepen the pycnocline, should positively correlate with the low-frequency modulations in the M_2 amplitude.

A poorer correlation with the barotropic tide and a higher variability in the direction of mode 2 energy flux compared to mode 1 is consistent with findings by Ansong et al. (2017), where historical mooring observations on a global scale were compared with a high-resolution numerical model (HYCOM). They also found almost constantly lower magnitudes of energy flux of mode 2 compared to mode 1. A larger incoherent proportion in the second mode in comparison to the first mode might be expected due the more complex structure of the second mode which makes it more susceptible for disturbances (Ponte & Klein, 2015; Rainville & Pinkel, 2006). Waterhouse et al. (2018) showed in mooring observations in an internal tide beam in the Tasman Sea, that about 25 % of the total semidiurnal energy flux was incoherent, which is in relative agreement with my observations. While the heading of their coherent energy flux is relatively steady, they demonstrate that the incoherent internal tides caused large short-term variability in both the magnitude and heading of the total energy flux. This could explain the higher directional variability in mode 2 of my in-situ observations due to higher incoherence, and suggests that even in a region with a strong coherent internal tide, the incoherent tide can still significantly alter the tidal energy flux (Savage et al., 2020).

The total energy (sum of potential and kinetic energy) varies by an order of magnitude and is in order of 1 kJ m^{-2}, which agrees with observations from 80 historical mooring records from Alford and Zhao (2007a). For a freely propagating linear internal tide a dominance of kinetic energy over potential energy is expected and can be seen also in the in-situ observations as the ratio r_ω between kinetic and potential energy (Alford 2007). However, it is possible, that two waves of equal amplitudes are propagating in opposite directions which can display offset nodes and antinodes in kinetic and potential energy. This would invalidate the ratio r_ω and lead to a periodic patter in it (Alford et al., 2006; Nash et al., 2004). The Baroclinic energy density varies substantially between spring and neap values by more than a factor of 3. This agrees with findings by Holloway and Merrifield (2003) who additionally found that the sum of spring values are stronger than the sum of M_2 and S_2 during spring times. The fraction of

mode 2 energy density (about 20 %) is higher than the fraction of the total mode 2 semidiurnal energy flux (about 9 %) which agrees with Zhao (2018) where mode 2 usually contributes significantly to energy but less to energy flux. This suggest that the mode 2 internal tide field is subject to multi-wave interferences (Alford et al., 2006; Martini et al., 2011; Nash et al., 2006).

Beside the strong spring-neap variability, I found a strong temporal variability on sub-seasonal time scales, that I attribute to interaction with the mesoscale flow. The presence of eddies and their influence on the energy flux is evaluated in the upcoming section. I did not found any other temporal variability for example in terms of seasonal changes in the semidiurnal energy flux, which reinforces the assumption that the temporal variability of internal tides is primarily due to the presence of mesoscale eddies, with the constant forcing of the tides (Ponte & Klein, 2015; Zaron & Egbert, 2014). Also, Shriver et al. (2014) found that energy flux in the vicinity of strong generation regions, like the seamount chain south of the Azores, tend to be less variable than regions of weak forcing.

4.2.2 Internal tide variability in the context of eddy events

In-situ measurements of the decay of the internal tide energy away from the generation site help to estimate the amount of energy that is available for mixing. However, due to interference of waves from multiple generation sites (Rainville et al., 2010; Zaron & Egbert, 2014) and to constructive and destructive interference from interaction with mesoscale eddies (Dunphy & Lamb, 2014), the correct interpretation of in-situ measurements is complicated. The decrease of the energy flux in the low modes during the eddy periods can be explained by their interaction with mesoscale motions (Dunphy & Lamb, 2014; Dunphy et al., 2017; Kelly & Lermusiaux, 2016; Kelly et al., 2016; Kerry et al., 2014; Rainville & Pinkel, 2006; St. Laurent & Garrett, 2002) which affects the propagation of all modes, although the effect increases with increasing mode number. These interactions can modify the propagation path, group and phase speed, lead to wave reflection and/or transfer energy from lower to higher modes which is conducive to increased wave breaking and in turn may lead to stronger local mixing. Not only the strength of the eddy is important for the interactions with the energy flux and its consequent damping, but also the length (time, distance) available for the interaction. Where the latter aspect could even be more important. Kerry et al. (2014) found that the mesoscale circulation enhances the internal tide dissipation by a factor of 2-5 when subtidal circulation is considered, compared to a horizontally uniform stratification. They relate this enhanced dissipation to interaction with sheared currents in the upper ocean which

may cause scattering of low-mode internal tides to higher modes, which have a greater downward propagation of energy and may therefore contribute to deep-ocean mixing (Whalen et al., 2018). The different response of mode 1 and mode 2 to the presence of the eddies may be attributed to the different susceptibility of the modes to interact with the modal structure of the eddies. Because of its more complex structure, the second mode is more susceptible for disturbances, especially in a depth of about 2000 m where the gradient of horizontal velocity is higher than in the first mode and where the maximum of the subsurface eddies are located (**Figure 4.5**). A stronger influence onto the second mode was also found by (Dunphy et al., 2017) who used the distortion metric in numerical experiments to confirm that the variability increases when a low mode internal tide propagates through a quasigeostrophic turbulent field. With my observations I can confirm an increase in the distortion metric during eddy time periods and that mode 2 waves are indeed distorted more strongly than mode 1 waves. Furthermore, Savage et al. (2020) demonstrated that a background flow has a larger overall effect on mode 2 than on mode 1 for internal tide energy fluxes in a tide beam by a comparison of their energy advection.

During eddy periods, one can observe higher values and a higher variability of the ratio between kinetic and potential energy, r_ω. This consistency check suggests an intrusion of energy by waves of other frequencies into the semidiurnal band, which are the surface and subsurface intensified eddies. Values below the theoretical value can occur due to the initial bandpass filtering of the velocity and temperature time series. One has to be careful by using r_ω for this purpose, because in practice in-situ measurements are often too noisy to be used for this (Alford & Zhao, 2007a). Nevertheless, for this time series the use of r_ω seems to be suitable because of the significantly higher values of r_ω during eddy periods in compare with the no-eddy period, and can therefore at least serve as an indicator for the detection of intrinsic frequencies. Interesting to note is that the increase in r_ω during eddy periods seem to be a result of a simultaneous increase of kinetic energy in mode 1 and a decrease of potential energy in both mode 1 and mode 2, while the kinetic energy in mode 2 is also decreased. This potentially surprising behavior of kinetic energy might be due to a mode 1 baroclinic vertical structure of the eddies (McWilliams, 1985). The eddies could inject energy in mode 1, while in mode 2 the energy might be scattered directly into higher modes. Furthermore, for mode 1 the decrease in potential energy seems to be of higher importance for the increase in r_ω during the surface eddy periods in compare with the no-eddy period, while during subsurface eddy periods the increase in kinetic energy seems to be more relevant than the decrease in potential energy.

An internal tide signal which is measured at a fixed location can become incoherent because of temporal changes in its phase and amplitude. The loss of phase coherence of propagating internal tides can be attributed to refraction caused by Doppler shifting due to varying subtidal

currents, and by varying background relative vorticity as well as by varying background stratification (Zaron & Egbert, 2014). My results support the idea that eddy interaction increases incoherence and that the effect becomes more important with increasing mode number. Although several studies based on numerical models and a combination of model and satellite altimetry (e.g. Ponte & Klein, 2015; Rainville & Pinkel, 2006) have shown this interaction, here such effect is shown from in-situ observations. Stronger incoherence of the internal tides affect their predictability and may influence the ability to estimate the ocean circulation from high resolution altimetry (Richman et al., 2012). The higher share of mode 1 in compare to mode 2 in the M_2 coherent part of the energy flux during eddy periods displays that the vast majority of the coherent internal tide energy flux lies almost solely in mode 1. The higher incoherence of the second mode during the subsurface eddy periods in comparison to the surface eddy periods can again be attributed to the vertical mode structure of horizontal velocity and its stronger gradient at a depth of 2000 m where the subsurface eddies are strongest. The observation of an increase in incoherence by eddy interaction are further supported by B. Li et al. (2020), who investigated the coherent and incoherent features of internal tides in the north South China Sea on observations and numerical simulations. They found that mesoscale eddies not only increase the intensity of background currents, but also induce horizontal variations of density which leads to an increase in incoherent signals. Furthermore, semidiurnal internal tides are more sensitive to these influences which make them more incoherent than diurnal internal tides.

Another aspect that needs to be investigated when considering modal internal tide energy flux, is the change in stratification caused by the presence of eddies, and whether these changes in the stratification have a considerable impact on the resulting mode shapes. To answer this, I assumed that the main density changes in the stratification profile are caused by temperature, leaving salinity constant over time. I took the salinity values from the repeated CTD casts close to the mooring location, which I used for the stratification in the first place, and calculated “pseudo” stratification profiles for each timestep with the temperatures from the mooring. I then calculated mean stratification profiles for the two surface eddies, the no-eddy and the two subsurface eddy time periods and computed the corresponding mode structure. The resulting differences in the mode structure are marginal and more pronounced in between the different deployment periods (surface eddy 1 and subsurface eddy 1 during ET-1 and surface eddy 2 and subsurface eddy 2 during ET-2) than between the different eddy phases, and can be seen in **Figure 4.8**. This might be due to a shift in the stratification during the mooring deployment, rather than the influence of the eddies. Therefore, I can exclude that the use of a temporally constant stratification strongly affects my energy flux calculation. This is in contrast to the results of Zaron and Egbert (2014) who found that refraction, caused by changes of the background stratification, is one of the main drivers for the variability of the internal tide response at the Hawaiian Ridge. A possibility for

this difference might be that the changes in stratification are in this case too weak to yield this effect. In general, reflection and scattering of internal waves occur when they propagate across horizontally varying topography or stratification. In my case the horizontal buoyancy gradients are relatively weak, therefore topographic effects should dominate (Q. Li et al., 2019).

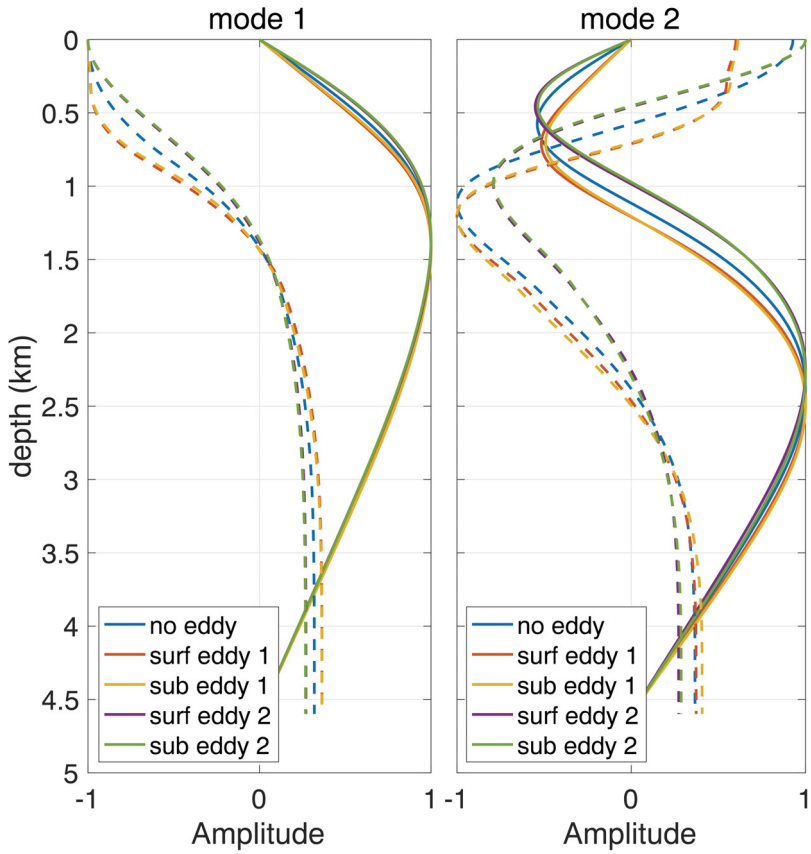

***Figure 4.8**: Structure of the first two vertical baroclinic modes for vertical displacement (solid lines) and horizontal velocities (dashed lines) during no-eddy (blue), surface eddy 1 (red), subsurface eddy 1 (yellow) surface eddy 2 (purple) and subsurface eddy 2 (green) periods show a negligible impact of the eddy induced changes in stratification on the mode structure.*

To further investigate the influence of mesoscale eddies on the energy flux variability, I calculated the power spectra of the amplitude of modal vertical and horizontal velocities (**Figure 4.9**). To have a better readability, the y-axis is multiplied with the frequencies ω of the x-axis to avoid a logarithmic scale and the x-axis is scaled by the forcing frequency M_2 to directly see the different harmonics of the M_2 frequency. The spectra show higher peaks during the no-eddy periods than during the four eddy periods in all velocity components of the second mode, supporting the observations above where eddy interaction is dampening the energy flux in the first and second mode. It might be an indication of a scattering of energy towards higher modes (not resolved by the mooring), which could ultimately lead to an increased local dissipation. In the first mode one can see the highest peak being in the no-

eddy period only in the vertical velocity component *w*. While in the horizontal velocity components all peaks are similar to each other. Here are several plausible hypotheses:

1) Rainville and Pinkel (2006) observed that mesoscale variability can lead to refraction of the propagation path of internal tides. This leads to a shift of the propagation path of the individual modes, whereby the effect increases with mode numbers. This reduces coherence and, as we observed in our observations, increases incoherence of the energy flux during eddy periods, especially in the second mode.

2) Given that the pattern of internal waves emanating from different topographic generation sites is non-uniform, the eddies could shift the interference pattern of single waves from different sources (Dunphy & Lamb, 2014; Kelly & Lermusiaux, 2016; Rainville et al., 2010), and might shift even the interference pattern of the different modes individually. An indication towards this explanation is the stronger directional variability during the eddy periods in compare with the no-eddy period.

3) The eddies could, because of their mostly horizontal mode 1 structure, pump energy into the first horizontal mode which is then directly scattered away into higher modes. This theory might explain why we do not see differences in the individual eddy phases in the horizontal component of mode 1, but it remains questionable why the eddies would pump energy specifically into the M_2 frequency. An indicator towards this theory is the increase of kinetic energy only in mode 1 during eddy periods.

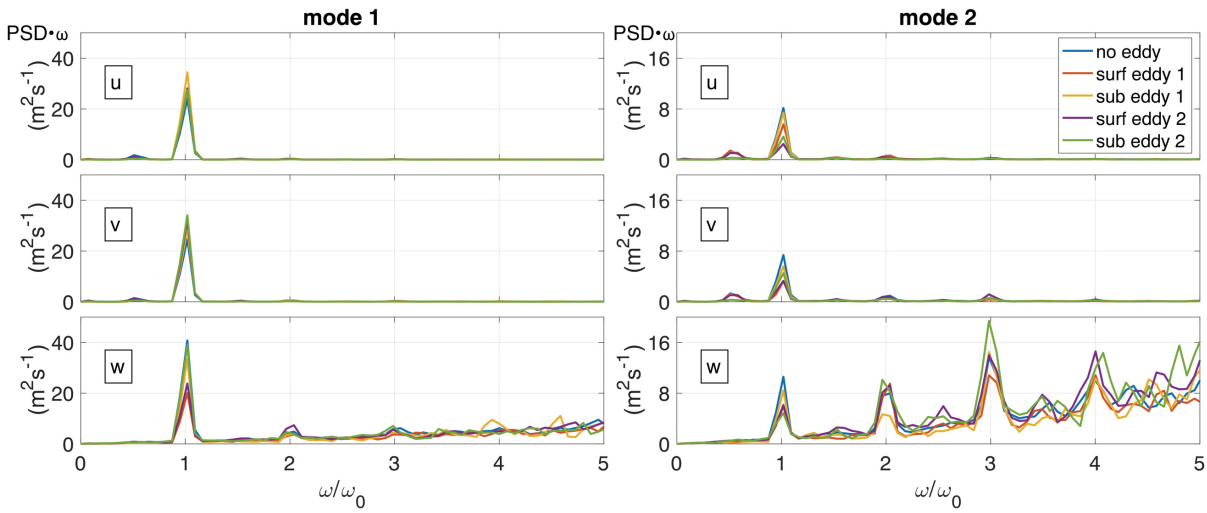

***Figure 4.9**: Power spectral density (PSD) of mooring observations after projection of horizontal (u,v) and vertical (w) velocities onto mode 1 and mode 2 shows differences between no-eddy (blue), surface eddy 1 (red) and subsurface eddy 1 (yellow), surface eddy 2 (purple) and subsurface eddy 2 (green) phase. The influence of the eddies is most prominent for the vertical velocity but also occur in mode 2 in all velocity components. X-axis is scaled by forcing frequency $\omega_0 = M_2$ and Y-axis multiplied with frequencies ω.*

The differences in the first mode between vertical and horizontal velocity components could explain why the second mode of the energy flux is more strongly affected by the eddies. The reduction of energy flux via eddy interaction would rely in the first mode only on the vertical (displacement), while in the second mode also the horizontal velocities are affected. It remains unclear which process is the main driver for the different behavior of the horizontal component in the first mode or in which way the individual effects act on the observed internal tides as a whole. Interesting to note is a variety of smaller peaks at each harmonic of the M_2 frequency, strongly emphasized at the vertical component (*w*) of mode 2 (**Figure 4.9**). They result from the scattering of energy to higher frequencies which is assumed to be a result of various wave-wave interactions that have been excited (Dunphy & Lamb, 2014; Dunphy et al., 2017). One can argue that by bandpass filtering only around the generation frequency M_2, some of the energy in the semidiurnal band will not be considered in the calculation of the energy flux of the internal tide as it is transferred to higher harmonics. Especially in the second mode, the second and third harmonic of M_2 seem to have a similar amount of energy as the generation frequency.

5 Generation of near-inertial internal waves during a strong wind event in an internal tide beam

Beside the existing lack of long-term observations of internal tides in a tide beam, there are also only few observations regarding the near-inertial internal gravity waves in such beams. Furthermore, there are no observations which can clearly separate a specific wind event from a background state of near-inertial energy flux. The 20 consecutive months of mooring observations in the tide beam south of the Azores, gives the opportunity to investigate this temporal variability. Due to the location of the mooring away from common storm tracks, the mooring offers the possibility to quantify the impact of strong wind events, when present, onto this background. The goal is to study how the temporal variability, with the usually intermittent occurrence of near-inertial waves, looks like and what its influencing factors are. Furthermore, how its characteristics, like the ratio between modes, are changing over time especially in the context of suddenly appearing strong wind events. In this chapter we look at similar parameters as for the internal tides and investigate the time series of energy flux, the time series of kinetic and potential energy and its modal composition. In section 5.1 I present the results of the in-situ measurements, which are discussed in section 5.2. A comprehensive list of all near-inertial internal wave energy fluxes as well as kinetic and potential energy that are discussed in this chapter are given in **Table 5.1**.

	Near-inertial flux (kW m^{-1})			Kinetic energy (kJ m^{-2})			Potential energy (kJ m^{-2})		
	Mode 1	Mode 2	**total**	Mode 1	Mode 2	**total**	Mode 1	Mode 2	**total**
Mooring total	0.27 ±0.03	0.21 ±0.02	**0.47** ±0.05	0.41 ±0.05	0.50 ±0.12	**0.91** ±0.17	0.02 ±0.002	0.06 ±0.006	**0.08** ±0.006
Mooring background	0.19 ±0.01	0.15 ±0.01	**0.33**± 0.02	0.26 ±0.03	0.28 ±0.02	**0.53** ±0.03	0.02 ±0.002	0.04 ±0.004	**0.06** ±0.005
Mooring wind event	1.32 ±0.53	1.18 ±0.34	**2.51** ±0.62	2.53 ±0.76	5.88 ±2.41	**8.41** ±3.25	0.06 ±0.004	0.14 ±0.04	**0.20** ±0.05

***Table 5.1**: Mean energy flux at the mooring in the near-inertial band and kinetic and potential energy for the entire deployment period (total), the background (from the beginning of the time series until 10 October 2018 and from 9 January 2019 until the end of the time series) and a strong wind event (from 10 October 2018 until 29 October 2018).*

5.1 Results

The following result section presents the general observations of the temporal variability of near-inertial internal wave energy fluxes during the mooring deployment. During this deployment a strong wind event was detected whose effects on the time series of energy flux and the time series of kinetic and potential energy is presented separately in section 5.1.2.

5.1.1 Time series of near-inertial internal waves

The time series of the energy flux in the near-inertial band shows minor variations in the first part until the appearance of a strong peak in mid of October 2018 followed by several smaller peaks until the beginning of January 2019. After that the time series appears as it was before the strong peak (**Figure 5.1**). The total mean of the near-inertial energy flux is 0.47±0.05 kW m^{-1} (0.27±0.03 kW m^{-1} for mode 1, 0.21±0.02 kW m^{-1} for mode 2). The highest peak in October reaches up to 6.34 kW m^{-1}, which is about 13.5 times higher than the mean of the entire time series. The amplitude of the energy flux is not dominated by either mode 1 or mode 2, which are contributing in a similar way to the total mean (**Figure 5.2** c).

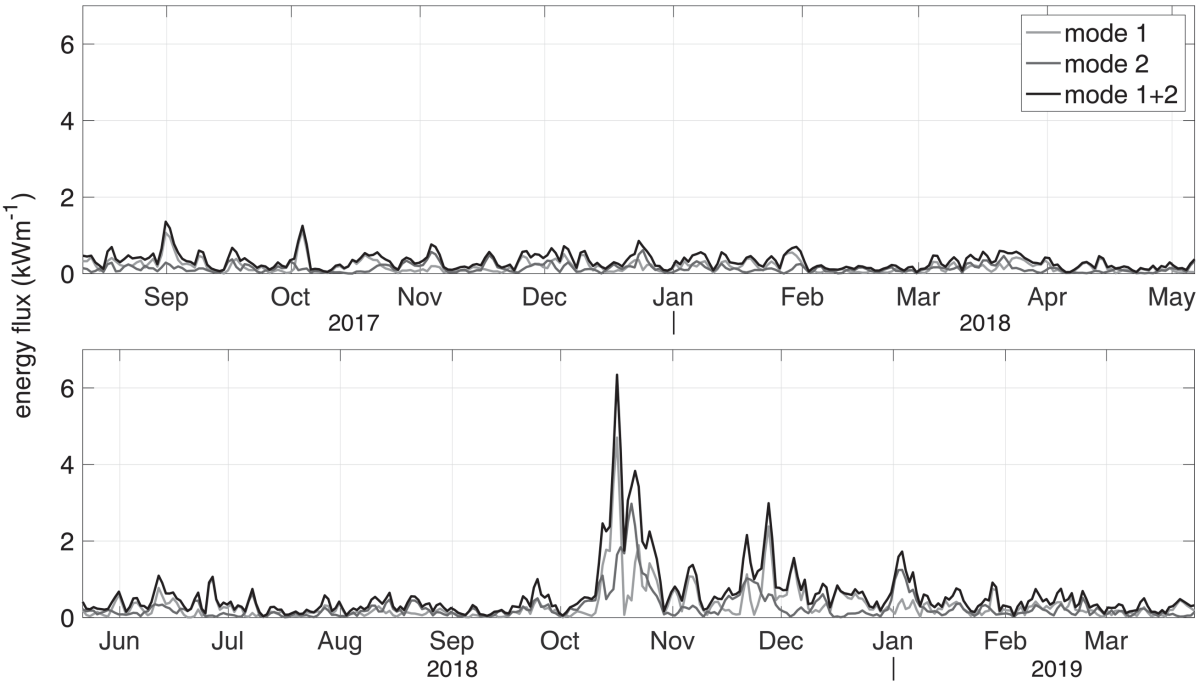

***Figure 5.1**: Time series of near-inertial energy flux shows minor variations in the first part of the time series until the appearance of a strong peak in mid of October 2018 which is followed by a variety of smaller peaks until the beginning of January 2019. Black: Sum of mode 1 and mode 2 of near-inertial energy flux from the mooring observations. Light grey and dark grey are the first and second mode of the near-inertial energy fluxes respectively.*

The near-inertial energy flux is not steady and varies in time and in direction (**Figure 5.2**). The mean direction of the mode 1 near-inertial energy flux is 181°±5°, whereas the mean direction of mode 2 is 175°±4°. In general, the direction of the energy flux has a higher variability than the internal tides in section 4, with few exceptions during the strong peaks from mid of October 2018 to the end of November 2018. In these instances, the energy flux is pointing with a stronger focus in southward (mid of October 2018) or northward direction (end November 2018). The fraction of the first mode in relation to the second mode is about 54±2 % for mode 1 and varies between 2 % and 99 %. The elevation in energy flux in mid to end of October is characterized by a primary domination of mode 1 followed by a domination of mode 2.

The time series of kinetic energy is greater than the time series of potential energy for the near-inertial band, as it the case for the semidiurnal band. In the near-inertial band, the energy is mostly dominated by mode 2 and shows generally a low variability during the entire period with three exceptions (**Figure 5.3**). In detail, the time series of potential energy shows a lower variability during the first deployment period until mid of May 2018 than in the second deployment period from mid of May 2018 until the end of the in-situ measurements. Also, the potential energy in the second mode has generally a higher variability than the first mode.

Here one can find the highest peak in the entire potential energy time series with about 650 J m^{-2} in the beginning of January. This peak is about 10 times higher than the mean of the entire mode 2 time series and coincides with a smaller peak in the energy flux time series (**Figure 5.1**). The mean of the potential energy time series is 0.08±0.006 kJ m^{-2} (0.02±0.002 kJ m^{-2} for mode 1, 0.06±0.006 kJ m^{-2} for mode 2). The mean of the kinetic energy time series is 0.91±0.17 kJ m^{-2} (0.41±0.05 kJ m^{-2} for mode 1, 0.50±0.12 kJ m^{-2} for mode 2, **Table 5.1**). The kinetic energy time series displays two strong peaks, one in mode 1 and one in mode 2 both in mid of October, which coincides with the highest peak in the energy flux time series (**Figure 5.1**). The peak in mode 1 reaches up to 6.21 kJ m^{-2}, while the peak in mode 2 reaches up to 17.99 kJ m^{-2} which are about 15 times and 35 times higher than their mean, respectively.

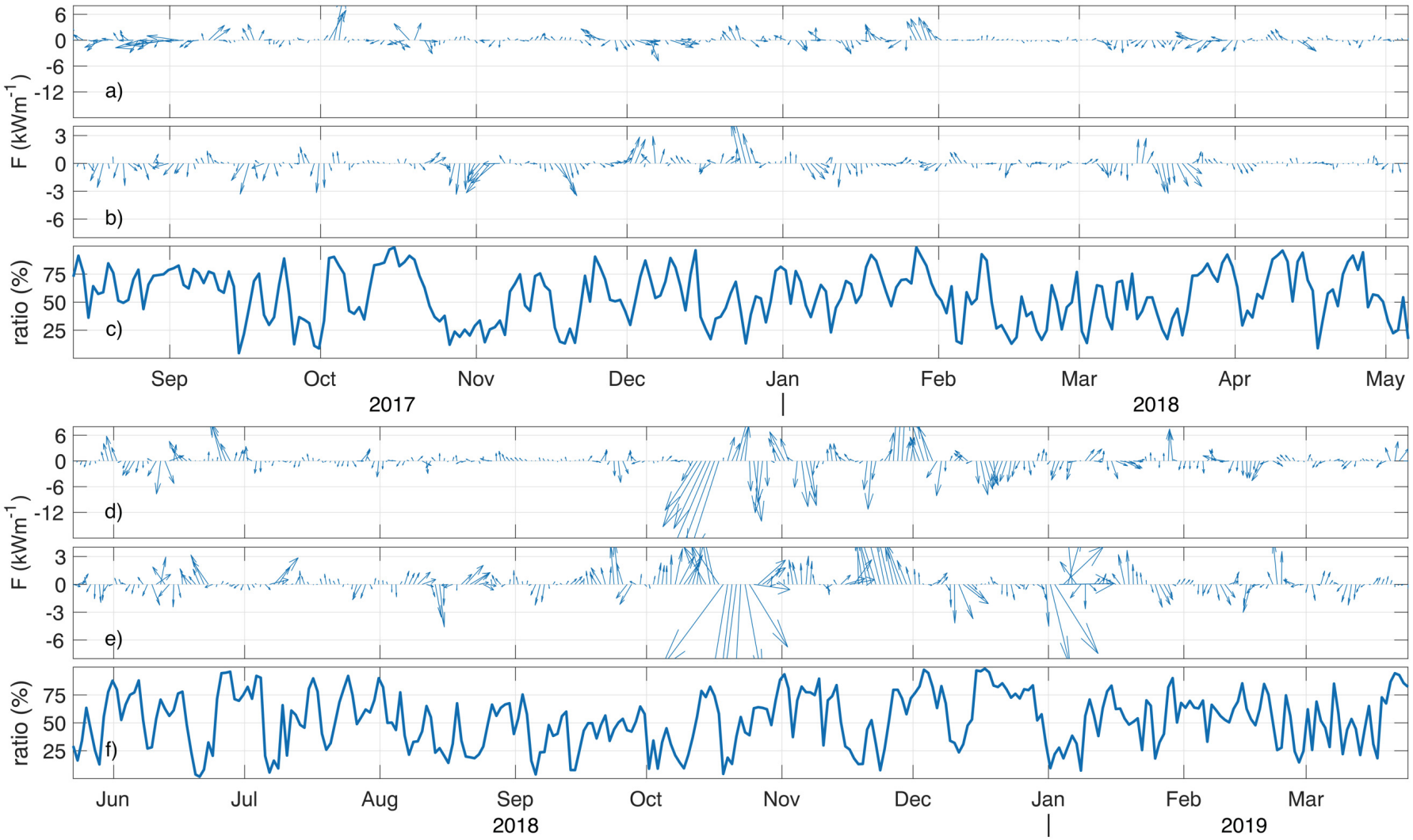

***Figure 5.2**: Directional variability and magnitude of the near-inertial energy flux for mode 1 (a, d) and mode 2 (b, e) from the mooring time series; note the different scaling of the y-axis for mode 1 and mode 2; ratio between first and second mode of energy fluxes (c, f); 80 % means that the combined mode 1 and mode 2 flux consists of 80 % mode 1 and 20 % mode 2 at the corresponding time.*

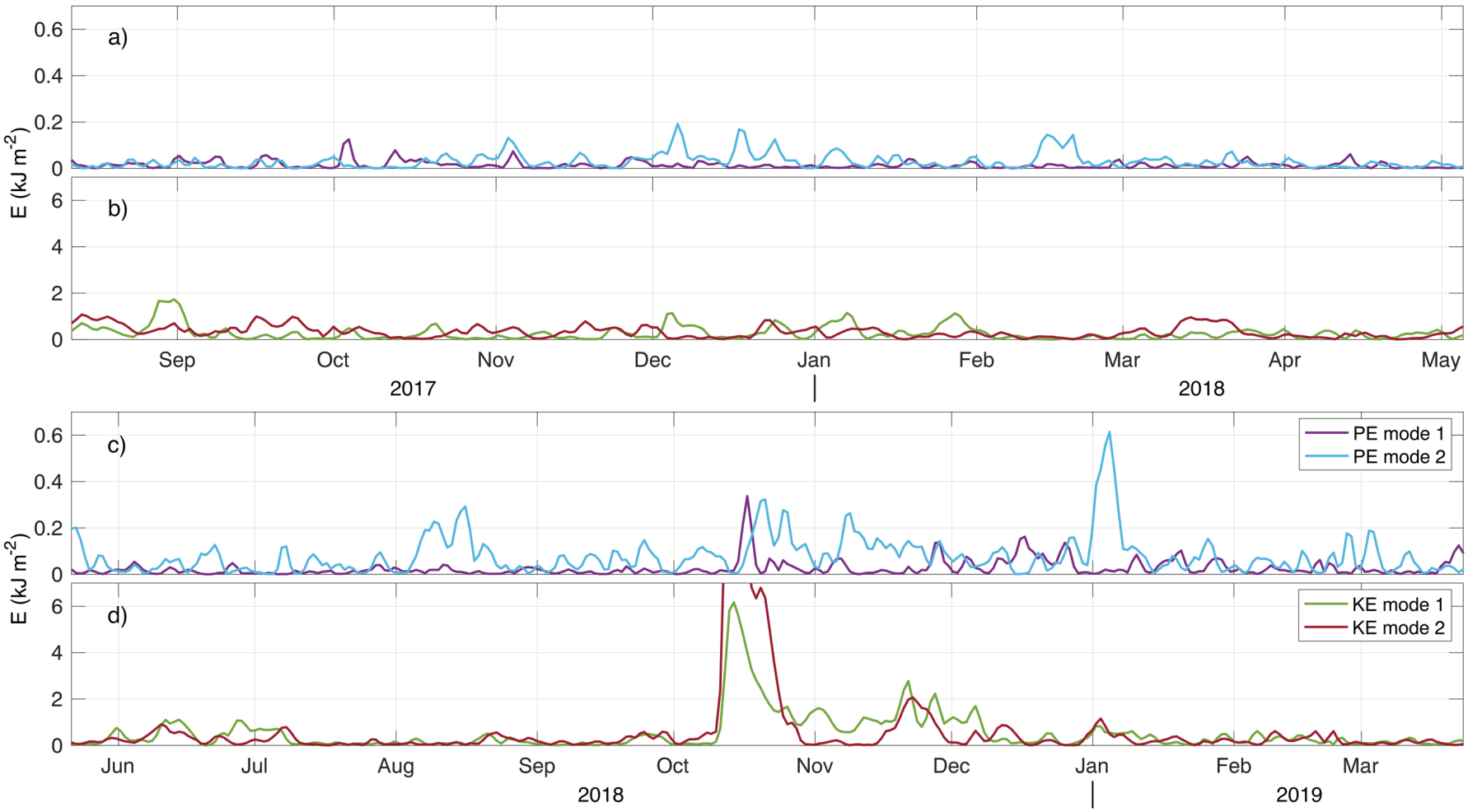

***Figure 5.3**: The time series potential (PE) and kinetic energy (KE) of the in-situ measurements for the first and second mode in the near-inertial frequency band as means over one wave period is mostly dominated by mode 2 and shows a low variability during the entire time series with few exceptions. The peak in mode 2 of kinetic energy reaches 17.99 kJ m^{-2} in d).*

5.1.2 The occurrence of a strong wind event in the near-inertial time series

The peaks in the time series of near-inertial energy flux, potential energy and kinetic energy are very prominent in comparison to the remaining time series of the in-situ observations. I formulated the hypothesis that this increase of the energy flux is caused by wind events in the study area. To test this, I analyzed maps of wind-speed and calculated wind power (equation [3.10]) from Copernicus Marine Environment Monitoring Service (CMEMS) datasets. Two similar CMEMS datasets for the wind speed and wind stress have been used because of the available temporal coverage of each individual dataset. Both datasets are the IFREMER CERSAT Global Blended Mean Wind Fields and contain meridional and zonal wind components. The first dataset (WIND_GLO_WIND_L4_REP_OBSERVATIONS_012_006) is used from the beginning of the mooring time series until the 31 December 2018. The second dataset (WIND_GLO_WIND_L4_NRT_OBSERVATIONS_012_004) is used from 1 January 2019 until the end of the mooring time series. Both datasets offer a 6-hourly temporal resolution and a spatial resolution of a 1/4°. While both datasets use remotely sensed surface winds derived from scatterometers and radiometers, the main difference between the two datasets is that the first one is reprocessed (REP) and the second one is near-real time (NRT). Usually, reprocessed products are more precise than NRT products, therefore errors in calculation where the second dataset is used are assumed to be higher. For the ocean surface velocities, the CMEMS dataset presented in section 4.1.2 is used.

By analyzing maps of wind speed and wind power, few strong wind events in the study region were identified, whereby only one of them agrees reasonably well with the time of the peaks in mid of October 2018 in the energy flux time series. The average wind speed of this strong wind event inside the green square in **Figure 5.4** b) was about 22 m s^{-1} on 12 October 2018 at noon. This corresponds to a strong gale with a Beaufort number of 9. Due to the 6-hourly temporal resolution of the windspeed dataset, strong gusts which are likely to be present during this wind event are not available, but are a likely contributor to the resulting near-inertial internal wave response. The area close to the seamount chain south of the Azores could be clearly identified as the generation site of these internal waves. This was achieved by calculating the group speed of the internal waves and following the dominant direction of the energy flux backwards which agrees with the wind power input in the green square in **Figure 5.4** b). Such a clear relation could not be made for the remaining peaks in the near-inertial energy flux time series.

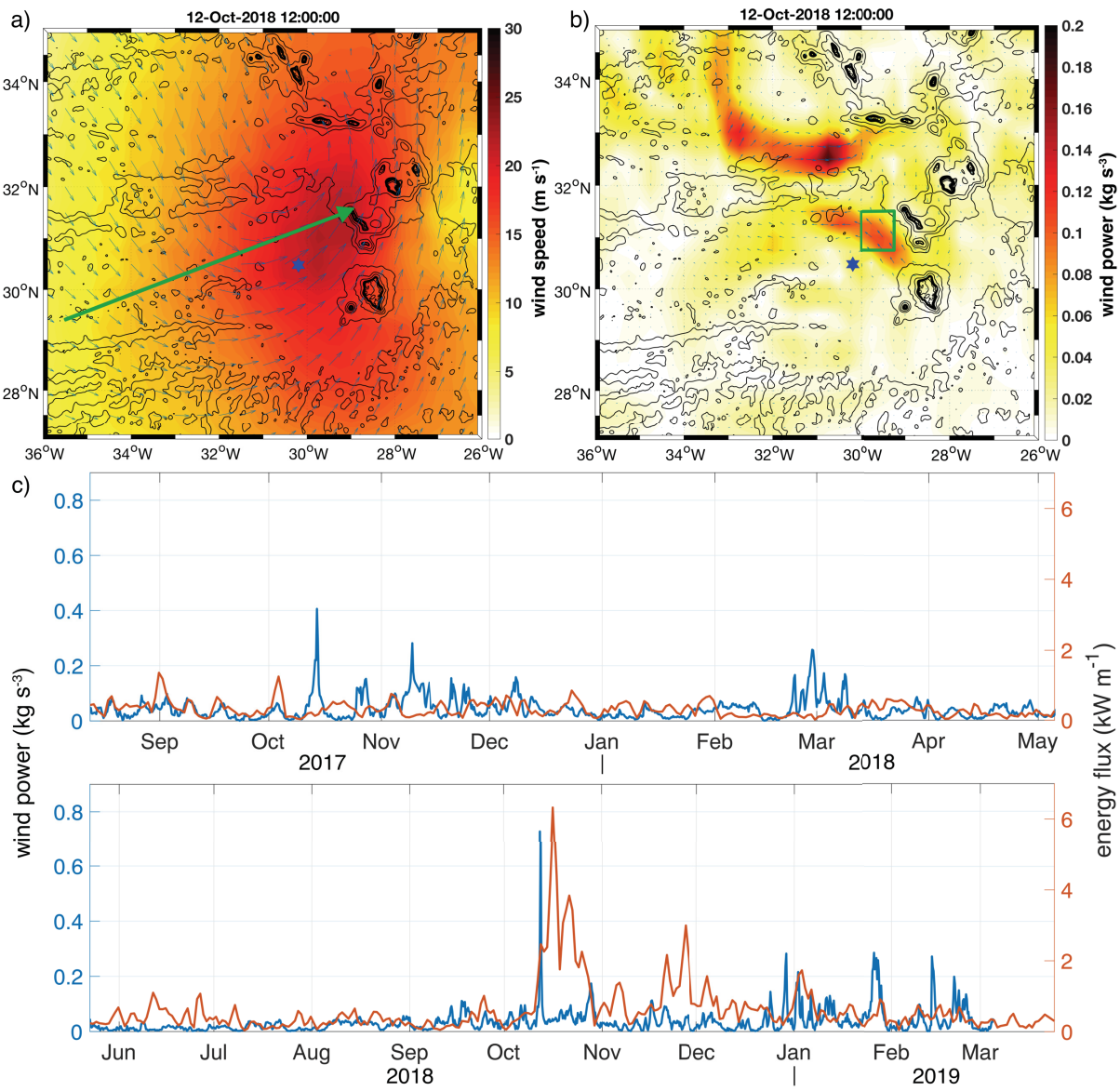

***Figure 5.4**: Windspeed and wind power around the mooring location can be related to peaks in near-inertial energy flux. a) shows the windspeed (background) and wind direction (blue arrows) in the study area south of the Azores at the strongest peak in the energy flux time series on 10 October 2018. Blue star: mooring location; green arrow: Track of the storm. b) shows the wind power (background) and wind power direction (blue arrows) in the study area south of the Azores at the strongest peak in the energy flux time series on 10 October 2018; green rectangle indicates area of which the wind power was integrated for c), which shows the area integrated wind power in relation to the sum of mode 1 and mode 2 near-inertial energy flux.*

The strong winds that are responsible for the near-inertial energy originated from the south-west and passes just north of the mooring, that is, in between the mooring location and the seamount chain south of the Azores (**Figure 5.4** a). The calculated wind power shows an elevation north-east from the mooring location during this wind event which agrees with the direction of the observed energy flux. I integrated the wind power in this area (**Figure 5.4** c),

displayed as the green rectangle in **Figure 5.4** b). The time series of the integrated wind-power is relatively low during the main part of the observation period with some minor peaks in October and November 2017, March 2018 and in January, February and March 2019. In addition, a major peak in mid of October 2018 can be seen, which coincides with the major peak in energy flux (considering the travel time of generated near-inertial waves). The strong wind event also caused a response on the ocean surface which can be seen in the velocity measurements of the mooring in **Figure 5.5**. The uppermost temperature sensor in a depth of about 100 m did not show any significant changes during this time and a deepening of the mixed layer cannot be resolved due to missing instruments at the mixed layer depth of 37 m. Nevertheless, one can identify a response of the vertical and horizontal velocities close to the ocean surface (**Figure 5.5**). For a better readability the displayed velocities have been 40-h low-pass filtered. The horizontal velocities depict a diurnal pattern of positive and negative values. The vertical velocities show an intensification close to the surface, while all velocity components display higher values in a depth of about 30 m to 70 m, propagating downward over time.

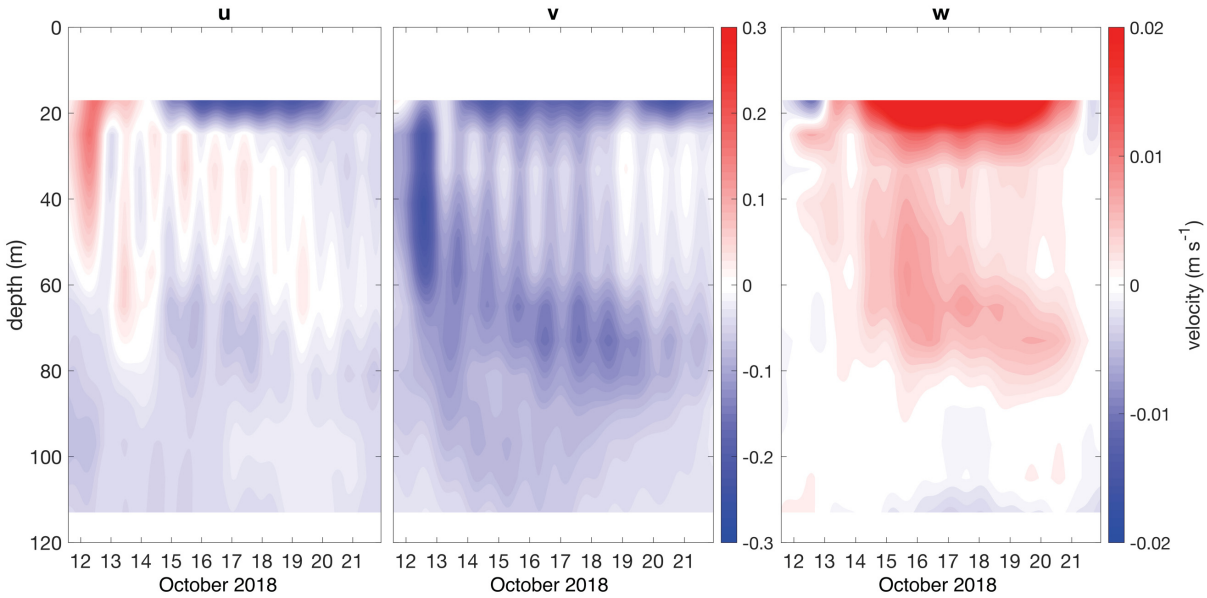

***Figure 5.5**: Horizontal (u,v) and vertical (w) velocities close to the surface from the Quartermaster ADCP during the strong wind event in October 2018 show an intensification close to the surface, and all velocity components display higher values propagating downward over time. The data was 40-h low-pass filtered for better readabilty.*

The prominent peaks in the time series of mode 1 and mode 2 energy flux as well as the peaks in the time series of mode 1 and mode 2 kinetic energy support the hypothesis that they are directly related to this strong wind event. I therefore define the mayor peak from 10 October 2018 until 29 October 2018 as the strong wind event for **Table 5.1**. The time from the beginning of the time series until 10 October 2018 and the time after the three peaks in energy

flux, from 9 January 2019 until the end of the time series are defined as the background of near-inertial internal wave energy flux. The mean amplitude of the energy flux during the strong wind event is 2.51±0.62 kW m^{-1} for the sum of mode 1 and mode 2 (1.32±0.53 kW m^{-1} for mode 1, 1.18±0.34 kW m^{-1} for mode 2), which is more than five times higher than the mean of the total observation period. The mean amplitude during the background is 0.33±0.02 kW m^{-1} for the sum of mode 1 and mode 2 (0.19±0.01 kW m^{-1} for mode 1, 0.15±0.01 kW m^{-1} for mode 2). Here, the amplitude of the energy flux during the strong wind event is about seven and a half times higher than the background. In other words, it would take about 152 days of the observed background energy flux to accumulate the same near-inertial wave energy flux that was generated during the strong wind event. The fraction of the first mode of the energy flux during the strong wind event is 49±9 %, compared to 53±2 % during the background. As stated earlier, the energy flux during the strong wind event is first dominated by mode 1 pointing with a stronger focus in southward direction, followed by a domination of mode 2 with a stronger focus in southward direction as well.

The mean amplitude of the kinetic energy during the strong wind event is 8.41±3.25 kJ m^{-2} for the sum of mode 1 and mode 2 (2.53±0.76 kJ m^{-2} for mode 1, 5.88±2.41 kJ m^{-2} for mode 2), while the mean amplitude of the potential energy is 0.20±0.05 kJ m^{-2} for the sum of mode 1 and mode 2 (0.06±0.004 kJ m^{-2} for mode 1, 0.14±0.04 kJ m^{-2} for mode 2). For the background the mean amplitude of kinetic energy is 0.53±0.03 kJ m^{-2} (0.26±0.03 kJ m^{-2} for mode 1, 0.28±0.02 kJ m^{-2} for mode 2). The mean amplitude of potential energy for the background is 0.06±0.005 kJ m^{-2} (0.02±0.002 kJ m^{-2} for mode 1, 0.04±0.004 kJ m^{-2} for mode 2).

5.2 Discussion of the effect of a strong wind event in relation to the background state

Near-inertial internal waves are generally more complex to analyze due to their temporally and spatially strongly varying generation mechanism by the wind in comparison to the steady forcing of internal tides by the barotropic tide. The energy flux observed at the mooring location can been seen as a realization of the background near-inertial energy flux induced by the wind at various places around the mooring location with the exceptions of the peaks between beginning of October 2018 until January 2019.

In general, the observed energy fluxes agree well with other observations and are in the same order of magnitude than earlier studies. For example, Alford (2003b) showed a time mean energy flux of approximately 0.5 kW m^{-1} at most of the approximately 80 mooring sites examined in their study (red arrows in **Figure 1.5**) with nearly always equatorward propagation (Alford et al., 2016). They showed that near-inertial waves have an energy flux and energy similar to those of internal tides and also radiate an appreciable fraction of their energy away from their respective generation site. This long-range propagation of near-inertial internal waves is important for their potential contribution to deep mixing. In this context it is important to know how much of the wind work at the surface penetrates to the deep ocean. Simmons and Alford (2012) found that about 16% of near-inertial wave energy radiates out of the mixed layer as low mode waves (season dependent). Other studies of near-inertial energy fluxes often show a seasonal variability with higher values in winter due to stronger winds and a higher wind variability (Alford, Cronin, et al., 2012; Alford & Whitmont, 2007; Silverthorne & Toole, 2009). In this study one does not see such a clear correlation in seasonality of the energy flux, despite the more frequent occurrence of strong wind events during winter. The occurrence of the peaks in energy flux in winter during the second year of the mooring deployment are likely more related to the pathway of the storm caused by any wind event at any given time during the year (**Figure 5.1**). The temporal resolution of the 6 hourly mean wind data from the CMEMS data sets which were used to identify the strong wind event, have a direct influence on the estimated wind power because strong wind bursts are not included. The absence of these bursts can result in an underestimation of the wind power input (Jiang et al., 2005; Rimac et al., 2013). This strong dependency is also the reason why it is not possible to give a more precise estimation about the relation of energy input into the mixed layer and about how much energy is then radiated away as near inertial waves. This estimate is further hindered by the fact that a single point mooring cannot display the spatial structure of the emerging internal waves. The amount of energy in near-inertial motions at a given site is then a combination of a local response to the wind forcing and waves that have travelled from far away. Two aspects that further emerge out of the distant meridional propagation are that the near-inertial waves could arise from continuum waves with $\omega \gg f$ which are propagating poleward until they reach the local Coriolis frequency (Fu, 1981), and that near-inertial waves which are generated near the Coriolis frequency could propagate equatorward until their frequency becomes $2f$ at which they would become unstable due to the parametric subharmonic instability (PSI) (Komori et al., 2008; Nagasawa et al., 2000; Niwa & Hibiya, 1997).

The dominant direction of the near-inertial energy flux should be southward in the northern hemisphere towards the equator because of their generation at the lower end of the range of frequencies for propagating internal gravity waves (between the local Coriolis frequency and the buoyancy frequency). As seen in **Figure 5.2** (a, b, d, e) the direction of the energy flux is

highly variable and is pointing occasionally in northward direction which can be explained by the generation of near-inertial waves slightly above the local Coriolis frequency. Due to the initial bandpass filtering around the Coriolis frequency *f*, these waves are fully taken into the calculation, but should be able to propagate only slightly toward the pole on a beta plane. They quickly reach a turning latitude where their frequency is equal to the local value of *f*, which is higher than that at their generation latitude, and are then reflected towards the equator (Alford, 2003a). This implies that most of the northward traveling energy fluxes in the time series must be generated relatively close to the mooring location until they reverse in direction. Another possibility for northward propagating near-inertial internal waves is the reflection by the bathymetry (similar to internal tides), but due to the absence of relevant topographic features south of the mooring location, this scenario is less likely.

Like the time series of near-inertial energy flux, the time series of kinetic energy in the near-inertial band is a good representation of the background state except for the strong peaks in October 2018 and its subsequent peaks until January 2019 (**Figure 5.3**). The order of magnitude of the energy from the near-inertial waves is comparable to the energy in the internal tides, as found in Alford (2003a) and in my study. Furthermore, Alford (2003a) as well shows the dominance of kinetic energy over potential energy, where the ratio of kinetic energy to potential energy is greater for near-inertial waves than for internal tides. This dominance is a result of the frequency much closer to *f* of near-inertial waves than internal tides, and results in smaller vertical displacements for the same energy. These small displacements combined with their intermittent appearance precludes near-inertial waves to be detected with satellite altimetry (Ray & Mitchum, 1996; Zhao & Alford, 2009; Zhao et al., 2012). The observed higher variability in the potential energy time series during the second deployment period of the mooring starting in May 2018 is likely caused by the repositioning of the ADCP closer to the surface (**Table 2.1**). As seen in equation [3.8] the potential energy is calculated via the stratification and the vertical displacement. Despite the usually lower displacement in the upper part of the water column the effect of the stronger stratification at this depth is mainly influencing the calculations, making them more susceptible for changes in the displacement. Moreover, the peak in the potential energy time series in the beginning of January is correlated with a peak in the energy flux time series. Where this peak in the potential energy comes from remains unclear. One possibility might be the influence of a surface intensified mesoscale eddy present at that time (cf. chapter 4.1.2) but this could not be verified.

The possibility of interaction between near-inertial waves with mesoscale eddies was already identified by Weller (1982). Although the β-effect is an important aspect in allowing horizontal scales and wavelengths of internal waves to shrink enough to propagate, the variability in the ocean response for similar events implicate the presence of other processes (Alford, Cronin,

et al., 2012). As internal tides, near-inertial internal waves have a horizontal scale on the order of 10-100 km (Fu, 1981) and due to their slow group velocities, they are a likely candidate to interact strongly with mesoscale features in the ocean, potentially even more likely than internal tides. This interaction can include the refraction and trapping of propagating waves (Balmforth et al., 1998; Balmforth & Young, 1999; Danioux et al., 2008; Elipot et al., 2010; P. Klein & Treguier, 1995; Kunze, 1985, 1986; Lee & Niiler, 1998; Rainville & Pinkel, 2004; Young & Ben Jelloul, 1997; Zhai et al., 2007; Zhai et al., 2005), nonlinear energy transfers (e.g. Brown & Owens, 1981; Bühler & McIntyre, 2005; P. Müller, 1976; Young & Ben Jelloul, 1997) and the mesoscale influence on the wind generation process by shifting the resonant frequency away from the local Coriolis frequency (P. Klein, Lapeyre, et al., 2004; P. Klein, Smith, et al., 2004; Kunze, 1985; Weller, 1982). Apart from the damping of the energy flux due to eddy interaction, Shakespeare and McC. Hogg (2018) diagnosed a positive transfer of energy from eddies to internal waves in a numerical model and showed that such a positive transfer of energy does not necessarily involve the generation of internal waves, but can also represent an amplification of the existing wave field. In this model, spontaneously generated internal waves by submesoscale instabilities at the surface propagate downward and are amplified in the interior by interaction with eddies. Also Cusack et al. (2020) identified energized eddies by interactions with internal waves in mooring observations. They relate those findings to a consequence of the energetic and deep-reaching shear of eddy flows in the Southern Ocean and to anisotropy in the horizontal or vertical directions of internal wave propagations. But, beside the occurrence of few smaller peaks in energy flux and in potential energy during eddy phases (as defined in section 4.1.2), which are not significantly different from the mean, I do not find any indications of mesoscale interaction with the near-inertial waves in the mooring time series. Although theoretical and modeling studies suggest that the horizontal straining component of eddy – near inertial wave interactions can extract energy from the eddy field (Rocha et al., 2018; Taylor & Straub, 2015; Xie & Vanneste, 2015). The time of the strong wind event is in a no-eddy period as defined in chapter 4.1.2.

An often-addressed aspect of near-inertial waves is their intermittency or their strong temporal variability (e.g. Fu, 1981) in comparison with internal tides or the internal wave continuum which are more constant in time and space. Their usual pronounced seasonality as well as “events” lasting for 5-20 inertial periods are consistent with the generation by storms which is a known forcing mechanism (Alford, Cronin, et al., 2012; D'Asaro et al., 1995). This agrees with the observed length of the strong wind event presented in section 5.1.2, where a diurnal pattern in the vertical velocities can also be observed in **Figure 5.5**, with a consistent length in inertial periods. Like Qi et al. (1995) and D'Asaro et al. (1995), I also find an almost instantaneous generation of inertial waves in the mixed layer followed by a likely gradual propagation into the thermocline that lasted many days after the initiation of the storm. Few other wind events around the mooring location during the deployment period were observed

by studying maps of windspeed and wind power, but only one in mid-October 2018 can be directly linked to an increase in energy flux. By investigating the wind events around the mooring location, one has to take the bathymetry and location of the wind event in relation to the location of the mooring into account. For wind events which were observed north or east from the seamount chain south of the Azores, it is likely that the near-inertial waves generated by these wind events are reflected by the seamount chain and therefore never reach the mooring location. Hence, only wind events which passed between the mooring location in the south and the seamount chain in the north-east are likely to be observed in the mooring, such as the strong wind event in October 2018. There was one other wind event which passed by north or north-west from the mooring location through the area between seamounts and mooring location but did not caused a response in the near-inertial energy flux. A likely explanation is that the induced near-inertial internal waves traveled next to the mooring and are therefore not observed. Wind events which are close the mooring location but passed south of it are also unlikely to induce a response in the near-inertial energy flux, because the near-inertial internal waves are inclined to travel south, in the direction of a lower Coriolis frequency f.

Many observations and simulations of individually moving storms, in particular hurricanes and typhoons, have been performed and characterized many aspects of the interaction between storm and ocean (e.g. Cuypers et al., 2013; D'Asaro et al., 1995; D'Asaro, 1995a, 1995b; Dohan & Davis, 2011; Firing et al., 1997; Gill, 1984; Jaimes & Shay, 2010; Jeon et al., 2019; Price, 1981, 1983; Qi et al., 1995; Sanford et al., 1987; Sanford et al., 2011; Sanford et al., 2007; Shay et al., 1992; Tsai et al., 2008; Yang & Hou, 2014; Zedler, 2009). But direct observations of near-inertial internal waves induced by strong wind events are very sparse and no study has been found that could make a clear separation between a near-inertial wave background state and a strong wind event. Nevertheless, some analogies can be drawn from earlier observations of near-inertial waves generated by storms. Yang and Hou (2014) for example found that the second baroclinic mode dominated with a variance contribution of 81 % in their observations of the typhoon Nesat. Here I do not find a similar contribution between mode 1 and mode 2 energy flux, neither in the background nor during the wind event as well as for the entire time series. A domination of mode 2 in the kinetic energy during the wind event however is observed while during the background or for the entire time series the contribution of mode 1 and mode 2 is equal. Furthermore, in contrast to the response of the energy flux, where first an increase in mode 1, followed by an increase in mode 2 can be observed during the wind event, the kinetic energy shows the opposite picture with a quicker response in mode 2 than in mode 1. Dohan and Davis (2011) observed differences between two storms of comparable magnitude in a mooring array. During the first storm they observed that the mixed layer followed a classical slab-layer response with a steady deepening during the course of the storm and little mixing of the thermocline beneath. During the second storm the mixed layer

did not deepened but shoaled while intense near-inertial waves are resonantly excited within. This seems to be a good example of internal versus external mixing (Turner, 1973), while in their first storm mixing is driven by the wind stress at the surface, which increases eddy kinetic energy by the sharpening of the transition layer thickness and the deepening of the mixed layer. In the second storm the majority of the wind forcing goes toward generating inertial oscillations. The mixing in this storm is then mostly shear driven and within the transition layer. The strong wind event in this study is likely close to the second storm event observed by Dohan and Davis (2011). As a matter of fact, I do not observe a significant increase of eddy kinetic energy during the wind event and I can identify an almost immediate generation of inertial oscillations.

Regarding the direction of the energy flux, a clear southward signal at the beginning of the strong wind event in mode 1 and later in mode 2 of the near-inertial energy flux can be identified. This agrees with the different speed of mode 1 and mode 2 internal waves, where mode 1 has a higher group speed and should arrive first at the mooring location. In theory, higher modes would arrive even later but are not resolved by the mooring. When the mode 2 energy flux arrives at the mooring location one can see a reversal in the direction of the mode 1 energy flux. Possible explanations for this are manifold (e.g. reflection by bathymetry or the generation of superinertial waves south from the mooring location) and can all reciprocally influence each other, hence an extraction of one responsible process cannot be made. Furthermore, due to the relatively short distance between the area of main wind power input and the mooring location (about 90 km between mooring location and the center of the green square in **Figure 5.4** b) one has to be generally careful if the wind event can be adequately represented by a modal decomposition.

As seen in **Figure 5.5**, the highest amplitudes in the velocity components are deepening over time after the wind event passed the mooring location. This is an indicator for downward travelling wave packets, which weakens the description of the physics by a representation of internal waves via mode separation. The modal picture is only valid when a standing wave evolved after the internal wave had been reflected at the ocean bottom or surface. Hence, it has to be tested if a mode 1 wave was already reflected at the ocean seafloor and at the surface before its measured at the mooring location. To test this the group velocities of a near-inertial mode 1 wave with a frequency of $\omega = 1.1f$ was approximated with:

$$\left(\frac{\partial\omega}{\partial k}, \frac{\partial\omega}{\partial m}\right) = \frac{km}{\omega}(\bar{N}^2 - f^2)(k^2 + m^2)^{-2}(m, -k), \qquad [5.1]$$

where the vertical group velocity is $c_{gv} = \frac{\partial\omega}{\partial m}$, and the horizontal is group velocity $c_{gh} = \frac{\partial\omega}{\partial k}$, with the vertical wavenumber *m*, the horizontal wavenumber *k*, the local Coriolis frequency *f*,

for a constant vertically averaged stratification $\overline{N}$. An ω slightly above f is a reasonable assumption to make due to the position of the wind event north of the mooring location and it is included in the initial bandpass filtering. The horizontal wavenumber k can be derived from the dispersion relation for a constant stratification $\overline{N}$:

$$\omega^2 = c_n^2 k^2 + f^2, \qquad [5.2]$$

with the eigenspeed c_n. The eigenspeed for each mode n are well approximated by:

$$c_n \approx \frac{\overline{N}H}{n\pi}. \qquad [5.3]$$

The vertical wavenumber m can then be calculated via:

$$m = \frac{\overline{N}\pi}{H}. \qquad [5.4]$$

This results in a vertical group velocity of about 0.02 m s^{-1}, and a horizontal group velocity of about 1.14 m s^{-1} for a mode 1 wave. With a water depth of about 4600 m, a mode 1 wave would need about 2.5 days to reach the seafloor before it gets reflected. The two major peaks of integrated wind power and near-inertial energy flux in **Figure 5.4** are about 4 days apart from each other. Hence, even given all the approximations made in this calculation, like the constant stratification and neglecting potential shifts of the stratification (either at the location of the wind event or caused by the wind event) or the frequency of $\omega = 1.1f$, the different Coriolis frequencies at the location of the wind power input and at the mooring location, and the uncertainties in the time between the peak of wind power input and energy flux, it seems unlikely that the strong wind event can be adequality represented in the modal picture. As a consequence, the modal decomposition might not be the correct tool to study the low mode energy flux of near-inertial waves close to their generation site. Apart from that, high modes still could be captured if the mooring would be equipped with more sensors, but higher modes usually dissipate close to the generation site and would then be missing if the observation would be further away to better display the low mode contribution. This results in a trade-off between what is desired to be observed and what can be observed by the mooring, and shows the limits of the method used in this study. Nevertheless, even if the representation via modal decomposition might not be completely adequate in the perspective of the wind event, one can still see a major effect of this event on the amplitude of the energy flux and the energy density. And also the sequence of arrival of the two modes as well as on

the direction of the energy flux, suggesting that some fundamental properties seem to be properly displayed. Furthermore, it shows how important these events are in perspective to the background state and that further investigations in this direction are necessary even if the exact numbers during the wind event have to be treated carefully.

A calculation of the consistency check r_ω as in chapter 4 for the internal tides cannot be made here because of the definition of r_ω. It is possible to evaluate the relation between kinetic and potential energy as displayed in equation [3.11] but setting $\omega = f$ is not defined and therefore no theoretical value exists. Nevertheless, to further investigate the influence of the strong wind event on the energy flux variability, I calculated the power spectra of the amplitude of modal vertical and horizontal velocities during the storm event and for the background state (**Figure 5.6**). To have a better readability, the y-axis is multiplied with the frequencies ω of the x-axis to avoid a logarithmic scale and the x-axis is scaled by the forcing frequency *f* to directly see the different harmonics of the local Coriolis frequency. The spectra show for the fundamental frequency an increase in the power density during the strong wind event in comparison to the spectra over the background period in all velocity components of the fundamental frequency in both modes. Here, the ratio between mode 1 and mode 2 remains almost the same. More prominent than the peaks in the fundamental frequency is the peak of the first harmonic of the Coriolis frequency, especially in mode 1. Due to the location of the mooring, *f* is about 23.59 h, its first harmonic is 11.80 h which is close to the M_2 frequency of 12.7 h. Because of these two frequencies being so close together, one sees a mix of both frequencies at the first harmonic. This explains also the much higher peak of the first harmonic in comparison to the fundamental frequency, because of the dominance of internal tides in this area in comparison to the wind induced near-inertial waves. There are small differences in the power spectral density estimate in the first harmonic between the background and the wind event, which can be explained with the natural variability of the amplitude in the forcing of the internal tides but also interactions between near-inertial waves and internal tides cannot be excluded and are discussed in the following. The higher power spectral density estimates in the vertical component at the second harmonic and higher can be attributed to noise.

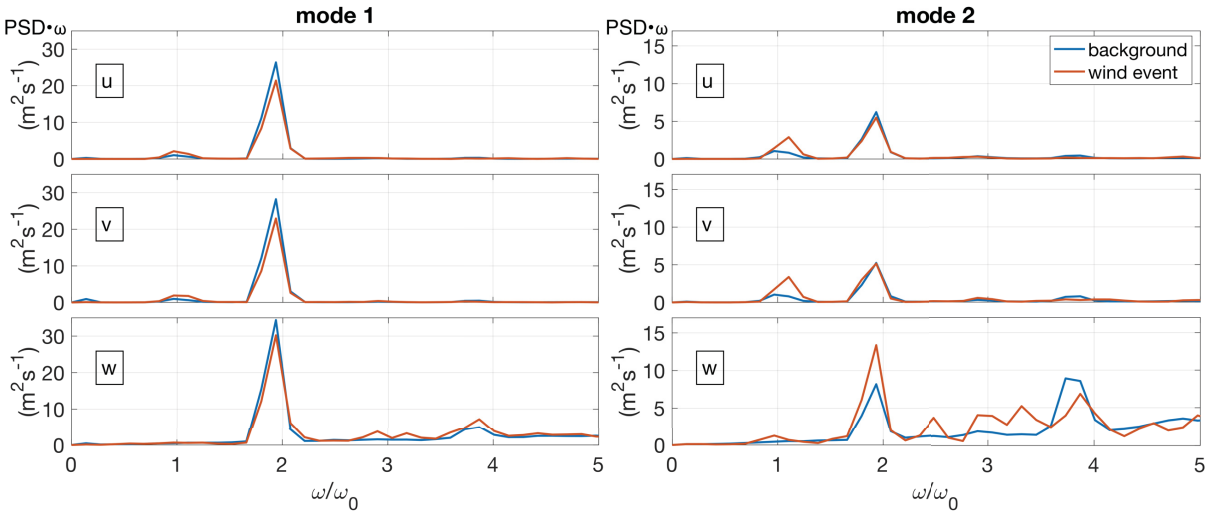

***Figure 5.6**: Power spectral density (PSD) of mooring observations after projection of horizontal (u,v) and vertical (w) velocities onto mode 1 and mode 2 shows differences between the background (blue) and during the strong wind event (red). X-axis is scaled by forcing frequency $\omega_0 = f$ and Y-axis multiplied with frequencies ω for a better readability, to avoid logarithmic scaling of the axis and to directly see the different harmonics of the local Coriolis frequency.*

The possibility that the harmonics of the near-inertial waves might interact with the internal tides can be tested by calculating the wavenumbers via the equations [5.2] to [5.4] for all frequencies of the PSD estimate in **Figure 5.6**, to check whether the conditions for resonant triad interactions are fulfilled. The conditions in wavenumber and frequency space for the interaction of a triad of internal waves (cf. chapter 1.2) are fulfilled by taking one near-inertial wave of mode 2 and two waves of mode 1, whereby it remains indifferent if the latter are first harmonics of the near-inertial internal waves or M_2 internal tides. This triad interaction has then the form of the parametric subharmonic instability (PSI) and transfers energy from a low wavenumber component to two high wavenumber components of half the frequency. PSI can cascade energy into higher modes and has been suggested to substantially shape the internal wave energy budget and potentially also turbulent mixing in several numerical studies (e.g. Furuichi et al., 2005; MacKinnon & Winters, 2005; Watanabe & Hibiya, 2002). The condition which needs to be fulfilled for the wave number and frequency triadic resonant interaction is that the parent and the sibling waves are sinusoidal in the vertical and in the horizontal. But, internal modes in a nonuniform stratified environment usually do not have a purely sinusoidal vertical structure which further complicates the analysis. Another form of interaction can be the non-linear self-interaction of internal modes in non-uniform stratified environments which results in energy being transferred to higher harmonic disturbances forced at twice the horizontal wavenumber and frequency of the parent mode (Baker & Sutherland, 2020; Sutherland, 2016; Sutherland & Jefferson, 2020). This suggests that resonant triad interactions of the low mode internal waves in the ocean may not be the only significant pathway for energy to transfer from large to small scales, and it is an ongoing debate in the scientific

community which process might be of higher relevance in the global picture (Olbers et al., 2020; Sutherland & Jefferson, 2020) Observational studies, however, reach diverging conclusions, with some supporting the importance of PSI (e.g. Nagasawa et al., 2002), while others stress the minor effect of PSI on internal wave energy levels (MacKinnon et al., 2013; Zhao & Alford, 2009).

To show the variations in the non-modal frequency spectrum **Figure 5.7** shows the Power Spectral Density (PSD) estimates for the vertical baroclinic velocities over depth and frequency in cycles per day (cpd) for the background and during the wind event. The PSD estimates were rescaled using:

$$p_s = 10log_{10}(\frac{p}{p_r}), \qquad [5.5]$$

where p_s is the power spectral density in dB, p the power spectral density in cpd and p_r represents a reference power spectral density which is the minimum of the PSD estimate. During the wind event one can identify an intensification in the near-inertial frequency band, in the internal tides and also stronger harmonics of these frequencies. The intensification in the near-inertial frequency band lies naturally in the presence of the strong wind event, while the intensification of the internal tides could be in the natural variability of the spring-neap cycle of the M_2 tide but could also be caused by the non-linear triad interactions or the non-linear self-interaction. At the time the wind event occurs, the barotropic forcing in the spring-neap cycle is declining, going towards neap tide which reinforces the argument for an increase of the energy in the M_2 frequency due non-linear interactions. But the available in-situ data does not provide further verifications in this instance, hence an amplification of the M_2 internal tide due to those non-linear interactions is speculative but cannot be excluded. Furthermore, the intensification of higher harmonics during the storm event is an indication for the self-interaction of the near-inertial waves or a possible interaction with the internal tide. The excitation of higher harmonics is not observed in the modal picture of the PSD estimates in **Figure 5.6** but they can be seen in the PSD estimates in **Figure 5.7**. This agrees with findings by Dohan and Davis (2011) who also found peaks at harmonics of inertial or tidal frequencies during the second storm event they observed.

Beside the intensification at the near-inertial frequency f also an intensification of the frequency f+M_2 can be observed during the wind event in **Figure 5.7**, especially visible in the u component. Aside from non-linear interactions where energy is transferred from the near-inertial and tidal peaks, this increase can be caused by kinematic heaving (Alford, Cronin, et al., 2012). This interaction wherein the near-inertial motions are heaved up and down by tidal displacements could be separated from the non-linear ones by a bispectral analysis. This

analysis is likely to produce potentially misleading results because its calculation is limited to a vertically two-dimensional plane, a uniform background stratification and a highly idealized incorporation of the M_2 internal tide (Chou et al., 2014). Thus, it is not included in this study.

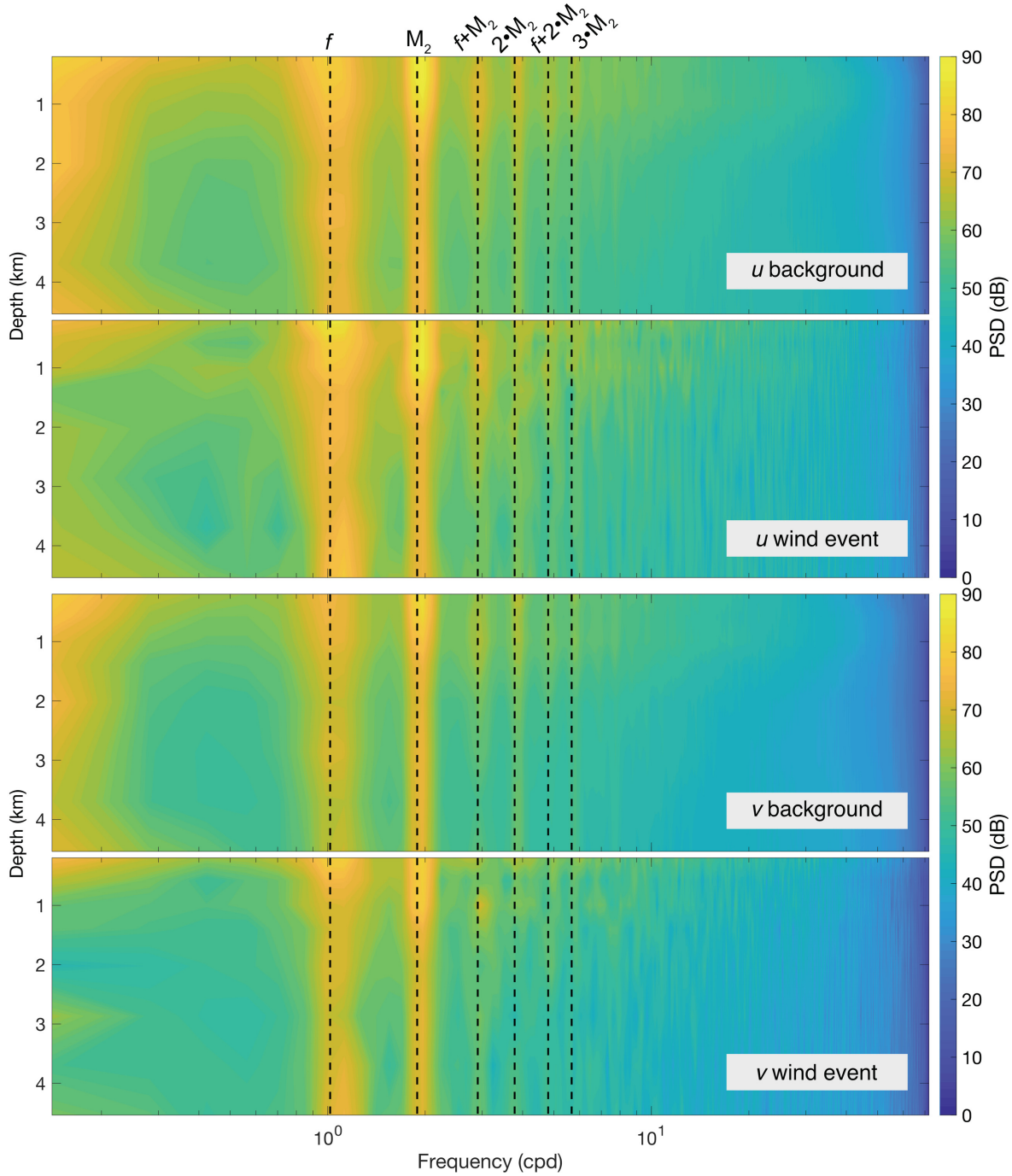

***Figure 5.7**: Power Spectral Density (PSD) estimates for the horizontal baroclinic velocities measured over depth and frequency in cycles per day (cpd) in the mooring display an intensification in the near-inertial frequency band (f) and the formation of higher harmonics during the wind event in comparison to the background. Dashed lines denote the Coriolis frequency (f) the semidiurnal internal tide (M_2), their sum ($f+M_2$), and other harmonics ($2M_2$, $f+2M_2$, $3M_2$). The PSD estimates have been scaled to decibel (dB).*

6 Comparison of the in-situ observations with model and satellite altimetry data

To quantify the capability of an OGCM and satellite altimetry to represent the in-situ observations, I compare several quantities derived from the mooring observations with the STORMTIDE2 model output, and that derived from satellite altimetry. This comparison is motivated by the question of how good an OGCM such as STORMTIDE2, that is not specifically tuned to mimic the measurements, is able to represent the characteristics of the energy flux in strong generation regions of internal tides. The comparison focuses on the energy flux of the internal waves, since this quantity is relatively easy to examine for this kind of models. Moreover, it is an important benchmark for models since its divergence identifies sources and sinks of energy, while OGCM's are usually not energetically consistent. The comparison of the M_2 coherent internal tide from the in-situ measurements with the satellite altimetry is motived by the separation between true dissipation and a loss of coherence. Because when internal tides propagate through the ocean, currents and variations in the stratification can modify their phase and group speed and make them incoherent. This can result in a fictitious energy loss of the internal tide along the propagation path when detected by satellite altimetry. Usually, a point-wise comparison of measurements with a model or other large dataset can be problematic for various reasons, for example because of spatial and temporal averaging or interference patterns of multiple waves (Terker et al., 2014).

In this chapter I first look at the comparability between the in-situ observations and the STORMTIDE2 model in section 6.1, followed by a comparison of STORMTIDE2's internal tides with the results from the in-situ measurements in section 6.2. In section 6.3 I compare the near-inertial waves from STORMTIDE2 with the in-situ measurements. The chapter is completed by a comparison of the M_2 coherent internal tide energy flux derived from satellite altimetry with the in-situ measurements in section 6.4. A comprehensive list of all mean energy fluxes is given in the beginning of the individual sections.

6.1 Comparability of the in-situ observations with STORMTIDE2

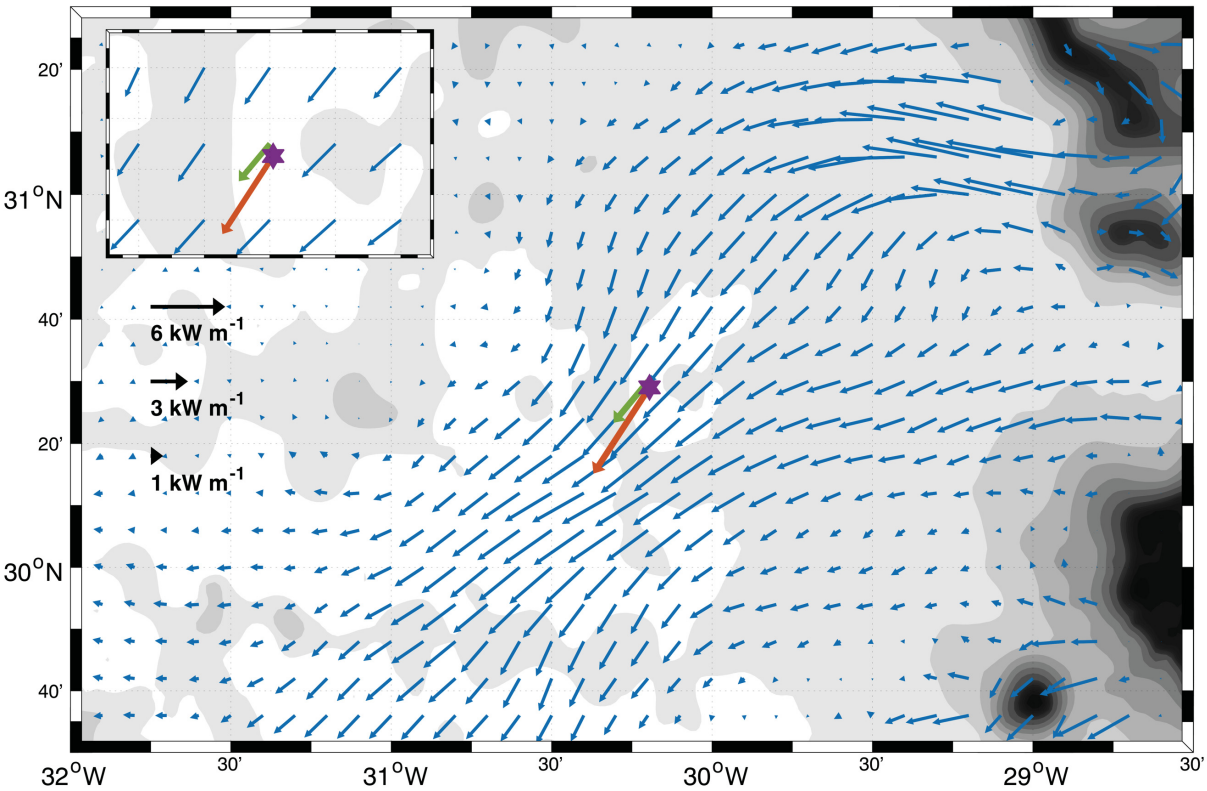

***Figure 6.1**: Position of the mooring in relation to the internal tide energy flux calculated from STORMTIDE2. Purple star: mooring location; red arrow: semidiurnal energy flux from mooring time series; green arrow: semidiurnal energy flux from STORMTIDE2 at the grid point closest to the mooring location; blue arrows: semidiurnal energy flux from STORMTIDE2; reference arrows for the main map at the left side. Inset upper left corner shows a zoom focused on the mooring position. Background: grey shading of bathymetry for every 100 m in the upper 1000 m and every 500 m for the remainder of the water depth.*

To demonstrate that a point-wise comparison of the STORMTIDE2 dataset with the in-situ measurements are, with some limitations justified, I display in **Figure 6.1** the location of the mooring in context of the net semidiurnal energy flux of the internal tides calculated from the four months of available STORMTIDE2 model output. The mooring location is marked with a purple star, and the energy flux of the model grid point closest to the mooring location is colored in green. The net semidiurnal energy flux from STORMTIDE2 is varying in direction and magnitude in the wider region around the mooring location, with a distinct tide beam in southwest direction. Closer to the mooring location in the tide beam, however, the model

shows a more homogenous picture (**Figure 6.1**, inset). This homogeneity is likely caused by the interference pattern of single waves forming the beam like structure, and the energy flux seem to vary little in close proximity to the mooring. Given the location of the mooring inside the tide beam in the STORMTIDE2 model, a point-wise comparison of the mooring with the closest grid point in STORMTIDE2 seems a viable comparison to make.

Looking at the net near-inertial energy flux derived from the four months of available model data from STORMTIDE2 in **Figure 6.2**, one can see a more diverse picture than for the internal tides. Also in this figure the mooring location is marked with a purple star, and the energy flux of the model grid point closest to the mooring location is colored in green. The majority of the near-inertial energy flux in STORMTIDE2 is, as expected, southward in direction of lower *f*. But near to the seamount chain, north-west of the mooring location, the amplitude of the near-inertial energy fluxes are generally higher and in northward direction. This northward pointing energy flux is likely caused by reflections of the steep topography of the seamounts.

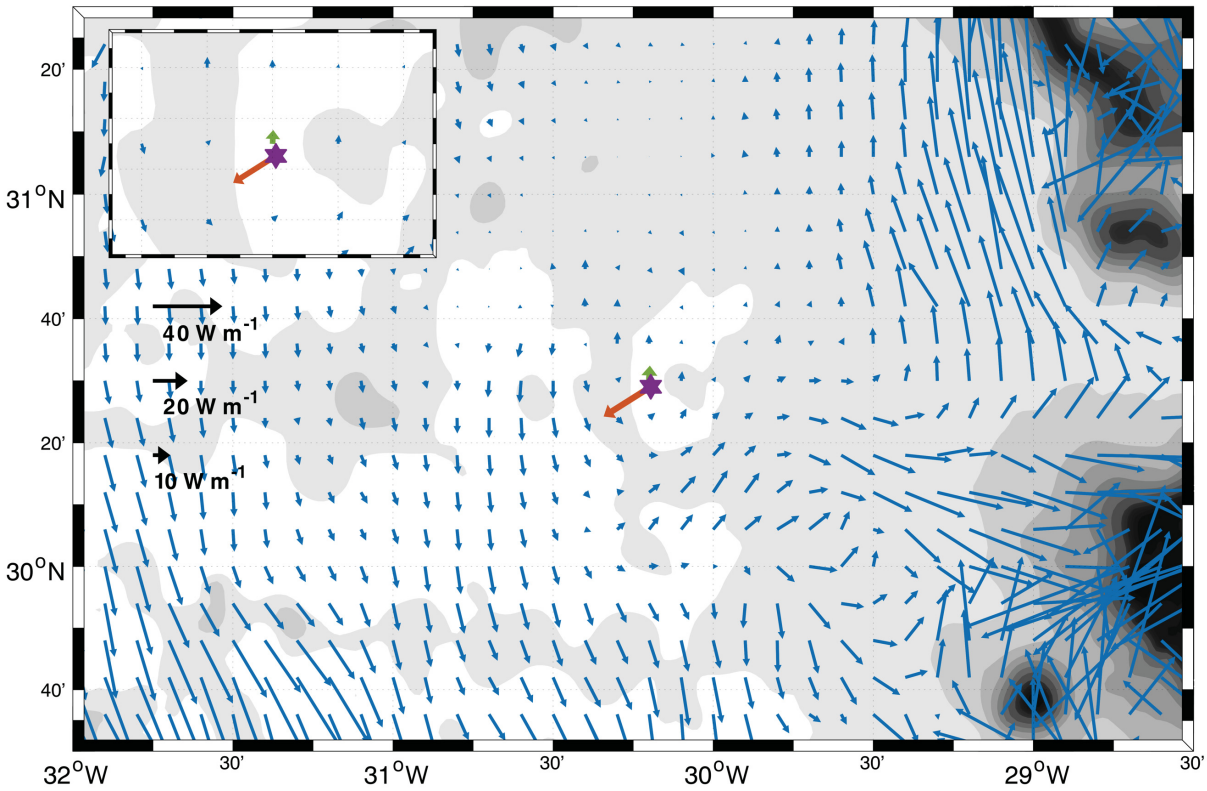

***Figure 6.2**: Position of the mooring in relation to the near-inertial internal wave net energy flux calculated from STORMTIDE2. Purple star: mooring location; red arrow: net near-inertial energy flux from the mooring time series; green arrow: near-inertial energy flux from STORMTIDE2 at the grid point closest to the mooring location; blue arrows: net near-inertial energy flux from STORMTIDE2; reference arrows for the main map at the left side. Inset upper left corner shows a zoom focused on the mooring position. Background: grey shading of bathymetry for every 100 m in the upper 1000 m and every 500 m for the remainder of the water depth.*

The near-inertial energy flux from STORMTIDE2 is varying in direction and magnitude in the entire study region south of the Azores which hampers a point-wise comparison of the model with the in-situ measurements. Furthermore, when comparing the near-inertial energy flux from the in-situ measurements with STORMTIDE2, one has to consider the different times of which the data was generated. The strong temporal and spatial variability of near-inertial waves due to the generation by the wind has to be considered in contrast to the relatively constant forcing of the tides with its spring-neap cycle and its formation of a tide beam. Because of the different times the data was generated (2012 for STORMTIDE2, 2017 – 2019 for the in-situ measurements) and the different wind power input into the mixed layer caused by different winds at these times, the comparable parameters are reduced.

Another hint regarding the comparability of the in-situ measurements with STORMTIDE2 can be given by estimates of the power density spectra of the horizontal baroclinic velocities. **Figure 6.3** shows these estimates which are rescaled to decibel according to equation [5.5], for the mooring, and the closest grid point to the mooring of the STORMTIDE2 dataset. Both datasets show a surface intensification at the Coriolis frequency and of the semidiurnal tide with the occurrence of harmonics of these frequencies. In the Coriolis frequency band *f*, one can identify a similar surface intensification between the two datasets. But in contrast to the in-situ measurements, where higher values throughout the entire water column can be observed, in STORMTIDE2 the PSD estimates drop sharply in a depth of about 300 m. This indicates that the surface energy in STORMTIDE2 is not able to propagate into the deep ocean. The semidiurnal tide shows a similar overall structure with a surface intensification. But the surface intensification of the mooring observations is stronger in comparison to STORMTIDE2. Generally, the PSD estimates of the mooring for the internal tides and near-inertial waves remains relatively constant with depth, although the bandwidth decreases because the stratification weakens with depth. The PSD estimates further elucidate that a direct point-wise comparison of the M_2 internal tide should be justified, but it is hampered for the near-inertial component by a likely incorrect representation in the model.

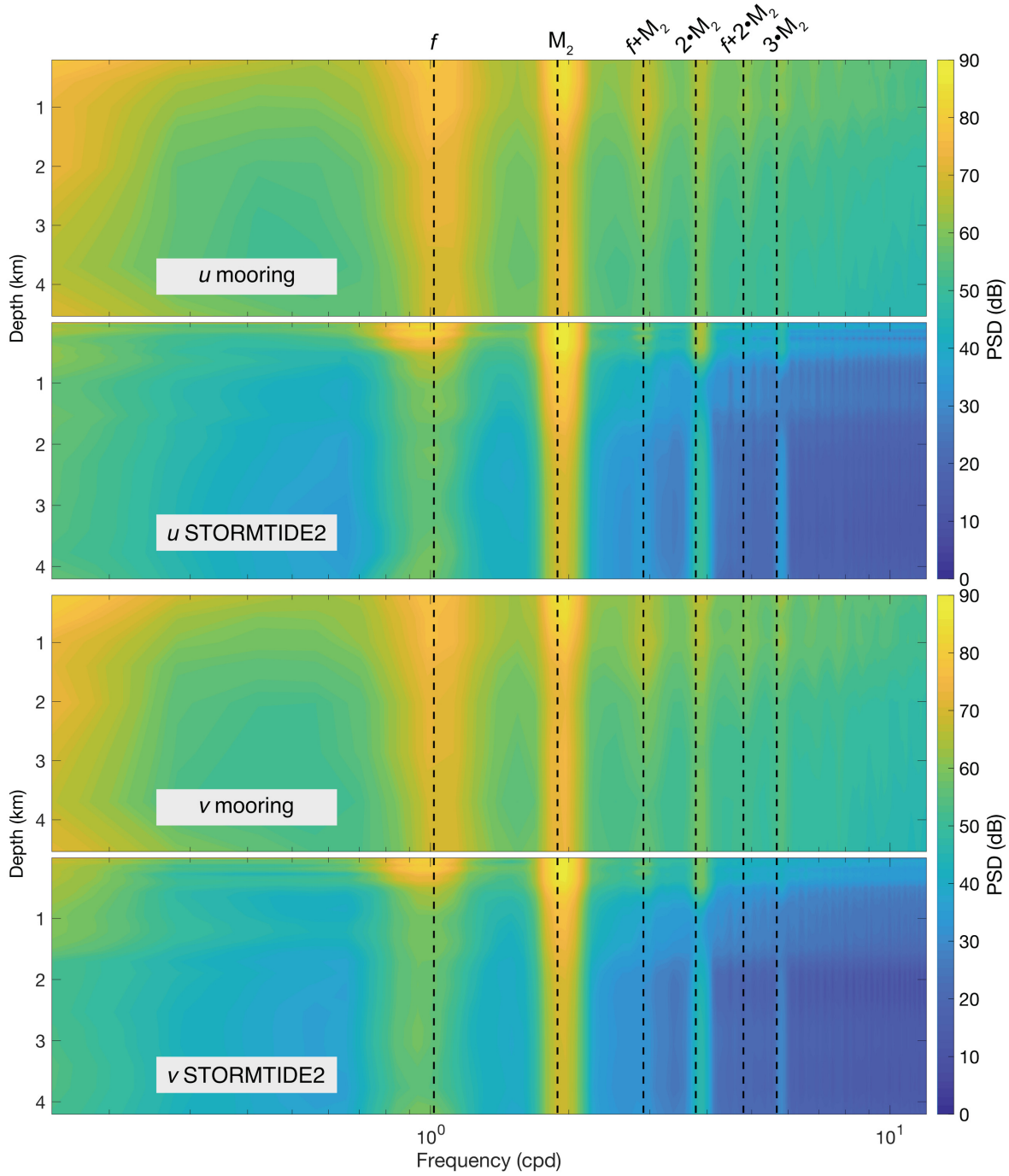

***Figure 6.3**: Power Spectral Density (PSD) estimates for the horizontal baroclinic velocities measured over depth and frequency in cycles per day (cpd), shows generally higher values for the mooring in compare with the STORMTIDE2 model. Dashed lines denote the Coriolis frequency (f) the semidiurnal internal tide (M_2), their sum ($f+M_2$), and other harmonics ($2M_2$, $f+2M_2$, $3M_2$). The PSD estimates have been scaled to decibel (dB).*

6.2 Comparison of the internal tide with STORMTIDE2

The mean energy fluxes from STORMTIDE2 in the semidiurnal band, as well as for its M_2+S_2 coherent and M_2 coherent parts are shown in **Table 6.1**, whereas **Figure 6.4** shows the time series of the semidiurnal energy flux, the direction of mode 1 and mode 2 as well as the ratio between first and second mode for all available months of the STORMTIDE2 dataset. One can see that there are few differences between the individual model months in these parameters, although they are at different times in the spring-neap cycle.

	Semidiurnal flux (kW m^{-1})			M_2+S_2 Coherent flux (kW m^{-1})			M_2 coherent flux (kW m^{-1})		
	Mode 1	Mode 2	**total**	Mode 1	Mode 2	**total**	Mode 1	Mode 2	**total**
STORMTIDE2	3.97 ±0.23	0.41 ±0.03	**4.39** ±0.24	3.76 ±0.05	0.40 ±0.01	**4.16** ±0.05	3.51 ±0.04	0.36 ±0.01	**3.87** ±0.04
	[0.06]	[0.07]	**[0.05]**						

***Table 6.1**: Mean energy flux of STORMTIDE2 in the semidiurnal band, the M_2+S_2 coherent and M2 coherent part. Distortion parameter d in square brackets for the semidiurnal energy flux.*

The energy fluxes from STORMTIDE2, as well as the mooring data, show a strong spring-neap variability clearly dominated by mode 1. The time mean for the STORMTIDE2 semidiurnal energy flux for the sum of the first and second mode is 4.39±0.24 kW m^{-1} (3.97±0.23 kW m^{-1} for mode 1, 0.41±0.03 kW m^{-1} for mode 2), with peaks up to 9.34 kW m^{-1}. This corresponds to an underestimation of the energy flux by the model of a factor of about 2 in comparison to the mean amplitude of the semidiurnal part of the mooring time series. In the M_2 coherent part, the underestimation of STORMTIDE2 compared to the mooring time series is a factor of about 1.9, while 95 % of the sum of the energy flux in mode 1 and mode 2 (95 % mode 1, 98 % mode 2) in the STORMTIDE2 model is coherent (**Table 6.1**). Hence, model and in-situ observations agree on the amount of incoherent energy flux for the first mode but differ on how much energy is in the incoherent part of the second mode. The higher coherence in the model compared to the in-situ measurements possibly result from a weaker background variability, which lead to fewer interactions with mesoscale motions, especially in mode 2 which has a higher susceptibility for disturbances than mode 1. Because of its resolution, STORMTIDE2 is also not able to resolve wave-wave interactions, representing another missing aspect that leads to an increase in incoherent energy flux. The significantly weaker energy flux

in the STORMTIDE2 model (in the total semidiurnal band, as well as in the M_2 coherent case) in comparison to the energy flux from the in-situ measurements is most likely caused by an unrealistically high (numerical) damping in the model (Köhler et al., 2019; M. Müller et al., 2012). Another possible explanation for the lower energy flux in STORMTIDE2 could be a not sufficient barotropic to baroclinic energy conversion rate at the seamount chain which is generating the observed tide beam. But this aspect is likely less prevalent regarding the sufficient barotropic velocities provided by STORMTIDE2, as discussed in Section 2.2. The fraction of the first mode in the semidiurnal energy flux in STORMTIDE2 is 90±1 %, and does not change for the M_2 coherent part of the energy flux which is 90.7±0.3 %. In this case model and in-situ observations agree on the fraction of mode 1 in the total semidiurnal part, but differ on this ratio in the M_2 coherent part, where the fraction of mode 1 increases. Furthermore, also in the STORMTIDE2 time series, one can identify a clear time lag between the peaks in energy flux of mode 1 and mode 2 similar to the in-situ measurements, representing the different travel times of mode 1 and mode 2 waves generated at the seamount chain south of the Azores.

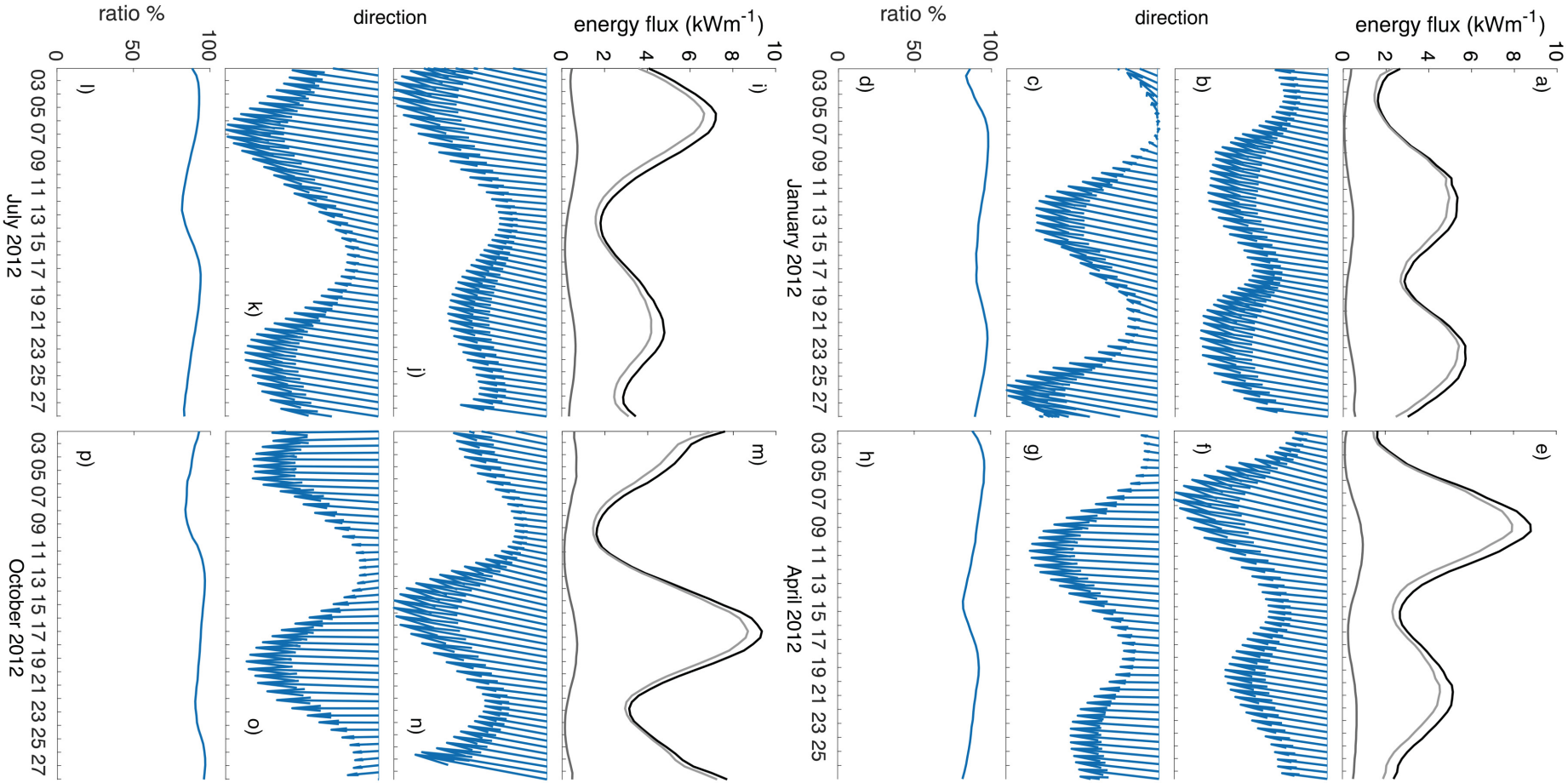

***Figure 6.4**: Time series of semidiurnal energy flux from the STORMTIDE2 model at the closest grid point to the mooring location show few differences between each individual model month. a), e), i), m) black: Sum of mode 1 and mode 2 of near-inertial energy flux from the mooring observations. Light grey and dark grey are the first and second mode of the near-inertial energy fluxes respectively. b), f), j) n), Direction of mode 1 near-inertial energy flux. c), g), k), o) Direction of mode 2 near-inertial energy flux. d), h), l), p) ratio between first and second mode of energy flux.*

Like the in-situ measurements, the direction of the STORMTIDE2 energy flux does not vary much in time and is steadily pointing away from its generation site. This is true not only for the first, but also for the second mode, whereby in contrast to the in-situ observations no northward energy flux can be detected in the STORMTIDE2 time series. Unlike the temporal variability in the energy flux magnitude, it seems that STORMTIDE2 is unable to accurately reproduce the temporal variability of the heading of the tidal energy fluxes. This implies that while the magnitude of the energy flux is highly correlated with the forcing, the heading of the energy flux is more sensitive to other dynamics that are unresolved in the STORMTIDE2 model such as interactions with other propagating internal waves. Similar observations have been made by Savage et al. (2020) who compared a month long mooring observation of energy fluxes in a tide beam with a semi-idealized internal tide model (the Coupled-mode Shallow Water Model, CSW). The mean direction of the amplitude of the semidiurnal energy flux in STORMTIDE2 is 230°±1° for mode 1 and 224°±7° for mode 2 and can be seen in **Figure 6.5** in relation to the mean amplitude of energy flux and its mean direction from the in-situ observations. This puts the mean direction of mode 1 of the energy flux in the semidiurnal component from STORMTIDE2 in a good agreement with the mode 1 mean directions from the in-situ measurements, and to a lesser degree also in mode 2.

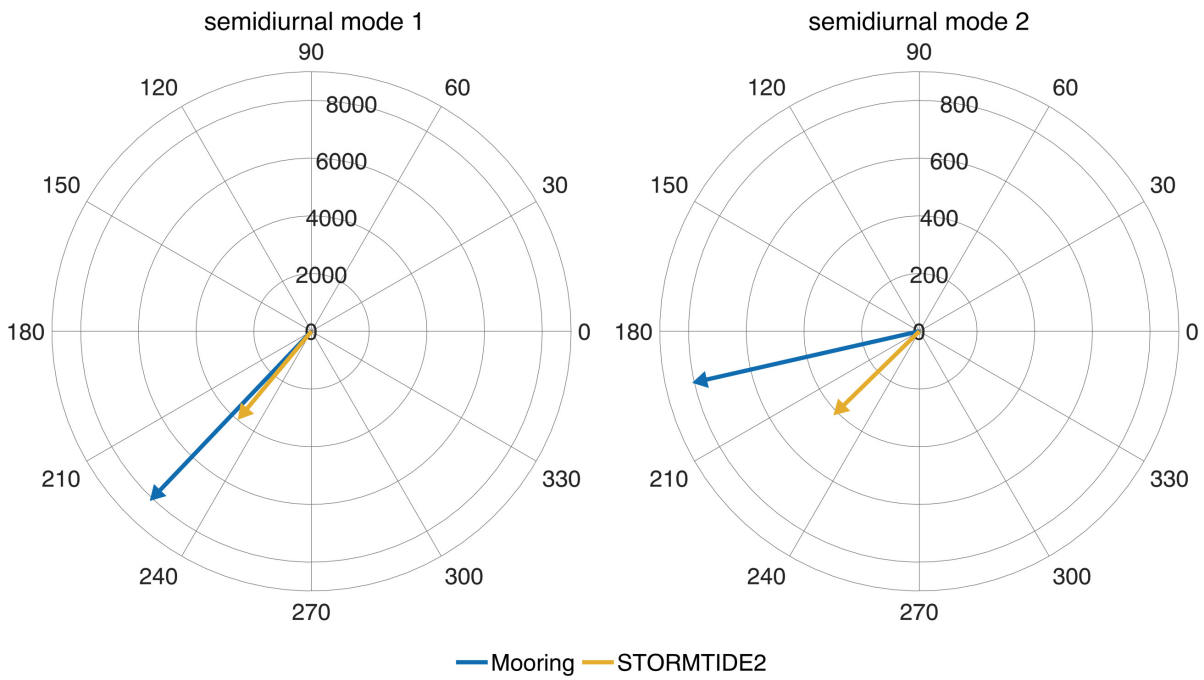

***Figure 6.5**: Mean amplitude and direction of the semidiurnal energy flux of the mooring time series (blue), STORMTIDE2 (yellow) for the first and second mode.*

The mean potential energy from STORMTIDE2 in the semidiurnal band is 1.67±0.04 kJ m^{-2} for the sum of mode 1 and mode 2 (1.31±0.04 kJ m^{-2} for mode 1, 0.37±0.01 kJ m^{-2} for mode 2).

The mean kinetic energy from STORMTIDE2 in the semidiurnal band is 0.68±0.01 kJ m^{-2} for the sum of mode 1 and mode 2 (0.57±0.01 kJ m^{-2} for mode 1 and 0.11±0.004 kJ m^{-2} for mode 2). As in chapter 4, I calculated r_ω as ratio between the kinetic and potential energy which can be used as a consistency check, with this ratio intrinsic frequencies can be detected. The r_ω time series shown in **Figure 6.6** displays constantly values below the theoretical value of about 1.81. The mean r_ω over all available model months is 0.42±0.01. Hence, the ratio of kinetic to potential energy is reversed, which arises the question if the kinetic energy is underrepresented or the potential energy is overrepresented (or a mix of both) in STORMTIDE2. Comparing the stratification (**Figure 2.3**) and the displacements used in the calculation process reveals a good representation by STORMTIDE2 with the in-situ observations which indicates a correct representation of potential energy. By comparing the M_2 filtered horizontal baroclinic velocities however, model and in-situ observations show a discrepancy. These velocities are about half as strong as in the in-situ observations and since these values enter quadratically into the equation for kinetic energy it means that a factor of about 4 would be needed to reverse the ratio between kinetic and potential energy. For now, it remains unclear why the M_2 filtered horizontal baroclinic velocities are almost half as strong in STORMTIDE2 as in the in-situ observations. One possible explanation might be a too weak conversion rate from barotropic to baroclinic energy of STORMTIDE2.

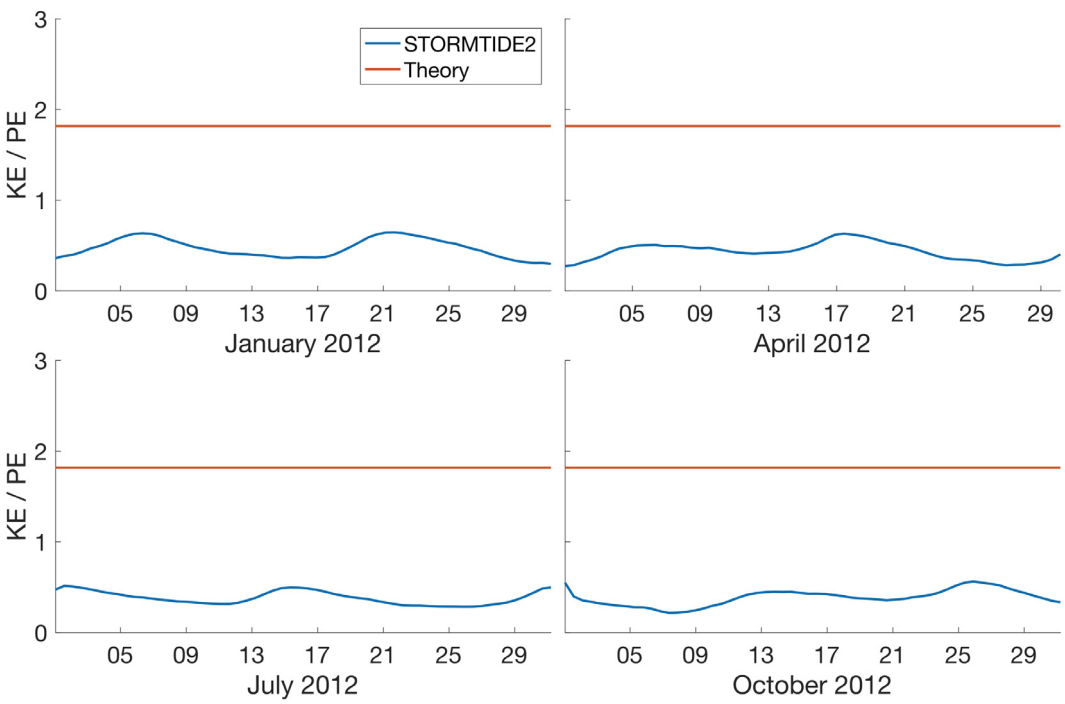

***Figure 6.6**: The Ratio r_ω of kinetic energy (KE) to potential energy (PE) from the STORTMIDE2 model (blue) shows constantly lower values during all model month than the theoretical value (red).*

The STORMTIDE2 model shows only a very weak mesoscale variability compared to the measurements in the region south of the Azores. I calculated the eddy kinetic energy (EKE) in the available model output, but could not identify a clear eddy signal. Furthermore, the time series of energy flux of STORMTIDE2 does not show any signs of possible interactions like a significant drop of energy flux not related to the variability in the spring-neap cycle, a higher directional variability, a change in the ratio between mode 1 and mode 2, a loss in coherence or peaks in the r_ω time series. Hence, it is not possible to compare the observed eddy – internal tide interactions with a similar situation in the model in this region. While a direct comparison of the in-situ observations with the STORMTIDE2 model is not possible during the eddy period, a comparison during the no-eddy period of the observations with the 'background' state in the model is possible. However, by doing so the difference between the semidiurnal energy fluxes between model and in-situ observations is not reduced, but rather increased to a factor of about 2.2. Taking only the M_2 coherent part during the no-eddy period of the mooring with the STORMTIDE2 average results in an underestimation of a factor of 2.1. Nevertheless, the distortion parameter in STORMTIDE2 agrees nicely with the distortion parameter of the in-situ observations during the no-eddy period with a value of 0.05, indicating similar disturbances in the background state.

Generally, the internal tide energy flux from the in-situ measurements is adequately represented in its direction and ratio between mode 1 and mode 2 despite the underestimation of the total energy flux by about a factor of 2. Regarding the damping of the energy flux and the associated loss in coherence with the occurrence of mesoscale eddies in the mooring time series, it is unambiguous how important a good realization of the interaction of mesoscale eddies with internal tides is.

6.3 Comparison of the near-inertial waves with STORMTIDE2

As stated above, a comparison of the near-inertial waves from STORMTIDE2 with the in-situ observations is difficult regarding the different times the data are representing. While the amplitude of the energy flux and the fraction between mode 1 and mode 2 can still be reasonably well compared between model and in-situ observations, the direction of the energy flux depends strongly on the location where the internal waves are generated. This location can be substantially different in each of the two datasets. Hence, the main reason to present the time series of the direction is not about in which direction the energy flux is pointing at but rather how strong it varies over time. Nevertheless, to be consistent with the comparison of the internal tides between the in-situ measurements and the STORMTIDE2

model, I present the values of the closest grid point of the STORMTIDE2 model to the mooring location.

The mean energy fluxes from STORTMIDE2 in the near-inertial band, as well as its mean potential and kinetic energies are shown in **Table 6.2**, whereas **Figure 6.7** shows the time series of the near-inertial energy flux, the direction of mode 1 and mode 2 as well as the ratio between first and second mode for all available months of the STORMTIDE2 dataset. One can see that there are distinct differences between the individual model months in the above-mentioned parameters, likely associated with the different wind forcing at each individual month. In the beginning of April and July 2012, two peaks in the energy flux time series can be observed with a distinct southward and northward direction in mode 1, respectively.

	Near-inertial flux (W m^{-1})			Kinetic energy (J m^{-2})			Potential energy (J m^{-2})		
	Mode 1	Mode 2	**total**	Mode 1	Mode 2	**total**	Mode 1	Mode 2	**total**
STORMTIDE2	19 ±5	9 ±1	**28** ±5	27.4 ±1.5	43.8 ±1.7	**71.1** ±2.6	8.4 ± 1.8	2.9 ±0.6	**11.3** ±1.9

***Table 6.2**: Mean energy flux of STORMTIDE2 in the near-inertial band, and its corresponding kinetic and potential energy.*

The mean energy flux of the closest grid point to the in-situ measurements as the sum of mode 1 and mode 2 is 28±5 W m^{-1} (19±5 W m^{-1} for mode 1, 9±1 W m^{-1} for mode 2, **Table 6.2**). The highest peak in this time series is 0.15 kW m^{-1} in July. This peak is about 5 times higher than the mean of all four months of the model. The fraction of the first mode in relation to the total energy flux is 57±5 % and varies between 0.4 % and 97 %, similar to the in-situ observations. In contrast to the in-situ measurements, the amplitude of the energy flux in STORMTIDE2 is slightly dominated by mode 1 in comparison to mode 2, whereas the main temporal variability in the near-inertial energy flux lies in mode 1 with a higher standard deviation than mode 2. The mean potential energy from STORMTIDE2 in the near-inertial band is 11.3±1.9 J m^{-2} for the sum of mode 1 and mode 2 (8.4±1.8 m^{-2} for mode 1, 2.9±0.6 J m^{-2} for mode 2), and the mean kinetic energy from STORMTIDE2 in the near-inertial band is 71.1 ±2.6 J m^{-2} for the sum of mode 1 and mode 2 (27.4±1.5 J m^{-2} for mode 1 and 43.8±1.7 J m^{-2} for mode 2). This reveals that in the STORMTIDE2 model the kinetic energy is about 6.3 times higher than the potential energy, whereas in the in-situ observations this ratio is about 11.25. As in the in-situ observations, also STORMTIDE2 has more kinetic energy in mode 2 than in mode 1, but in contrast to the in-situ observations we do not see also a higher potential energy in the second mode. In STORMTIDE2 mode 1 contains most of the potential energy.

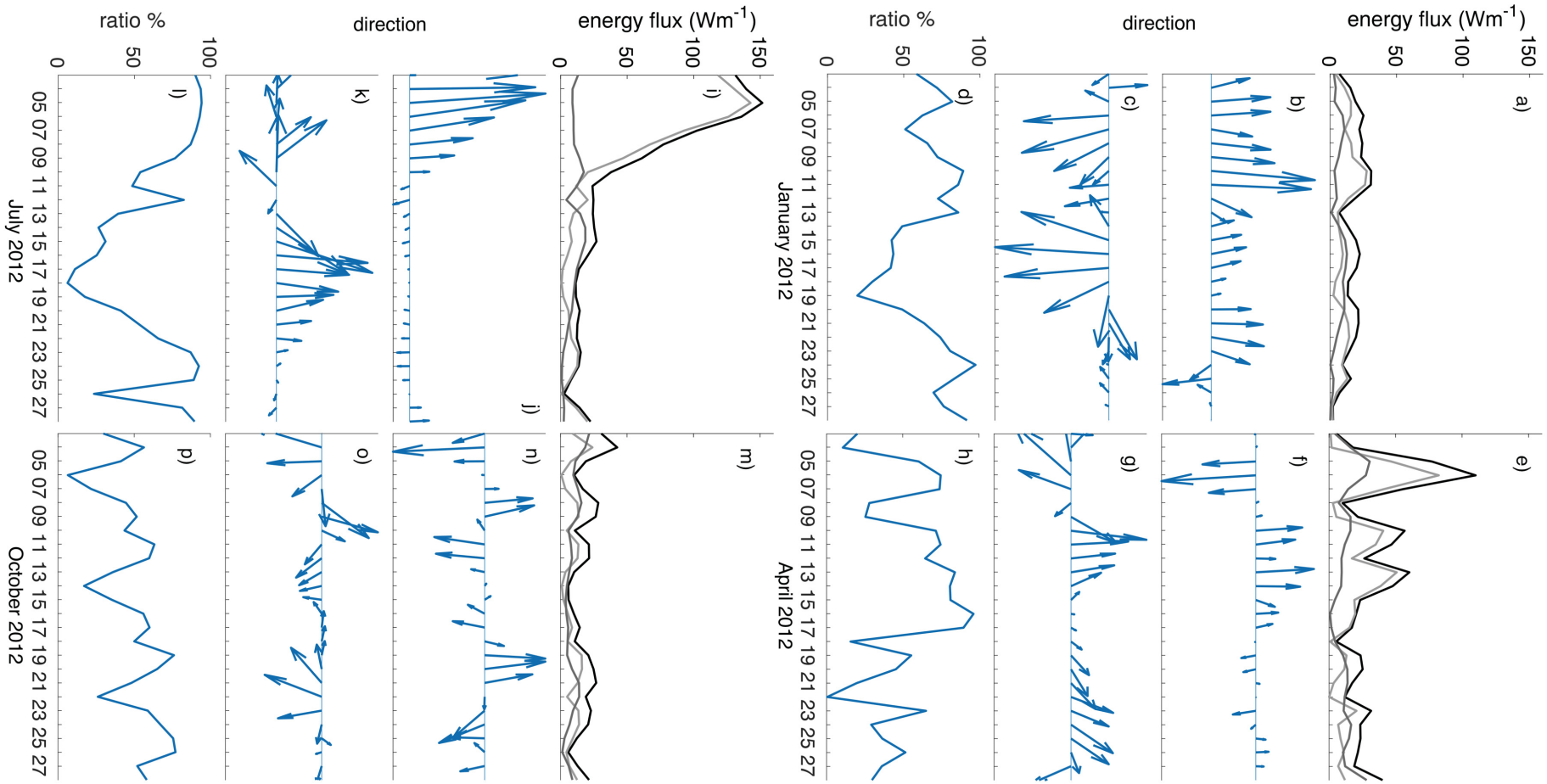

Figure 6.7*: Time series of near-inertial energy flux from the STORMTIDE2 model at the closest grid point to the mooring location. a), i), e), m) black: Sum of mode 1 and mode 2 of near-inertial energy flux from the mooring observations. Light grey and dark grey are the first and second mode of the near-inertial energy fluxes respectively. b), f), j), n) Direction of mode 1 near-inertial energy flux. c), g), k) o) Direction of mode 2 near-inertial energy flux. d), h) l), p) ratio between first and second mode of energy flux.*

Even if the near-inertial energy flux is not steady and varies in direction during all available model months in both modes, and its direction is strongly depended on the location of the generation by the wind, the mean direction of the energy flux in STORMTIDE2 is relatively similar to that of the in-situ observations as shown in **Figure 6.8**. The mean direction for STORMTIDE2 of mode 1 near-inertial energy flux is 157°±13°, whereas the mean direction of mode 2 is 181°±9°.

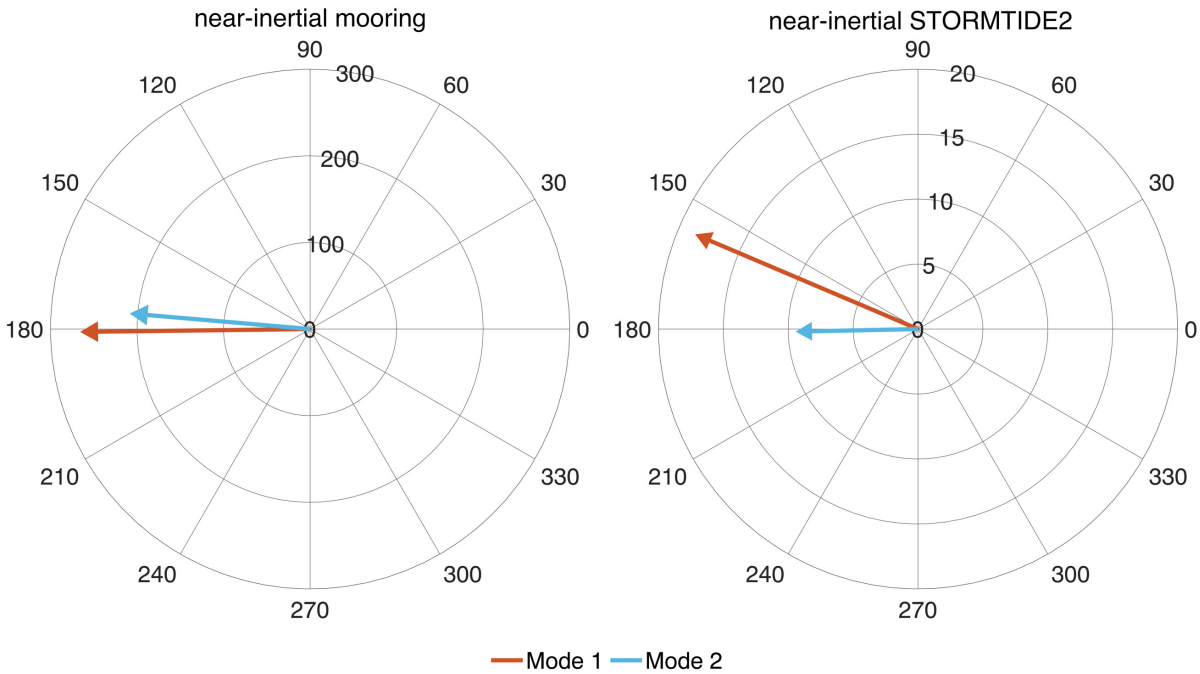

***Figure 6.8**: Mean amplitude and direction of the near-inertial energy flux of the mooring time series and STORMTIDE2 for the first (red) and second (blue) mode.*

The mean near-inertial energy flux from STORMTIDE2 as the sum of mode 1 and mode 2 underestimates the near-inertial energy flux from the in-situ observations by more than one order of magnitude, more precisely by a factor of about 17. Not only the energy flux in STORMTIDE2 is strongly underestimated, also its potential and kinetic energy are about an order of magnitude lower. The reason for this stronger underestimation for the near-inertial waves than for the internal tides is likely a combination of the earlier mentioned unrealistically high (numerical) damping in the model (Köhler et al., 2019; M. Müller et al., 2012) and a not sufficient temporal resolution of the wind forcing in STORMTIDE2 (Jiang et al., 2005; Rimac et al., 2013). It has been shown by Rimac et al. (2013), that models can be very sensitive to the temporal and spatial resolution of the input wind dataset. They presented an increase of wind generated power input to near-inertial motions by a factor of about 3 by using an hourly wind input with 0.35° resolution in compare to a six hourly wind input with a 1.875° resolution in a global eddy-permitting OGCM. They further suggest that high-frequency temporal variations in the wind stress field are more efficient in generating near-inertial wave energy than small-

scale spatial variations in the wind stress field. **Figure 6.3** is further suggesting that around the Coriolis frequency f only few energy is leaving the upper water column. This leads to less waves that are emanated from its generation site. This can imply that near-inertial waves, which are generated in the STORMTIDE2 model do not travel far enough, potentially due to the resolution of the wind forcing or by the damping in the model. Thus, only waves generated in close proximity to the here shown grid point are present.

The two peaks in the beginning of April 2012 and July 2012 with their distinct directions are suggesting wind events as a cause, as for the peaks in the near-inertial waves in the in-situ measurements in chapter 5. To check whether there are wind events present at these times, I examined the same wind dataset used in chapter 5 for verification. Unfortunately, such wind-events could not be identified. Furthermore, the observed peaks generated by the strong wind event in the in-situ observations are about 13.5 times higher than the mean of the entire time series in contrast to the about 5 times higher in the STORMTIDE2 model. Together with the usual strong speeds of which these events are usually passing over single locations in relation to the temporal resolution of the wind dataset used in STORMTIDE2, their overall presence in the model is generally questionable. Therefore, a comparison of the strong-wind event in the in-situ observations with a similar situation in the STORMTIDE2 model cannot be made.

Generally, the amplitude of the near-inertial energy flux, as well as the amplitude of kinetic and potential energy from the in-situ measurements seem to be worse represented in the STORMTIDE2 dataset than its internal tides. Despite that the ratio of mode 1 to mode 2 of the energy flux as well as the mean directions of the energy flux and its high variability are well represented by the model, and that like the in-situ observations mode 2 contains more kinetic energy than mode 1, the magnitude of the energy flux and of the potential and kinetic energy are strongly underestimated in the model.

6.4 Comparison of the M_2 coherent internal tide with satellite altimetry

From satellite altimetry data it is only possible to extract the coherent part of the internal tide energy flux (Zhao et al., 2016), so the results from the altimetry can only be compared to the M_2 coherent portion of the in-situ measurements and of STORMTIDE2. Furthermore, the satellite altimetry data cannot display any particular events regarding its spatial and temporal averaging, hence a comparison of the impact of specific eddy events on the M_2 coherent energy flux from the satellite altimetry dataset cannot be made. Nevertheless, because of the temporal and spatial averaging one can assume that the impact of eddies in the study region are considered. I therefore compare the M_2 coherent part of the in-situ measurements over

the entire deployment period of the mooring with the data from satellite altimetry. Regarding the comparability of a point-wise comparison between a single mooring and the large dataset as satellite altimetry, due to its position inside the tide beam, such comparison is in a similar way justified as for the STORMTIDE2 dataset.

	Semidiurnal flux (kW m^{-1})			M_2+S_2 Coherent flux (kW m^{-1})			M_2 coherent flux (kW m^{-1})		
	Mode 1	Mode 2	**total**	Mode 1	Mode 2	**total**	Mode 1	Mode 2	**total**
Satellite altimetry	/	/	/	/	/	/	1.76	0.08	**1.84**

***Table 6.3**: Estimates of internal tide energy flux derived from satellite can only be extracted for its coherent component.*

Mean amplitudes of energy fluxes calculated from satellite altimetry show 1.84 kW m^{-1} as the sum for the first and second mode (1.76 kW m^{-1} for mode 1, 0.08 kW m^{-1} for mode 2, **Table 6.3**). In compare, the M_2 coherent part of the energy flux from in-situ measurements for the sum of mode 1 and mode 2 is 7.24±0.02 kW m^{-1} (6.96±0.02 kW m^{-1} for mode 1, 0.28±0.01 kW m^{-1} for mode 2, **Table 4.1**), and for STORMTIDE2 3.87±0.04 kW m^{-1} (3.51±0.04 kW m^{-1} for mode 1, 0.36±0.01 kW m^{-1} for mode 2, **Table 6.1**). This results in an underestimate of the mean amplitude of energy flux from satellite altimetry of a factor of about 3.9 and 2.1 in compare to the in-situ measurements and STORMTIDE2 respectively. For the energy flux derived from satellite altimetry, the fraction of the first mode is 90.7±0.3 %, and for the in-situ observations it is 96.1±0.2 %.

The mean direction and the mean amplitude of the M_2 coherent energy flux for mode 1 and mode 2 are shown in **Figure 6.9**. The mean direction of the M_2 coherent energy flux is 238.4°±0.3° for the mooring, 230.5°±0.3° for STORMTIDE2 and 244.5° for the satellite altimetry in mode 1. For mode 2 it is 218.3°±0.2° for the mooring, 243.4°±4.1° for STORMTIDE2 and 273.7° for the satellite altimetry. The mean direction of the M_2 coherent energy flux from satellite altimetry is in a good agreement with the in-situ measurements and the results from STORMTIDE2 in mode 1. But they are further apart in mode 2, with STORMTIDE2 being in between the in-situ measurements and the energy flux from satellite altimetry.

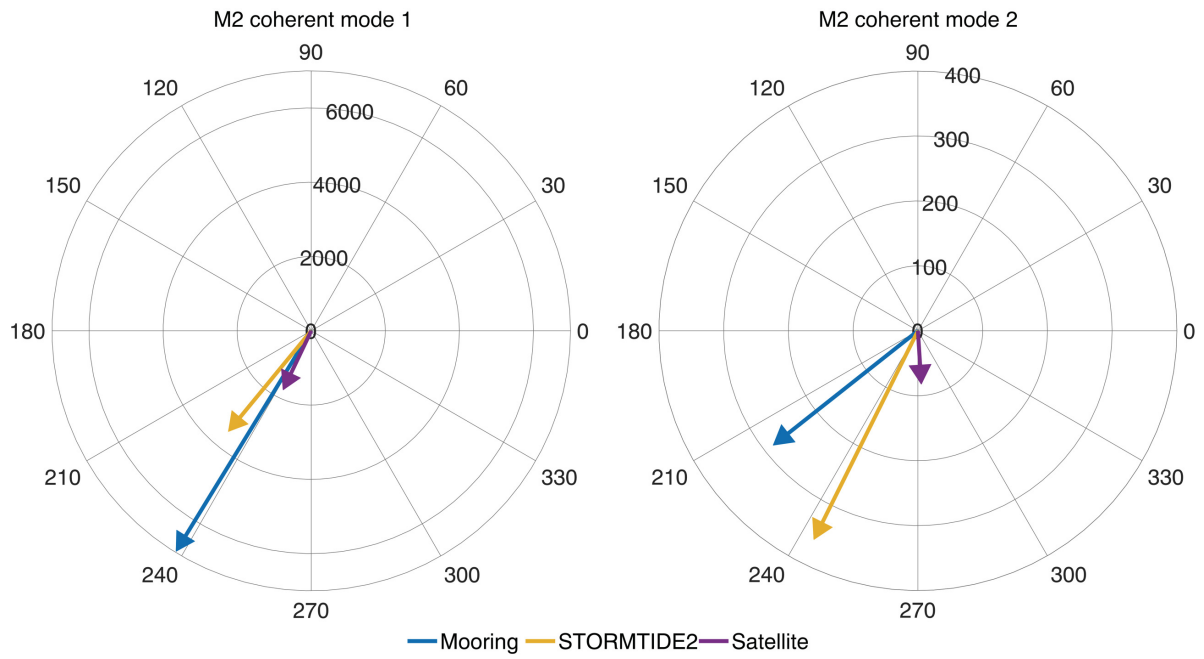

***Figure 6.9**: Mean amplitudes and directions of the M_2 coherent energy flux of the mooring time series (blue), STORMTIDE2 (yellow) and satellite altimetry (purple) agree nicely in mode 1 butter differ in mode 2.*

The underestimation of the mean amplitude of M_2 coherent energy flux in both modes by the satellite altimetry in comparison to the in-situ measurements and STORMTIDE2 likely results from the large spatial and temporal averaging of the satellite data. For the calculation of the energy flux from satellite altimetry, data from more than 20 years of observations have been used. The fitting window is large (160 x 160 km for mode 1, 120 x120 km for mode 2) in comparison with the total width of the tide beam, which is about 150 km (Zhao, 2018; Zhao et al., 2016). Thus, a smeared amplitude of energy flux in this dataset can be expected. The M_2 coherent energy flux during the surface eddy period from satellite altimetry differs of a factor of 2.9 from the in-situ observations. This might be another reasonable comparison to make due to the loss of coherence associated with eddy interaction. With the altimetry only being able to detect the coherent part of energy flux, depending on the overall eddy activity in this area over the 20 years of satellite data.

In general, the M_2 coherent energy flux from the in-situ observations are worse represented in the satellite altimetry dataset than in STORMTIDE2. On one hand, in-situ observations, model and satellite altimetry agree on the direction of mode 1 energy flux and that the total energy flux contains between 4 % and 9 % mode 2 in the M_2 coherent part. On the other hand, the satellite altimetry dataset underestimates the total M_2 coherent energy flux and the direction of the energy flux differs more strongly in mode 2 between STORMTIDE2, the in-situ observations and the data from satellite altimetry.

7 Summary and conclusions

The goal of this study is to analyze the temporal variability of low mode internal waves with a focus on specific events occurring during in-situ observations. I investigated how the temporally variability of energy flux of internal waves looks inside a tide beam, what the main driver of the temporal variability are and how its characteristics change over time. Furthermore, the question arises on how important different events are in compare to the mean of the energy flux. Due to the costs of in-situ observations a further question emerges on how well in-situ measurements are represented in global estimates of internal energy fluxes in state-of-the-art ocean global circulation models and data from satellite altimetry. In general, long-term observations of the temporal variability of energy fluxes of internal waves are sparse and often with a strong regional focus (e.g. Alford et al., 2011; Dohan & Davis, 2011; Silverthorne & Toole, 2009; Vic et al., 2018) with few comparisons on the global scale (Ansong et al., 2017; Simmons & Alford, 2012). Especially the interpretation of their interactions with mesoscale flow is often based on theoretical and idealized studies or numerical models (e.g. Bühler & McIntyre, 2005; Dunphy & Lamb, 2014; Kerry et al., 2014; Ponte & Klein, 2015; Rainville et al., 2010; Zaron & Egbert, 2014; Zhai et al., 2005). This analysis was performed using in-situ data from moored records in an internal tide beam south of the Azores, with a total observation period of about 20 months, and focuses on the M_2 internal tide and near-inertial internal waves generated by the wind. In more detail, the amount of coherent energy flux of the internal tides, the direction of the energy flux and its modal composition, and their time series of potential and kinetic energy are investigated, also in relation to particular events that caused changes in these properties. The first type of events are surface and subsurface intensified mesoscale eddies. To my knowledge this is the first study where a mooring based observational comparison of the M_2 internal tide energy flux between distinct eddy phases and a no-eddy phase in the open ocean is performed. The second type of event is the occurrence of strong winds, with a Beaufort number of 9, classified as a strong gale. Here as well, no study could be found which compares the influence of a strong wind event with the background state of near-inertial internal wave energy flux by mooring observations. This analysis is complemented by comparisons with energy fluxes calculated from the global ocean circulation model STORMTIDE2 and M_2 coherent energy fluxes derived from satellite altimetry.

Regarding the M_2 internal tides the following list provides a comprehensive summary of the main findings regarding the in-situ measurements followed by the consequences of the interaction of the internal tide with eddies:

- The energy flux shows a strong spring-neap variability with a dominance of mode 1.
- The time lag between energy flux and barotropic tide was successfully used to verify the seamount chain south of the Azores as generation site for the internal tides.
- The direction of the energy flux does not vary much in time and is steadily pointing away from its generation site.
- The kinetic energy usually exceeds the potential energy as expected for a freely propagating internal wave.
- The distortion parameter *d* (standard deviation normalized by the mean) and the consistency check r_ω (as indicator for intrusions of other frequencies) were successfully used in combination of eddy kinetic energy calculations to identify distinct eddy periods.

During the deployment four distinct eddies were passing over the mooring location, which allowed me to study the influence of mesoscale motions onto the low-mode internal tide energy flux. The time series was split in five sections, two surface eddy periods, two subsurface eddy periods and one no-eddy time period and are summarized in the following:

- Apart from the spring-neap variability, the strongest changes in the internal tide energy flux are observed during times when eddies pass over the mooring. During eddy periods the characteristics of the energy flux changed considerably indicating an interaction between the mesoscale structures and the internal tide.
- The eddy interactions are dampening the energy flux, increase the directional variability and decreases the coherence, while all these effects have a stronger impact on the second mode in compare to the first mode.
- Eddies induced changes in the stratification seem to have a neglectable impact on the modal decomposition process.
- The eddy interactions can lead to a refraction of the propagation path of each individual mode, a shift in the interference pattern of the tide beam and the scattering of energy into higher modes.

- The observations generally agree with other observations and results from theory and idealized models.

Direct measurements of the energy decrease of internal tides away from their generation site provide an important insight on how much energy is available for mixing but their interpretation is challenging due to their temporal and spatial inhomogeneity. Here in this study the main temporal variability, beside the spring-neap variability inherent in the forcing, lies in the presence of mesoscale eddies. These eddies do not only influence the temporal variability of the energy flux but also the spatial variability by changing the interference pattern of waves from multiple sources (Dunphy & Lamb, 2014; Rainville et al., 2010; Zaron & Egbert, 2014). Understanding the variability of internal tides is important to interpret sparse observations of ocean mixing and a key factor in improving parameterizations for climate models. My study supports the role of strong mesoscale variability in transforming the energy of internal tides into mixing (Kerry et al., 2014; Whalen et al., 2012). The mechanism for deep-ocean mixing away from internal tide generation sites, provided by scattering of low-mode internal tide energy to higher modes through interactions with mesoscale eddies, contributes to the spatially varying non-uniform distribution of diapycnal mixing (Simmons, Jayne, et al., 2004; St. Laurent & Simmons, 2006; Walter & Mertens, 2013; Walter et al., 2005; Waterhouse et al., 2014; Whalen et al., 2018). Furthermore, the coherence of internal tides is an important factor for their detection using satellite altimetry. When internal tides propagate through the ocean, currents and variations in stratification can modify their phase and group speed and ultimately make them incoherent and create a fictitious energy loss along the propagation path. It is important to improve the separation between true dissipation and loss of coherence to get a better representation of internal tide energy from satellite altimetry.

Regarding the near-inertial internal waves the following list provides a comprehensive summary of the main observations regarding the in-situ measurements. It consists a strong wind event that has an impact on the near-inertial energy fluxes, causing a major peak in the time series. This wind event was a strong gale with a Beaufort number of 9. I compared this event with what I call a background state, where no such event could be detected.

- The amplitude of the energy flux time series is not steady because of its intermittent forcing by the wind. It is not dominated by either mode 1 or mode 2, which are contributing in a similar way to the mean. Moreover, the direction of the energy flux has a higher variability than the internal tides in this region.

- As for the internal tides the kinetic energy usually exceeds potential energy, as indicator for a freely propagating internal wave.

- The energy flux during the wind event is characterized by a primarily dominance of mode 1 followed by a dominance of mode 2 (which is consistent with mode 1 and mode 2 group speeds) with a distinct direction away from the area of the main wind power input.

- The energy flux during the wind event was about 7.5 times higher than during the background and one needs about 152 days of background to accumulate the same amount of energy flux which was generated by the wind event.

- The fraction of mode 1 to mode 2 does not change between wind event and background state.

- A calculation of the vertical group speed of mode 1 near-inertial waves is weakening the description via mode separation during the strong wind event, but most fundamental properties seem to be properly displayed.

- No clear indications of an interaction of the near-inertial waves with eddies could be identified, but indications for non-linear interactions between the near-inertial waves and the internal tide in the form of resonant triad interaction (PSI) and non-linear self-interaction are found and cannot be excluded.

- Generally, the observed near-inertial energy fluxes agree with other observational studies. They display a comparable amount of energy and energy flux similar to those of internal tides and also radiate an appreciable fraction away from their generation site.

This study provides new insights on the relative importance of single wind-events regarding the energy flux time series in perspective to a background state of near-inertial energy flux. It reinforces the assumption of a global strongly nonuniform distribution of near-inertial energy with emphasis on regions where such events occur often and regularly (Alford et al., 2016). But also, the background state is comparable to the energy flux from the internal tides, which displays its importance for creating energetically consistent ocean models and generating estimates on how much energy is available for (deep) ocean mixing as an equally important component next to the internal tides. The basic distribution of energy between low and high modes of near-inertial waves was not well measured by the Ocean Storms Experiment (Alford et al., 2016; D'Asaro et al., 1995) and subsequently constrained by few full depth time series (Alford, 2010; Silverthorne & Toole, 2009). This study showed an almost equal contribution of mode 1 and mode 2 for the sum of the measured in-situ energy flux during the background but also during the strong wind event. This could suggest that higher modes still contain a more appreciable amount of energy than in internal tides. This would make higher modes of

near-inertial waves inevitably more important as often suggested (D'Asaro et al., 1995; Gill, 1984). One of the most important but unclear issue is the role of mesoscale eddies and their interaction with near-inertial waves. Unfortunately, even in this study where several distinct eddies are passing over the mooring location no clear indications for interactions could be identified. Due to the intermittency in their forcing and their generation all around the mooring location the ascertainment of single effects seems impractical to single in-situ measurements like this. Hence, stronger effort in theoretical studies and realistic models seems to be a more promising way in answering the question of how exactly these interactions look like. Moreover, the very local nature of the in-situ measurements does not allow a detailed investigation of the fate of the energy that is injected in the deep ocean. While many studies have used the power input from the wind to surface currents to obtain an upper bound of the power available for near-inertial waves, only few of them provide an estimate of the fraction of energy that propagates at depth with values between 10 % to 30 % (Cuypers et al., 2013; Furuichi et al., 2008; von Storch et al., 2007; Zhai et al., 2009).

The last part of this work focuses on the comparison of internal tide energy fluxes and near-inertial wave energy fluxes from the in-situ measurements with an ocean general circulation model (STORMTIDE2) and data based on satellite altimetry. Following is a comprehensive summary of the main findings:

- A comparison between point-wise measurements, such as the in-situ observations, with large datasets such as the STORMTIDE2 model and M_2 coherent energy fluxes derived from satellite altimetry is possible for the internal tide, due to its position in a tide beam, but is hampered for the near-inertial component.

- The semidiurnal internal tides from STORMTIDE2 show a strong spring-neap variability and a domination of mode 1, comparable with the in-situ observations. However, STORMTIDE2 underestimates the total energy flux by a factor of about 2, which is likely caused by a too high numerical damping inside the model. The direction of the semidiurnal energy flux is in both modes in good agreement with the in-situ observations and show a low directional variability, and is steadily pointing away from the generation site. But STORMTIDE2 shows however, a higher coherence of the energy in mode 2 than the in-situ observations.

- The underestimation of the M_2 coherent part of the energy flux from the STORMTIDE2 model is a factor of about 1.9, and for the energy flux derived from satellite altimetry a factor of about 3.9 in comparison to the in-situ measurements. However, the direction of the M_2 coherent energy flux derived from satellite altimetry and from the STORMTIDE2 model are in good agreement with the in-situ observation in mode 1, but

they differ in mode 2. All three dataset agree that the ratio between mode 1 and mode 2 in the total M_2 coherent internal tide contains between 91 %, to 96 % mode 1.

- The energy flux of the near-inertial waves from the STORMTIDE2 model is one order of magnitude lower than the in-situ measurements, which is likely caused by a combination of a too high numerical damping and an insufficient resolution of the wind input used in the model. Nevertheless, the near-inertial energy flux from STORMTIDE2 shows a similar directional variability and a similar fraction between mode 1 and mode 2 compared to the in-situ measurements.

- The representation of the amplitude of the near-inertial waves in STORMTIDE2 seem to be generally worse than for the internal tides although both having a considerably similar importance for the energy budget of the oceans.

The analysis of the in-situ observations have shown that individual events, like the occurrence of mesoscale eddies and their related damping of the energy flux and the associated reduction of coherence, as well as the occurrence of strong wind events for the near-inertial component which can lead to a sudden and strong generation of internal waves, have a substantial impact on the temporal variability of the energy flux from internal waves and should be adequately represented in newest Ocean General Circulation Models (OGCM's). The stronger underestimation of near-inertial energy fluxes in comparison to the underestimation in the internal tides by STORMTIDE2 is concerning, especially because of the indications that near-inertial waves might have a similar amount of energy on the global scale in comparison to the internal tides. Hence, a better realization of near-inertial internal waves in OGCM's could be more important for the future development of these models than improvements of the internal tide in further details. Many studies have investigated the importance of turbulent mixing driven by internal tide breaking. While the internal tide generation map is relatively well known, the internal tide generation and propagation outside the coastal zone is somewhat deterministic, and their sea surface height signature can be detected by satellite altimetry, the enhanced turbulence caused by near-inertial wave breaking might be equally important but is worse understood. However, the development of appropriate parameterizations of enhanced turbulence by near-inertial wave breaking is still a work in progress because of their poorly understood generation, their temporal intermittency, and their possibly greater tendency of interactions with mesoscale motions (Zhao et al., 2016).

A generally good representation of internal waves, their generation, propagation and dissipation are needed in OGCM's in order to characterize the impact of internal waves energy onto the climate. Although the horizontal resolution of state of the art OGCMs is nowadays generally sufficient to represent (at least) low mode internal waves, two major difficulties arise by representing storm induced near-inertial waves. First the atmospheric wind forcing

at finer scales are usually not resolved by current reanalysis products, which are used to force OGCMs (Halliwell et al., 2011). Hereby the resolution of the wind-forcing at the ocean surface plays and important role. The problem with lower-resolution wind-input is the loss of peaks during storm events by smoothing the dataset, which are shown to a have significant importance in generating near-inertial waves. Therefore, more effort is needed to create realistic global wind dataset with a high temporal and spatial resolution which can be implemented in these models. And second, the currently often used parameterizations of dissipation of internal wave energy results in an artificial damping, however newest investigations start to offer feasible solution to this problem (e.g. Juricke et al., 2020; Leclair & Madec, 2011; Pollmann et al., 2019). My findings support the idea that parameterizations of ocean mixing should take also the energy transformation associated with the interaction between internal waves and eddies properly into account, rather than relying mainly on the topographic roughness and pure tidal forcing (Kerry et al., 2014; Liang & Thurnherr, 2012). Few OGCMs resolve simultaneously internal tides and the low-frequency circulation (Arbic et al., 2010; M. Müller et al., 2012) and adequately predict incoherence of low mode internal tides. The rareness, cost and complexity of such realistic models, as well as observations, limit our understanding of internal wave – eddy interaction and the associated coherence of internal tides. My study provides a step towards understanding the role of the temporal variability of internal waves for global ocean mixing estimates.

Future efforts regarding in-situ observations of internal waves seem necessary, especially concerning the generation, propagation and dissipation of near-inertial waves. For example, the relative importance between near-inertial waves generated by wind in compare to other sources like nonlinear wave-wave interactions, spontaneous generations and lee-wave generation is still unknown. Furthermore, there are no dedicated observations between 30°S-30°N on how far towards the equator near-inertial waves are actually going and what ultimately happens with them (Alford 2016). But also, the internal tides still offer a variety of open questions which need to be answered. The next step in investigating the temporal variability of internal tides lies in evaluating the relative importance of the individual processes between the interaction of mesoscale eddies with internal tides. For example, so far it is not clear how important the shift of the interference pattern of internal tides in relation to the refraction of the propagation path of individual modes is. Furthermore, we need to understand how much of the energy, scattered in higher modes by the interaction with eddies, is at the end available for local mixing. An ongoing investigation is also the quantification of the coherence of the internal tide energy flux and the loss of coherence by eddy interaction. These estimations are highly relevant to evaluate the energy fluxes from satellite altimetry in areas with elevated eddy kinetic energy. To tackle these questions, I am planning to deploy two highly equipped moorings which can resolve higher modes of internal wave energy flux, and several Pressure Inverted Echo Sounders (PIES) inside a tide beam in the south Atlantic

Ocean close the Walvis Ridge. The internal tides in this region are prominent to interact with eddies formed by the Agulhas Current (Agulhas Rings). These investigations will be accompanied by the analysis of an OGCM with a horizontal resolution of about 500 m in the focus region and will provide the next step in evaluating the processes relevant for the temporal variability of internal tides and their necessity to be implemented in parameterizations in climate models.

Acknowledgements

There are many people out there who strongly supported me in writing this thesis and without them this document might not exist. First of all, I want to thank Janna Köhler. If I would be asked to describe Janna in one word it would be outstanding. Besides the great scientific support provided by her, she is a very heartwarming and kind person. She became a real friend and is the perfect partner to share an office with.

I want to deeply thank Maren Walter and Christian Mertens who guided me through my time as a PhD student. They always had an open door and helped me to identify problems and guided me to find the proper solution to them. In many senses they became role-models for a-lot of aspects in my life. Monika Rhein gave me the possibility to write this thesis, her scientific knowledge and her positive and supportive attitude was always a great help. She always stood up for me and encouraged me to give my very best.

Zhongxiang Zhao, did not only provided the satellite altimetry datasets but was also part of my thesis committee, in which he provided great scientific support and helped me to look at problems from a different angle. Zhuhua Li and Jin-Song von Storch who provided the STORMTIDE2 dataset were always happy to answer as many questions as I can think of. I want to thank Dirk Olbers for several fruitful and educational discussions, his general interest in science is truly fascinating and should be an example for every researcher. Furthermore, during my time as PhD student I was strongly supported by all members of the physical oceanography working group. They provided not on only scientific input, but also technical and moral support whenever needed.

Special thanks go to the entire staff of the TRR181, especially Meike Ruhnau, Jennifer Fandrich and Carsten Eden, who agreed to be part of my thesis committee as well. The summer schools, workshops, and retreats organized by them were always great experiences that I still like to think back to and where I learned how good interdisciplinary science can work. Being part of the TRR181 and the membership in the Bremen International Graduate School for Marine Sciences (GLOMAR) gave me the opportunity to participate in several international conferences and workshops by giving financial support. Moreover, their soft skill courses were of great value and will be very helpful in the future.

Many thanks go to the entire crew of the research vessel FS Poseidon, with their help we realized three successful cruises south of the Azores. They strongly helped by providing the scientific infrastructure for the in-situ measurements used in this thesis.

My deepest gratitude goes to my beloved wife Ilaria Stendardo and my son Jacob. They sometimes had a hard time dealing with a moody and stressed husband/father but always got my back. They took me through the three sea voyages morally and never doubted that I would make it. I love you.

Declaration of Originality

I, Jonas Löb, hereby affirm that the presented work has been done without unauthorized assistance, that I have not used any sources and aids other than those I have indicated, and that I have identified the parts of the works used, either literally or in terms of content, as such. Parts of chapter 2, 3, 4, and 6 have been published to the Journal Geophysical Research Ocean under the title "*Observations of the low mode internal tide and its interaction with mesoscale flow south of the Azores"* (Löb et al., 2020). The text of the previously published chapters has been adapted in order to fit the context of a thesis.

Jonas Löb Date:

Table of Figures

Bibliography

Alford, M. H. (2001). Internal Swell Generation: The Spatial Distribution of Energy Flux from the Wind to Mixed Layer Near-Inertial Motions. *Journal of Physical Oceanography, 31*(8), 2359-2368. doi:10.1175/1520-0485(2001)031<2359:Isgtsd>2.0.Co;2

Alford, M. H. (2003a). Improved global maps and 54-year history of wind-work on ocean inertial motions. *Geophysical Research Letters, 30*(8). doi:doi:10.1029/2002GL016614

Alford, M. H. (2003b). Redistribution of energy available for ocean mixing by long-range propagation of internal waves. *Nature, 423*, 159. doi:10.1038/nature01628

Alford, M. H. (2010). Sustained, Full-Water-Column Observations of Internal Waves and Mixing near Mendocino Escarpment. *Journal of Physical Oceanography, 40*(12), 2643-2660. doi:10.1175/2010jpo4502.1

Alford, M. H., Cronin, M. F., & Klymak, J. M. (2012). Annual Cycle and Depth Penetration of Wind-Generated Near-Inertial Internal Waves at Ocean Station Papa in the Northeast Pacific. *Journal of Physical Oceanography, 42*(6), 889-909. doi:10.1175/JPO-D-11-092.1

Alford, M. H., Gregg, M. C., & Merrifield, M. A. (2006). Structure, Propagation, and Mixing of Energetic Baroclinic Tides in Mamala Bay, Oahu, Hawaii. *Journal of Physical Oceanography, 36*(6), 997-1018. doi:10.1175/jpo2877.1

Alford, M. H., MacKinnon, J. A., Nash, J. D., Simmons, H., Pickering, A., Klymak, J. M., . . . Lu, C.-W. (2011). Energy Flux and Dissipation in Luzon Strait: Two Tales of Two Ridges. *Journal of Physical Oceanography, 41*(11), 2211-2222. doi:10.1175/jpo-d-11-073.1

Alford, M. H., MacKinnon, J. A., Simmons, H. L., & Nash, J. D. (2016). Near-Inertial Internal Gravity Waves in the Ocean. *Ann Rev Mar Sci, 8*, 95-123. doi:10.1146/annurev-marine-010814-015746

Alford, M. H., Mickett, J. B., Zhang, S., MacCready, P., Zhao, Z., & Newton, J. (2012). Internal Waves on the Washington Continental Shelf. *Oceanography, 25*. doi:https://doi.org/10.5670/oceanog.2012.43

Alford, M. H., & Whitmont, M. (2007). Seasonal and Spatial Variability of Near-Inertial Kinetic Energy from Historical Moored Velocity Records. *Journal of Physical Oceanography, 37*(8), 2022-2037. doi:10.1175/jpo3106.1

Alford, M. H., & Zhao, Z. (2007a). Global Patterns of Low-Mode Internal-Wave Propagation. Part I: Energy and Energy Flux. *Journal of Physical Oceanography, 37*(7), 1829-1848. doi:10.1175/jpo3085.1

Alford, M. H., & Zhao, Z. (2007b). Global Patterns of Low-Mode Internal-Wave Propagation. Part II: Group Velocity. *Journal of Physical Oceanography, 37*(7), 1849-1858. doi:10.1175/jpo3086.1

Anderson, D. L. T., & Gill, A. E. (1979). Beta dispersion of inertial waves. *Journal of Geophysical Research: Oceans, 84*(C4), 1836-1842. doi:10.1029/JC084iC04p01836

Ansong, J. K., Arbic, B. K., Alford, M. H., Buijsman, M. C., Shriver, J. F., Zhao, Z., . . . Zamudio, L. (2017). Semidiurnal internal tide energy fluxes and their variability in a Global Ocean Model and moored observations. *Journal of Geophysical Research: Oceans, 122*(3), 1882-1900. doi:doi:10.1002/2016JC012184

Ansong, J. K., Arbic, B. K., Buijsman, M. C., Richman, J. G., Shriver, J. F., & Wallcraft, A. J. (2015). Indirect evidence for substantial damping of low-mode internal tides in the open ocean. *Journal of Geophysical Research: Oceans, 120*(9), 6057-6071. doi:10.1002/2015jc010998

Arbic, B. K., Richman, J. G., Shriver, J. F., Timko, P. G., Metzger, E. J., & Wallcraft, A. J. (2012). Global Modeling of Internal Tides Within an Eddying Ocean General Circulation Model. *Oceanography, 25*. doi:https://doi.org/10.5670/oceanog.2012.38

Arbic, B. K., Wallcraft, A. J., & Metzger, E. J. (2010). Concurrent simulation of the eddying general circulation and tides in a global ocean model. *Ocean Modelling, 32*(3), 175-187. doi:https://doi.org/10.1016/j.ocemod.2010.01.007

Baines, P. G. (1982). On internal tide generation models. *Deep Sea Research Part A. Oceanographic Research Papers, 29*(3), 307-338. doi:https://doi.org/10.1016/0198-0149(82)90098-X

Baker, L. E., & Sutherland, B. R. (2020). The evolution of superharmonics excited by internal tides in non-uniform stratification. *Journal of Fluid Mechanics, 891*, R1. doi:10.1017/jfm.2020.188

Balmforth, N. J., Llewellyn Smith, S. G., & Young, W. R. (1998). Enhanced dispersion of near-inertial waves in an idealized geostrophic flow. *Journal of Marine Research, 56*(1), 1-40. doi:10.1357/002224098321836091

Balmforth, N. J., & Young, W. R. (1999). Radiative damping of near-inertial oscillations in the mixed layer. *Journal of Marine Research, 57*(4), 561-584. doi:10.1357/002224099321549594

Bell, T. H. (1975a). Lee waves in stratified flows with simple harmonic time dependence. *Journal of Fluid Mechanics, 67*(4), 705-722. doi:10.1017/S0022112075000560

Bell, T. H. (1975b). Topographically generated internal waves in the open ocean. *Journal of Geophysical Research, 80*(3), 320-327. doi:10.1029/JC080i003p00320

Brown, E. D., & Owens, W. B. (1981). Observations of the Horizontal Interactions between the Internal Wave Field and the Mesoscale Flow. *Journal of Physical Oceanography, 11*(11), 1474-1480. doi:10.1175/1520-0485(1981)011<1474:Oothib>2.0.Co;2

Bühler, O., & McIntyre, M. E. (2005). Wave capture and wave–vortex duality. *Journal of Fluid Mechanics, 534*, 67-95. doi:10.1017/S0022112005004374

Buijsman, M. C., Arbic, B. K., Richman, J. G., Shriver, J. F., Wallcraft, A. J., & Zamudio, L. (2017). Semidiurnal internal tide incoherence in the equatorial Pacific. *Journal of Geophysical Research: Oceans, 122*(7), 5286-5305. doi:10.1002/2016jc012590

Cacchione, D. A., Pratson, L. F., & Ogston, A. S. (2002). The Shaping of Continental Slopes by Internal Tides. *Science, 296*(5568), 724. doi:10.1126/science.1069803

Carter, G. S., & Gregg, M. C. (2002). Intense, Variable Mixing near the Head of Monterey Submarine Canyon. *Journal of Physical Oceanography, 32*(11), 3145-3165. doi:10.1175/1520-0485(2002)032<3145:Ivmnth>2.0.Co;2

Chaigneau, A., Pizarro, O., & Rojas, W. (2008). Global climatology of near-inertial current characteristics from Lagrangian observations. *Geophysical Research Letters, 35*(13). doi:10.1029/2008gl034060

Chavanne, C., Flament, P., Luther, D., & Gurgel, K.-W. (2010). The Surface Expression of Semidiurnal Internal Tides near a Strong Source at Hawaii. Part II: Interactions with Mesoscale Currents. *Journal of Physical Oceanography, 40*(6), 1180-1200. doi:10.1175/2010jpo4223.1

Chou, S. H., Luther, D. S., Guiles, M. D., Carter, G. S., & Decloedt, T. (2014). An empirical investigation of nonlinear energy transfer from the M2 internal tide to diurnal wave motions in the Kauai Channel, Hawaii. *Geophysical Research Letters, 41*(2), 505-512. doi:10.1002/2013gl058320

Crawford, G. B., & Large, W. G. (1996). A Numerical Investigation of Resonant Inertial Response of the Ocean to Wind Forcing. *Journal of Physical Oceanography, 26*(6), 873-891. doi:10.1175/1520-0485(1996)026<0873:Aniori>2.0.Co;2

Cummins, P. F., Cherniawsky, J. Y., & Foreman, M. G. G. (2001). North Pacific internal tides from the Aleutian Ridge: Altimeter observations and modeling. *Journal of Marine Research, 59*(2), 167-191. doi:10.1357/002224001762882628

Cusack, J. M., Brearley, J. A., Naveira Garabato, A. C., Smeed, D. A., Polzin, K. L., Velzeboer, N., & Shakespeare, C. J. (2020). Observed eddy-internal wave interactions in the Southern Ocean. *Journal of Physical Oceanography*, 1-62. doi:10.1175/jpo-d-20-0001.1

Cuypers, Y., Le Vaillant, X., Bouruet-Aubertot, P., Vialard, J., & McPhaden, M. J. (2013). Tropical storm-induced near-inertial internal waves during the Cirene experiment: Energy fluxes and impact on vertical mixing. *Journal of Geophysical Research: Oceans, 118*(1), 358-380. doi:10.1029/2012jc007881

D'Asaro, E. A., Eriksen, C. C., Levine, M. D., paulson, C. A., Niiler, P., & Van Meurs, P. (1995). Upper-Ocean Inertial Currents Forced by a Strong Storm. Part I: Data and Comparisons with Linear Theory. *Journal of Physical Oceanography, 25*(11), 2909-2936. doi:10.1175/1520-0485(1995)025<2909:Uoicfb>2.0.Co;2

D'Asaro, E. A. (1995a). Upper-Ocean Inertial Currents Forced by a Strong Storm. Part II: Modeling. *Journal of Physical Oceanography, 25*(11), 2937-2952. doi:10.1175/1520-0485(1995)025<2937:Uoicfb>2.0.Co;2

D'Asaro, E. A. (1995b). Upper-Ocean Inertial Currents Forced by a Strong Storm. Part III: Interaction of Inertial Currents and Mesoscale Eddies. *Journal of Physical Oceanography, 25*(11), 2953-2958. doi:10.1175/1520-0485(1995)025<2953:Uoicfb>2.0.Co;2

Danioux, E., Klein, P., & Rivière, P. (2008). Propagation of Wind Energy into the Deep Ocean through a Fully Turbulent Mesoscale Eddy Field. *Journal of Physical Oceanography, 38*(10), 2224-2241. doi:10.1175/2008jpo3821.1

de Lavergne, C., Falahat, S., Madec, G., Roquet, F., Nycander, J., & Vic, C. (2019). Toward global maps of internal tide energy sinks. *Ocean Modelling, 137*, 52-75. doi:https://doi.org/10.1016/j.ocemod.2019.03.010

Dohan, K., & Davis, R. E. (2011). Mixing in the Transition Layer during Two Storm Events. *Journal of Physical Oceanography, 41*(1), 42-66. doi:10.1175/2010jpo4253.1

Dunphy, M., & Lamb, K. G. (2014). Focusing and vertical mode scattering of the first mode internal tide by mesoscale eddy interaction. *Journal of Geophysical Research: Oceans, 119*(1), 523-536. doi:10.1002/2013jc009293

Dunphy, M., Ponte, A. L., Klein, P., & Gentil, S. L. (2017). Low-Mode Internal Tide Propagation in a Turbulent Eddy Field. *Journal of Physical Oceanography, 47*(3), 649-665. doi:10.1175/jpo-d-16-0099.1

Dushaw, B. D., Howe, B. M., Cornuelle, B. D., Worcester, P. F., & Luther, D. S. (1995). Barotropic and Baroclinic Tides in the Central North Pacific Ocean Determined from Long-Range Reciprocal Acoustic Transmissions. *Journal of Physical Oceanography, 25*(4), 631-647. doi:10.1175/1520-0485(1995)025<0631:Babtit>2.0.Co;2

Dushaw, B. D., Worcester, P. F., & Dzieciuch, M. A. (2011). On the predictability of mode-1 internal tides. *Deep Sea Research Part I: Oceanographic Research Papers, 58*(6), 677-698. doi:https://doi.org/10.1016/j.dsr.2011.04.002

Eden, C. (2007). Eddy length scales in the North Atlantic Ocean. *Journal of Geophysical Research: Oceans, 112*(C6). doi:10.1029/2006jc003901

Eden, C., Czeschel, L., & Olbers, D. (2014). Toward Energetically Consistent Ocean Models. *Journal of Physical Oceanography, 44*(12), 3160-3184. doi:10.1175/jpo-d-13-0260.1

Egbert, G. D., & Erofeeva, S. Y. (2002). Efficient Inverse Modeling of Barotropic Ocean Tides. *Journal of Atmospheric and Oceanic Technology, 19*(2), 183-204. doi:10.1175/1520-0426(2002)019<0183:Eimobo>2.0.Co;2

Egbert, G. D., & Ray, R. D. (2000). Significant dissipation of tidal energy in the deep ocean inferred from satellite altimeter data. *Nature, 405*, 775. doi:10.1038/35015531

Egbert, G. D., & Ray, R. D. (2001). Estimates of M2 tidal energy dissipation from TOPEX/Poseidon altimeter data. *Journal of Geophysical Research: Oceans, 106*(C10), 22475-22502. doi:10.1029/2000jc000699

Egbert, G. D., & Ray, R. D. (2017). Tidal Prediction. *Journal of Marine Research, 75*(3), 189-237. doi:10.1357/002224017821836761

Elipot, S., Lumpkin, R., & Prieto, G. (2010). Modification of inertial oscillations by the mesoscale eddy field. *Journal of Geophysical Research: Oceans, 115*(C9). doi:10.1029/2009jc005679

Ferrari, R., & Wunsch, C. (2009). Ocean Circulation Kinetic Energy: Reservoirs, Sources, and Sinks. *Annual Review of Fluid Mechanics, 41*(1), 253-282. doi:10.1146/annurev.fluid.40.111406.102139

Firing, E., Lien, R.-C., & Muller, P. (1997). Observations of strong inertial oscillations after the passage of Tropical Cyclone Ofa. *Journal of Geophysical Research: Oceans, 102*(C2), 3317-3322. doi:10.1029/96jc03497

Fischer, J., & Visbeck, M. (1993). Seasonal variation of the daily zooplankton migration in the Greenland sea. *Deep Sea Research Part I: Oceanographic Research Papers, 40*(8), 1547-1557. doi:https://doi.org/10.1016/0967-0637(93)90015-U

Fu, L.-L. (1981). Observations and models of inertial waves in the deep ocean. *Reviews of Geophysics, 19*(1), 141-170. doi:doi:10.1029/RG019i001p00141

Furuichi, N., Hibiya, T., & Niwa, Y. (2005). Bispectral Analysis of Energy Transfer within the Two-Dimensional Oceanic Internal Wave Field. *Journal of Physical Oceanography, 35*(11), 2104-2109. doi:10.1175/jpo2816.1

Furuichi, N., Hibiya, T., & Niwa, Y. (2008). Model-predicted distribution of wind-induced internal wave energy in the world's oceans. *Journal of Geophysical Research, 113*(C9). doi:10.1029/2008jc004768

Garabato, A. C. N., Polzin, K. L., King, B. A., Heywood, K. J., & Visbeck, M. (2004). Widespread Intense Turbulent Mixing in the Southern Ocean. *Science, 303*(5655), 210. doi:10.1126/science.1090929

Garrett, C., & Kunze, E. (2007). Internal Tide Generation in the Deep Ocean. *Annual Review of Fluid Mechanics, 39*(1), 57-87. doi:10.1146/annurev.fluid.39.050905.110227

Garrett, C., & Munk, W. (1972). Space-Time scales of internal waves. *Geophysical Fluid Dynamics, 3*(3), 225-264. doi:10.1080/03091927208236082

Garrett, C., & Munk, W. (1979). Internal Waves in the Ocean. *Annual Review of Fluid Mechanics, 11*(1), 339-369. doi:10.1146/annurev.fl.11.010179.002011

Gill, A. E. (1984). On the Behavior of Internal Waves in the Wakes of Storms. *Journal of Physical Oceanography, 14*(7), 1129-1151. doi:10.1175/1520-0485(1984)014<1129:Otboiw>2.0.Co;2

Griffies, S. M. (2004). Fundamentals of Ocean Climate Models. *Princeton University Press*, 528 pp.

Griffies, S. M., Böning, C., Bryan, F., Chassignet, E., Gerdes, R., Hasumi, H., . . . Webb, D. (2000). Developments in Ocean Climate Modelling. *Ocean Modelling, 2*, 123-192. doi:10.1016/S1463-5003(00)00014-7

Haidvogel, D. B., & Beckmann, A. (1999). Numerical ocean circulation modeling. *Imperial College Press*, 344.

Haji, M. N. (2015). *Scattering of the low-mode internal tide at the Line Islands Ridge.* (Master thesis). Massachusetts Institute of Technology,

Halliwell, G. R., Jr., Shay, L. K., Brewster, J. K., & Teague, W. J. (2011). Evaluation and Sensitivity Analysis of an Ocean Model Response to Hurricane Ivan. *Monthly Weather Review, 139*(3), 921-945. doi:10.1175/2010mwr3104.1

Haney, S., & Young, W. R. (2017). Radiation of internal waves from groups of surface gravity waves. *Journal of Fluid Mechanics, 829*, 280-303. doi:10.1017/jfm.2017.536

Hendry, R. M., & Charnock, H. (1977). Observations of the semidiurnal internal tide in the western North Atlantic Ocean. *Philosophical Transactions of the Royal Society of London. Series A, Mathematical and Physical Sciences, 286*(1330), 1-24. doi:doi:10.1098/rsta.1977.0108

Holloway, P. E., & Merrifield, M. A. (2003). On the spring-neap variability and age of the internal tide at the Hawaiian Ridge. *Journal of Geophysical Research: Oceans, 108*(C4). doi:10.1029/2002jc001486

Jaimes, B., & Shay, L. K. (2010). Near-Inertial Wave Wake of Hurricanes Katrina and Rita over Mesoscale Oceanic Eddies. *Journal of Physical Oceanography, 40*(6), 1320-1337. doi:10.1175/2010jpo4309.1

Jayne, S. R. (2009). The Impact of Abyssal Mixing Parameterizations in an Ocean General Circulation Model. *Journal of Physical Oceanography, 39*(7), 1756-1775. doi:10.1175/2009jpo4085.1

Jayne, S. R., & St. Laurent, L. C. (2001). Parameterizing tidal dissipation over rough topography. *Geophysical Research Letters, 28*, 811. doi:10.1029/2000gl012044

Jeon, C., Park, J.-H., Nakamura, H., Nishina, A., Zhu, X.-H., Kim, D. G., . . . Hirose, N. (2019). Poleward-propagating near-inertial waves enabled by the western boundary current. *Scientific Reports, 9*(1), 9955. doi:10.1038/s41598-019-46364-9

Jiang, J., Lu, Y., & Perrie, W. (2005). Estimating the energy flux from the wind to ocean inertial motions: The sensitivity to surface wind fields. *Geophysical Research Letters, 32*(15). doi:doi:10.1029/2005GL023289

Jones, W. L. (1968). Reflexion and stability of waves in stably stratified fluids with shear flow: a numerical study. *Journal of Fluid Mechanics, 34*(3), 609-624. doi:10.1017/S0022112068002119

Juricke, S., Danilov, S., Koldunov, N., Oliver, M., & Sidorenko, D. (2020). Ocean Kinetic Energy Backscatter Parametrization on Unstructured Grids: Impact on Global Eddy-Permitting Simulations. *Journal of Advances in Modeling Earth Systems, 12*(1), e2019MS001855. doi:10.1029/2019ms001855

Kantha, L. H., & Tierney, C. C. (1997). Global baroclinic tides. *Progress in Oceanography, 40*(1), 163-178. doi:https://doi.org/10.1016/S0079-6611(97)00028-1

Kelly, S. M. (2019). Coastally Generated Near-Inertial Waves. *Journal of Physical Oceanography, 49*(11), 2979-2995. doi:10.1175/JPO-D-18-0148.1

Kelly, S. M., Jones, N. L., Ivey, G. N., & Lowe, R. J. (2015). Internal-Tide Spectroscopy and Prediction in the Timor Sea. *Journal of Physical Oceanography, 45*(1), 64-83. doi:10.1175/jpo-d-14-0007.1

Kelly, S. M., & Lermusiaux, P. F. J. (2016). Internal-tide interactions with the Gulf Stream and Middle Atlantic Bight shelfbreak front. *Journal of Geophysical Research: Oceans, 121*(8), 6271-6294. doi:10.1002/2016jc011639

Kelly, S. M., Lermusiaux, P. F. J., Duda, T. F., & Jr., P. J. H. (2016). A Coupled-Mode Shallow-Water Model for Tidal Analysis: Internal Tide Reflection and Refraction by the Gulf Stream. *Journal of Physical Oceanography, 46*(12), 3661-3679. doi:10.1175/jpo-d-16-0018.1

Kelly, S. M., & Nash, J. D. (2010). Internal-tide generation and destruction by shoaling internal tides. *Geophysical Research Letters, 37*(23). doi:10.1029/2010gl045598

Kerry, C. G., Powell, B. S., & Carter, G. S. (2014). The Impact of Subtidal Circulation on Internal-Tide-Induced Mixing in the Philippine Sea. *Journal of Physical Oceanography, 44*(12), 3209-3224. doi:10.1175/jpo-d-13-0249.1

Kerry, C. G., Powell, B. S., & Carter, G. S. (2016). Quantifying the Incoherent M2 Internal Tide in the Philippine Sea. *Journal of Physical Oceanography, 46*(8), 2483-2491. doi:10.1175/jpo-d-16-0023.1

Klein, B., & Siedler, G. (1989). On the origin of the Azores Current. *Journal of Geophysical Research: Oceans, 94*(C5), 6159-6168. doi:10.1029/JC094iC05p06159

Klein, P., Lapeyre, G., & Large, W. G. (2004). Wind ringing of the ocean in presence of mesoscale eddies. *Geophysical Research Letters, 31*(15). doi:10.1029/2004gl020274

Klein, P., Smith, S. L., & Lapeyre, G. (2004). Organization of near-inertial energy by an eddy field. *Quarterly Journal of the Royal Meteorological Society, 130*(598), 1153-1166. doi:10.1256/qj.02.231

Klein, P., & Treguier, A. M. (1995). Dispersion of wind-induced inertial waves by a barotropic jet. *Journal of Marine Research, 53*(1), 1-22. doi:10.1357/0022240953213331

Klymak, J. M., Moum, J. N., Nash, J. D., Kunze, E., Girton, J. B., Carter, G. S., . . . Gregg, M. C. (2006). An Estimate of Tidal Energy Lost to Turbulence at the Hawaiian Ridge. *Journal of Physical Oceanography, 36*(6), 1148-1164. doi:10.1175/jpo2885.1

Köhler, J., & Löb, J. (2019). RV POSEIDON 533/2 Cruise Report / Fahrtbericht Las Palmas (Gran Canaria) 25.03.2019 Ponta Delgada (Azores) 01.04.2019 POS533/2 - ENERGY

TRANSFER III. *Zentrum für Marine Umweltwissenschaften, Universität Bremen*. doi:10.3289/CR_POS533_2

Köhler, J., Walter, M., Mertens, C., Stiehler, J., Li, Z., Zhao, Z., . . . Rhein, M. (2019). Energy Flux Observations in an Internal Tide Beam in the Eastern North Atlantic. *Journal of Geophysical Research: Oceans, 124*(8), 5747-5764. doi:10.1029/2019jc015156

Komori, N., Ohfuchi, W., Taguchi, B., Sasaki, H., & Klein, P. (2008). Deep ocean inertia-gravity waves simulated in a high-resolution global coupled atmosphere–ocean GCM. *Geophysical Research Letters, 35*(4). doi:10.1029/2007gl032807

Krauss, W., Döscher, R., Lehmann, A., & Viehoff, T. (1990). On eddy scales in the eastern and northern North Atlantic Ocean as a function of latitude. *Journal of Geophysical Research: Oceans, 95*(C10), 18049-18056. doi:10.1029/JC095iC10p18049

Kunze, E. (1985). Near-Inertial Wave Propagation In Geostrophic Shear. *Journal of Physical Oceanography, 15*(5), 544-565. doi:10.1175/1520-0485(1985)015<0544:Niwpig>2.0.Co;2

Kunze, E. (1986). The Mean and Near-Inertial Velocity Fields in a Warm-Core Ring. *Journal of Physical Oceanography, 16*(8), 1444-1461. doi:10.1175/1520-0485(1986)016<1444:Tmaniv>2.0.Co;2

Kunze, E., Rosenfeld, L. K., Carter, G. S., & Gregg, M. C. (2002). Internal Waves in Monterey Submarine Canyon. *Journal of Physical Oceanography, 32*(6), 1890-1913. doi:10.1175/1520-0485(2002)032<1890:Iwimsc>2.0.Co;2

Leaman, K. D., & Sanford, T. B. (1975). Vertical energy propagation of inertial waves: A vector spectral analysis of velocity profiles. *Journal of Geophysical Research (1896-1977), 80*(15), 1975-1978. doi:10.1029/JC080i015p01975

Leclair, M., & Madec, G. (2011). z˜-Coordinate, an Arbitrary Lagrangian–Eulerian coordinate separating high and low frequency motions. *Ocean Modelling, 37*(3), 139-152. doi:https://doi.org/10.1016/j.ocemod.2011.02.001

Lee, D.-K., & Niiler, P. P. (1998). The inertial chimney: The near-inertial energy drainage from the ocean surface to the deep layer. *Journal of Geophysical Research: Oceans, 103*(C4), 7579-7591. doi:10.1029/97jc03200

Levine, M. D., & Zervakis, V. (1995). Near-Inertial Wave Propagation into the Pycnocline during Ocean Storms: Observations and Model Comparison. *Journal of Physical Oceanography, 25*(11), 2890-2908. doi:10.1175/1520-0485(1995)025<2890:Niwpit>2.0.Co;2

Li, B., Wei, Z., Wang, X., Fu, Y., Fu, Q., Li, J., & Lv, X. (2020). Variability of coherent and incoherent features of internal tides in the north South China Sea. *Scientific Reports, 10*(1), 12904. doi:10.1038/s41598-020-68359-7

Li, Q., Mao, X., Huthnance, J., Cai, S., & Kelly, S. (2019). On Internal Waves Propagating across a Geostrophic Front. *Journal of Physical Oceanography, 49*(5), 1229-1248. doi:10.1175/jpo-d-18-0056.1

Li, Z., von Storch, J.-S., & Müller, M. (2015). The M2 Internal Tide Simulated by a 1/10° OGCM. *Journal of Physical Oceanography, 45*(12), 3119-3135. doi:10.1175/jpo-d-14-0228.1

Li, Z., von Storch, J.-S., & Müller, M. (2017). The K1 internal tide simulated by a 1/10° OGCM. *Ocean Modelling, 113*, 145-156. doi:https://doi.org/10.1016/j.ocemod.2017.04.002

Liang, X., & Thurnherr, A. M. (2012). Eddy-Modulated Internal Waves and Mixing on a Midocean Ridge. *Journal of Physical Oceanography, 42*(7), 1242-1248. doi:10.1175/jpo-d-11-0126.1

Liu, Q., Xie, X., Shang, X., & Chen, G. (2016). Coherent and incoherent internal tides in the southern South China Sea. *Chinese Journal of Oceanology and Limnology, 34*(6), 1374-1382. doi:10.1007/s00343-016-5171-5

Llewellyn Smith, S. G., & Young, W. R. (2002). Conversion of the Barotropic Tide. *Journal of Physical Oceanography, 32*(5), 1554-1566. doi:10.1175/1520-0485(2002)032<1554:Cotbt>2.0.Co;2

Löb, J., Köhler, J., Mertens, C., Walter, M., Li, Z., von Storch, J.-S., . . . Rhein, M. (2020). Observations of the Low-Mode Internal Tide and Its Interaction With Mesoscale Flow South of the Azores. *Journal of Geophysical Research: Oceans, 125*(11), e2019JC015879. doi:https://doi.org/10.1029/2019JC015879

MacKinnon, J. A., Alford, M. H., Sun, O., Pinkel, R., Zhao, Z., & Klymak, J. (2013). Parametric Subharmonic Instability of the Internal Tide at 29°N. *Journal of Physical Oceanography, 43*(1), 17-28. doi:10.1175/jpo-d-11-0108.1

MacKinnon, J. A., & Winters, K. B. (2005). Subtropical catastrophe: Significant loss of low-mode tidal energy at 28.9°. *Geophysical Research Letters, 32*(15). doi:10.1029/2005gl023376

MacKinnon, J. A., Zhao, Z., Whalen, C. B., Waterhouse, A. F., Trossman, D. S., Sun, O. M., . . . Alford, M. H. (2017). Climate Process Team on Internal Wave–Driven Ocean Mixing. *Bulletin of the American Meteorological Society, 98*(11), 2429-2454. doi:10.1175/bams-d-16-0030.1

Martini, K. I., Alford, M. H., Kunze, E., Kelly, S. M., & Nash, J. D. (2011). Observations of Internal Tides on the Oregon Continental Slope. *Journal of Physical Oceanography, 41*(9), 1772-1794. doi:10.1175/2011jpo4581.1

McComas, C. H., & Bretherton, F. P. (1977). Resonant interaction of oceanic internal waves. *Journal of Geophysical Research (1896-1977), 82*(9), 1397-1412. doi:10.1029/JC082i009p01397

McWilliams, J. C. (1985). Submesoscale, coherent vortices in the ocean. *Reviews of Geophysics, 23*(2), 165-182. doi:10.1029/RG023i002p00165

Melet, A., Hallberg, R., Legg, S., & Polzin, K. (2013). Sensitivity of the Ocean State to the Vertical Distribution of Internal-Tide-Driven Mixing. *Journal of Physical Oceanography, 43*(3), 602-615. doi:10.1175/jpo-d-12-055.1

Mitchum, G. T., & Chiswell, S. M. (2000). Coherence of internal tide modulations along the Hawaiian Ridge. *Journal of Geophysical Research: Oceans, 105*(C12), 28653-28661. doi:10.1029/2000jc900140

Morozov, E. G. (1995). Semidiurnal internal wave global field. *Deep Sea Research Part I: Oceanographic Research Papers, 42*(1), 135-148. doi:https://doi.org/10.1016/0967-0637(95)92886-C

Müller, M., Cherniawsky, J. Y., Foreman, M. G. G., & von Storch, J.-S. (2014). Seasonal variation of the M 2 tide. *Ocean Dynamics, 64*(2), 159-177. doi:10.1007/s10236-013-0679-0

Müller, M., Cherniawsky, J. Y., Foreman, M. G. G., & von Storch, J. S. (2012). GlobalM2internal tide and its seasonal variability from high resolution ocean

circulation and tide modeling. *Geophysical Research Letters, 39*(19), n/a-n/a. doi:10.1029/2012gl053320

Müller, P. (1976). On the diffusion of momentum and mass by internal gravity waves. *Journal of Fluid Mechanics, 77*(4), 789-823. doi:10.1017/S0022112076002899

Munk, W. (1981). Internal waves and small scale processes. *Evolution of Physical Oceanography*.

Munk, W., Cartwright, D. E., & Bullard, E. C. (1966). Tidal spectroscopy and prediction. *Philosophical Transactions of the Royal Society of London. Series A, Mathematical and Physical Sciences, 259*(1105), 533-581. doi:doi:10.1098/rsta.1966.0024

Munk, W., & Wunsch, C. (1998). Abyssal recipes II: energetics of tidal and wind mixing. *Deep Sea Research Part I: Oceanographic Research Papers, 45*(12), 1977-2010. doi:https://doi.org/10.1016/S0967-0637(98)00070-3

Munk, W., Zetler, B., & Groves, G. W. (1965). Tidal Cusps. *Geophysical Journal International, 10*(2), 211-219. doi:10.1111/j.1365-246X.1965.tb03062.x

Nagasawa, M., Hibiya, T., Niwa, Y., Watanabe, M., Isoda, Y., Takagi, S., & Kamei, Y. (2002). Distribution of fine-scale shear in the deep waters of the North Pacific obtained using expendable current profilers. *Journal of Geophysical Research: Oceans, 107*(C12), 14-11-14-17. doi:10.1029/2002jc001376

Nagasawa, M., Niwa, Y., & Hibiya, T. (2000). Spatial and temporal distribution of the wind-induced internal wave energy available for deep water mixing in the North Pacific. *Journal of Geophysical Research: Oceans, 105*(C6), 13933-13943. doi:10.1029/2000jc900019

Nash, J. D., Alford, M. H., & Kunze, E. (2005). Estimating Internal Wave Energy Fluxes in the Ocean. *Journal of Atmospheric and Oceanic Technology, 22*(10), 1551-1570. doi:10.1175/jtech1784.1

Nash, J. D., Kelly, S. M., Shroyer, E. L., Moum, J. N., & Duda, T. F. (2012). The Unpredictable Nature of Internal Tides on Continental Shelves. *Journal of Physical Oceanography, 42*(11), 1981-2000. doi:10.1175/jpo-d-12-028.1

Nash, J. D., Kunze, E., Lee, C. M., & Sanford, T. B. (2006). Structure of the Baroclinic Tide Generated at Kaena Ridge, Hawaii. *Journal of Physical Oceanography, 36*(6), 1123-1135. doi:10.1175/jpo2883.1

Nash, J. D., Kunze, E., Toole, J. M., & Schmitt, R. W. (2004). Internal Tide Reflection and Turbulent Mixing on the Continental Slope. *Journal of Physical Oceanography, 34*(5), 1117-1134. doi:10.1175/1520-0485(2004)034<1117:Itratm>2.0.Co;2

Nash, J. D., Shroyer, E. L., Kelly, S. M., Inall, M. E., Duda, T. F., Levine, M. D., . . . Musgrave, R. C. (2012). Are Any Coastal Internal Tides Predictable? *Oceanography, 25*. doi:https://doi.org/10.5670/oceanog.2012.44

Nikurashin, M., & Ferrari, R. (2010). Radiation and Dissipation of Internal Waves Generated by Geostrophic Motions Impinging on Small-Scale Topography: Theory. *Journal of Physical Oceanography, 40*(5), 1055-1074. doi:10.1175/2009jpo4199.1

Nikurashin, M., & Ferrari, R. (2011). Global energy conversion rate from geostrophic flows into internal lee waves in the deep ocean. *Geophysical Research Letters, 38*(8). doi:10.1029/2011gl046576

Niwa, Y., & Hibiya, T. (1997). Nonlinear processes of energy transfer from traveling hurricanes to the deep ocean internal wave field. *Journal of Geophysical Research: Oceans, 102*(C6), 12469-12477. doi:10.1029/97jc00588

Nycander, J. (2005). Generation of internal waves in the deep ocean by tides. *Journal of Geophysical Research: Oceans, 110*(C10). doi:10.1029/2004jc002487

Olbers, D. (1976). Nonlinear energy transfer and the energy balance of the internal wave field in the deep ocean. *Journal of Fluid Mechanics, 74*(2), 375-399. doi:10.1017/S0022112076001857

Olbers, D. (1981). The Propagation of Internal Waves in a Geostrophic Current. *Journal of Physical Oceanography, 11*(9), 1224-1233. doi:10.1175/1520-0485(1981)011<1224:Tpoiwi>2.0.Co;2

Olbers, D. (1983). Models of the oceanic internal wave field. *Reviews of Geophysics, 21*(7), 1567-1606. doi:10.1029/RG021i007p01567

Olbers, D., & Eden, C. (2016). Revisiting the Generation of Internal Waves by Resonant Interaction with Surface Waves. *Journal of Physical Oceanography, 46*(8), 2335-2350. doi:10.1175/jpo-d-15-0064.1

Olbers, D., Pollmann, F., & Eden, C. (2020). On PSI Interactions in Internal Gravity Wave Fields and the Decay of Baroclinic Tides. *Journal of Physical Oceanography, 50*(3), 751-771. doi:10.1175/jpo-d-19-0224.1

Olbers, D., Willebrand, J., & Eden, C. (2012). *Ocean Dynamics* (Vol. 1): Springer-Verlag Berlin Heidelberg.

Park, J.-H., & Watts, D. R. (2006). Internal Tides in the Southwestern Japan/East Sea. *Journal of Physical Oceanography, 36*(1), 22-34. doi:10.1175/jpo2846.1

Pawlowicz, R., Beardsley, B., & Lentz, S. (2002). Classical tidal harmonic analysis including error estimates in MATLAB using T_TIDE. *Computers & Geosciences, 28*(8), 929-937. doi:https://doi.org/10.1016/S0098-3004(02)00013-4

Pickering, A., Alford, M. H., Nash, J., Rainville, L., Buijsman, M., Ko, D. S., & Lim, B. (2015). Structure and Variability of Internal Tides in Luzon Strait*. *Journal of Physical Oceanography, 45*(6), 1574-1594. doi:10.1175/jpo-d-14-0250.1

Pollmann, F., Nycander, J., Eden, C., & Olbers, D. (2019). Resolving the horizontal direction of internal tide generation. *Journal of Fluid Mechanics, 864*, 381-407. doi:10.1017/jfm.2019.9

Polzin, K. L., Toole, J. M., Ledwell, J. R., & Schmitt, R. W. (1997). Spatial Variability of Turbulent Mixing in the Abyssal Ocean. *Science, 276*(5309), 93. doi:10.1126/science.276.5309.93

Ponte, A. L., & Klein, P. (2015). Incoherent signature of internal tides on sea level in idealized numerical simulations. *Geophysical Research Letters, 42*(5), 1520-1526. doi:doi:10.1002/2014GL062583

Price, J. F. (1981). Upper Ocean Response to a Hurricane. *Journal of Physical Oceanography, 11*(2), 153-175. doi:10.1175/1520-0485(1981)011<0153:Uortah>2.0.Co;2

Price, J. F. (1983). Internal Wave Wake of a Moving Storm. Part I. Scales, Energy Budget and Observations. *Journal of Physical Oceanography, 13*(6), 949-965. doi:10.1175/1520-0485(1983)013<0949:Iwwoam>2.0.Co;2

Qi, H., De Szoeke, R. A., Paulson, C. A., & Eriksen, C. C. (1995). The Structure of Near-Inertial Waves during Ocean Storms. *Journal of Physical Oceanography, 25*(11), 2853-2871. doi:10.1175/1520-0485(1995)025<2853:Tsoniw>2.0.Co;2

R. Stephenson Jr., G., Hopkins, J. E., Mattias Green, J. A., Inall, M. E., & Palmer, M. R. (2015). Baroclinic energy flux at the continental shelf edge modified by wind-mixing. *Geophysical Research Letters, 42*(6), 1826-1833. doi:10.1002/2014gl062627

Rainville, L., Johnston, T. M. S., Carter, G. S., Merrifield, M. A., Pinkel, R., Worcester, P. F., & Dushaw, B. D. (2010). Interference Pattern and Propagation of the M2 Internal Tide South of the Hawaiian Ridge. *Journal of Physical Oceanography, 40*(2), 311-325. doi:10.1175/2009jpo4256.1

Rainville, L., & Pinkel, R. (2004). Observations of Energetic High-Wavenumber Internal Waves in the Kuroshio. *Journal of Physical Oceanography, 34*(7), 1495-1505. doi:10.1175/1520-0485(2004)034<1495:Ooehiw>2.0.Co;2

Rainville, L., & Pinkel, R. (2006). Propagation of Low-Mode Internal Waves through the Ocean. *Journal of Physical Oceanography, 36*(6), 1220-1236. doi:10.1175/jpo2889.1

Ray, R. D. (2013). Precise comparisons of bottom-pressure and altimetric ocean tides. *Journal of Geophysical Research: Oceans, 118*(9), 4570-4584. doi:10.1002/jgrc.20336

Ray, R. D., & Cartwright, D. E. (2001). Estimates of internal tide energy fluxes from Topex/Poseidon Altimetry: Central North Pacific. *Geophysical Research Letters, 28*(7), 1259-1262. doi:10.1029/2000gl012447

Ray, R. D., & Mitchum, G. T. (1996). Surface manifestation of internal tides generated near Hawaii. *Geophysical Research Letters, 23*(16), 2101-2104. doi:doi:10.1029/96GL02050

Ray, R. D., & Zaron, E. D. (2011). Non-stationary internal tides observed with satellite altimetry. *Geophysical Research Letters, 38*(17). doi:10.1029/2011gl048617

Ray, R. D., & Zaron, E. D. (2015). M2 Internal Tides and Their Observed Wavenumber Spectra from Satellite Altimetry*. *Journal of Physical Oceanography, 46*(1), 3-22. doi:10.1175/jpo-d-15-0065.1

Richman, J. G., Arbic, B. K., Shriver, J. F., Metzger, E. J., & Wallcraft, A. J. (2012). Inferring dynamics from the wavenumber spectra of an eddying global ocean model with embedded tides. *Journal of Geophysical Research: Oceans, 117*(C12). doi:10.1029/2012jc008364

Rimac, A., Storch, J.-S. v., & Eden, C. (2016). The Total Energy Flux Leaving the Ocean's Mixed Layer. *Journal of Physical Oceanography, 46*(6), 1885-1900. doi:10.1175/jpo-d-15-0115.1

Rimac, A., von Storch, J.-S., Eden, C., & Haak, H. (2013). The influence of high-resolution wind stress field on the power input to near-inertial motions in the ocean. *Geophysical Research Letters, 40*(18), 4882-4886. doi:doi:10.1002/grl.50929

Rocha, C. B., Wagner, G. L., & Young, W. R. (2018). Stimulated generation: extraction of energy from balanced flow by near-inertial waves. *Journal of Fluid Mechanics, 847*, 417-451. doi:10.1017/jfm.2018.308

Saidi, J. S. (2011). *Experimental investigation of 2D and 3D internal wave fields.* (Master thesis). Massachusetts Institute of Technology,

Samelson, R. M. (1998). Large-Scale Circulation with Locally Enhanced Vertical Mixing*. *Journal of Physical Oceanography, 28*(4), 712-726. doi:10.1175/1520-0485(1998)028<0712:Lscwle>2.0.Co;2

Sanford, T. B., Black, P. G., Haustein, J. R., Feeney, J. W., Forristall, G. Z., & Price, J. F. (1987). Ocean Response to a Hurricane. Part I: Observations. *Journal of Physical Oceanography, 17*(11), 2065-2083. doi:10.1175/1520-0485(1987)017<2065:Ortahp>2.0.Co;2

Sanford, T. B., Price, J. F., & Girton, J. B. (2011). Upper-Ocean Response to Hurricane Frances (2004) Observed by Profiling EM-APEX Floats*. *Journal of Physical Oceanography, 41*(6), 1041-1056. doi:10.1175/2010jpo4313.1

Sanford, T. B., Price, J. F., Girton, J. B., & Webb, D. C. (2007). Highly resolved observations and simulations of the ocean response to a hurricane. *Geophysical Research Letters, 34*(13). doi:10.1029/2007gl029679

Sarkar, S., & Scotti, A. (2017). From Topographic Internal Gravity Waves to Turbulence. *Annual Review of Fluid Mechanics, 49*(1), 195-220. doi:10.1146/annurev-fluid-010816-060013

Savage, A. C., Arbic, B. K., Alford, M. H., Ansong, J. K., Farrar, J. T., Menemenlis, D., . . . Zamudio, L. (2017). Spectral decomposition of internal gravity wave sea surface height in global models. *Journal of Geophysical Research: Oceans, 122*(10), 7803-7821. doi:10.1002/2017jc013009

Savage, A. C., Waterhouse, A. F., & Kelly, S. M. (2020). Internal tide nonstationarity and wave-mesoscale interactions in the Tasman Sea. *Journal of Physical Oceanography*, 1-52. doi:10.1175/jpo-d-19-0283.1

Scott, R. B., Goff, J. A., Naveira Garabato, A. C., & Nurser, A. J. G. (2011). Global rate and spectral characteristics of internal gravity wave generation by geostrophic flow over topography. *Journal of Geophysical Research: Oceans, 116*(C9). doi:10.1029/2011jc007005

Shakespeare, C. J., & McC. Hogg, A. (2018). The Life Cycle of Spontaneously Generated Internal Waves. *Journal of Physical Oceanography, 48*(2), 343-359. doi:10.1175/jpo-d-17-0153.1

Sharples, J., Tweddle, J. F., Mattias Green, J. A., Palmer, M. R., Kim, Y.-N., Hickman, A. E., . . . Krivtsov, V. (2007). Spring-neap modulation of internal tide mixing and vertical nitrate fluxes at a shelf edge in summer. *Limnology and Oceanography, 52*(5), 1735-1747. doi:10.4319/lo.2007.52.5.1735

Shay, L. K., Black, P. G., Mariano, A. J., Hawkins, J. D., & Elsberry, R. L. (1992). Upper ocean response to Hurricane Gilbert. *Journal of Geophysical Research: Oceans, 97*(C12), 20227-20248. doi:10.1029/92jc01586

Shriver, J. F., Richman, J. G., & Arbic, B. K. (2014). How stationary are the internal tides in a high-resolution global ocean circulation model? *Journal of Geophysical Research: Oceans, 119*(5), 2769-2787. doi:10.1002/2013jc009423

Silverthorne, K. E., & Toole, J. M. (2009). Seasonal Kinetic Energy Variability of Near-Inertial Motions. *Journal of Physical Oceanography, 39*(4), 1035-1049. doi:10.1175/2008jpo3920.1

Simmons, H. L., & Alford, M. H. (2012). Simulating the Long-Range Swell of Internal Waves Generated by Ocean Storms. *Oceanography, 25*(2), 30-41. doi:10.5670/oceanog.2012.39

Simmons, H. L., Hallberg, R. W., & Arbic, B. K. (2004). Internal wave generation in a global baroclinic tide model. *Deep Sea Research Part II: Topical Studies in Oceanography, 51*(25), 3043-3068. doi:https://doi.org/10.1016/j.dsr2.2004.09.015

Simmons, H. L., Jayne, S. R., St. Laurent, L. C., & Weaver, A. J. (2004). Tidally driven mixing in a numerical model of the ocean general circulation. *Ocean Modelling, 6*(3), 245-263. doi:https://doi.org/10.1016/S1463-5003(03)00011-8

St. Laurent, L. C., & Garrett, C. (2002). The Role of Internal Tides in Mixing the Deep Ocean. *Journal of Physical Oceanography, 32*(10), 2882-2899. doi:10.1175/1520-0485(2002)032<2882:Troiti>2.0.Co;2

St. Laurent, L. C., & Simmons, H. (2006). Estimates of Power Consumed by Mixing in the Ocean Interior. *Journal of Climate, 19*(19), 4877-4890. doi:10.1175/jcli3887.1

Sutherland, B. R. (2016). Excitation of superharmonics by internal modes in non-uniformly stratified fluid. *Journal of Fluid Mechanics, 793*, 335-352. doi:10.1017/jfm.2016.108

Sutherland, B. R., & Jefferson, R. (2020). Triad resonant instability of horizontally periodic internal modes. *Physical Review Fluids, 5*(3), 034801. doi:10.1103/PhysRevFluids.5.034801

Taylor, S., & Straub, D. (2015). Forced Near-Inertial Motion and Dissipation of Low-Frequency Kinetic Energy in a Wind-Driven Channel Flow. *Journal of Physical Oceanography, 46*(1), 79-93. doi:10.1175/jpo-d-15-0060.1

Terker, S. R., Girton, J. B., Kunze, E., Klymak, J. M., & Pinkel, R. (2014). Observations of the internal tide on the California continental margin near Monterey Bay. *Continental Shelf Research, 82*, 60-71. doi:https://doi.org/10.1016/j.csr.2014.01.017

Thompson, K. R., Marsden, R. F., & Wright, D. G. (1983). Estimation of Low-Frequency Wind Stress Fluctuations over the Open Ocean. *Journal of Physical Oceanography, 13*(6), 1003-1011. doi:10.1175/1520-0485(1983)013<1003:Eolfws>2.0.Co;2

Tsai, Y., Chern, C.-S., & Wang, J. (2008). The upper ocean response to a moving typhoon. *Journal of Oceanography, 64*(1), 115-130. doi:10.1007/s10872-008-0009-1

Turner, J. S. (1973). *Buoyancy Effects in Fluids*. Cambridge: Cambridge University Press.

van Haren, H. (2004). Incoherent internal tidal currents in the deep ocean. *Ocean Dynamics, 54*(1), 66-76. doi:10.1007/s10236-003-0083-2

van Haren, H., Maas, L., & van Aken, H. (2002). On the nature of internal wave spectra near a continental slope. *Geophysical Research Letters, 29*(12), 57-51-57-53. doi:10.1029/2001gl014341

Vanneste, J. (2013). Balance and Spontaneous Wave Generation in Geophysical Flows. *Annual Review of Fluid Mechanics, 45*(1), 147-172. doi:10.1146/annurev-fluid-011212-140730

Vic, C., Garabato, A. C. N., Green, J. A. M., Spingys, C., Forryan, A., Zhao, Z., & Sharples, J. (2018). The Lifecycle of Semidiurnal Internal Tides over the Northern Mid-Atlantic Ridge. *Journal of Physical Oceanography, 48*(1), 61-80. doi:10.1175/jpo-d-17-0121.1

von Storch, J.-S., Sasaki, H., & Marotzke, J. (2007). Wind-Generated Power Input to the Deep Ocean: An Estimate Using a 1/10° General Circulation Model. *Journal of Physical Oceanography, 37*(3), 657-672. doi:10.1175/jpo3001.1

Walter, M., Köhler, J., Löb, J., Loureiro, C., Stiehler, J., Gemmrich, H., . . . Reitz, T. (2019). RV POSEIDON 523 Cruise Report / Fahrtbericht Malaga (Spain) 02.05.2018 Ponta Delgada (Azores) 23.05.2018 POS523 – ENERGY TRANSFER II. *Zentrum für Marine Umweltwissenschaften, Universität Bremen*. doi:10.3289/CR_POS523

Walter, M., Köhler, J., Löb, J., Sukjikh, N., Böke, W., Münzner, F., . . . Rümmler, S. (2018). RV POSEIDON 516 [POS516] Cruise Report / Fahrtbericht, Ponta Delgada (Azores) 29.07.2017 - Ponta Delgada (Azores) 18.08.2017, POS516 – ENERGY TRANSFER . *Zentrum für Marine Umweltwissenschaften, Universität Bremen*. doi:10.3289/CR_POS516

Walter, M., & Mertens, C. (2013). Mid-depth mixing linked to North Atlantic Current variability. *Geophysical Research Letters, 40*(18), 4869-4875. doi:10.1002/grl.50936

Walter, M., Mertens, C., & Rhein, M. (2005). Mixing estimates from a large-scale hydrographic survey in the North Atlantic. *Geophysical Research Letters, 32*(13). doi:10.1029/2005gl022471

Walter, M., Mertens, C., Stöber, U., German, C. R., Yoerger, D. R., Sültenfuß, J., . . . Baker, E. T. (2010). Rapid dispersal of a hydrothermal plume by turbulent mixing. *Deep Sea Research Part I: Oceanographic Research Papers, 57*(8), 931-945. doi:https://doi.org/10.1016/j.dsr.2010.04.010

Ward, M. L., & Dewar, W. K. (2010). Scattering of gravity waves by potential vorticity in a shallow-water fluid. *Journal of Fluid Mechanics, 663*, 478-506. doi:10.1017/S0022112010003721

Watanabe, M., & Hibiya, T. (2002). Global estimates of the wind-induced energy flux to inertial motions in the surface mixed layer. *Geophysical Research Letters, 29*(8), 64-61-64-63. doi:doi:10.1029/2001GL014422

Waterhouse, A. F., Kelly, S. M., Zhao, Z., MacKinnon, J. A., Nash, J. D., Simmons, H., . . . Pinkel, R. (2018). Observations of the Tasman Sea Internal Tide Beam. *Journal of Physical Oceanography, 48*(6), 1283-1297. doi:10.1175/jpo-d-17-0116.1

Waterhouse, A. F., MacKinnon, J. A., Nash, J. D., Alford, M. H., Kunze, E., Simmons, H. L., . . . Lee, C. M. (2014). Global Patterns of Diapycnal Mixing from Measurements of the Turbulent Dissipation Rate. *Journal of Physical Oceanography, 44*(7), 1854-1872. doi:10.1175/jpo-d-13-0104.1

Webb, D. J., & Suginohara, N. (2001). Vertical mixing in the ocean. *Nature, 409*(6816), 37-37. doi:10.1038/35051171

Weller, R. A. (1982). The Relation of Near-Inertial Motions Observed in the Mixed layer During the JASIN (1978) Experiment to the Local Wind Stress and to the Quasi-Geostrophic Flow Field. *Journal of Physical Oceanography, 12*(10), 1122-1136. doi:10.1175/1520-0485(1982)012<1122:TRONIM>2.0.CO;2

Whalen, C. B., MacKinnon, J. A., & Talley, L. D. (2018). Large-scale impacts of the mesoscale environment on mixing from wind-driven internal waves. *Nature Geoscience, 11*(11), 842-847. doi:10.1038/s41561-018-0213-6

Whalen, C. B., Talley, L. D., & MacKinnon, J. A. (2012). Spatial and temporal variability of global ocean mixing inferred from Argo profiles. *Geophysical Research Letters, 39*(18). doi:10.1029/2012gl053196

Wilson, J. F. (2003). *Dynamics of offshore structures*: John Wiley & Sons.

Worcester, P. F., Dzieciuch, M. A., Mercer, J. A., Andrew, R. K., Dushaw, B. D., Baggeroer, A. B., . . . Wage, K. E. (2013). The North Pacific Acoustic Laboratory deep-water acoustic propagation experiments in the Philippine Sea. *The Journal of the Acoustical Society of America, 134*(4), 3359-3375. doi:10.1121/1.4818887

Wright, C. J., Scott, R. B., Ailliot, P., & Furnival, D. (2014). Lee wave generation rates in the deep ocean. *Geophysical Research Letters, 41*(7), 2434-2440. doi:10.1002/2013gl059087

Wunsch, C. (1975). Internal tides in the ocean. *Reviews of Geophysics, 13*(1), 167-182. doi:10.1029/RG013i001p00167

Wunsch, C., & Ferrari, R. (2004). Vertical Mixing, Energy, and the General Circulation of the Oceans. *Annual Review of Fluid Mechanics, 36*(1), 281-314. doi:10.1146/annurev.fluid.36.050802.122121

Xie, J. H., & Vanneste, J. (2015). A generalised-Lagrangian-mean model of the interactions between near-inertial waves and mean flow. *Journal of Fluid Mechanics, 774*, 143-169. doi:10.1017/jfm.2015.251

Yang, B., & Hou, Y. (2014). Near-inertial waves in the wake of 2011 Typhoon Nesat in the northern South China Sea. *Acta Oceanologica Sinica, 33*(11), 102-111. doi:10.1007/s13131-014-0559-6

Young, W., & Ben Jelloul, M. (1997). Propagation of near-inertial oscillations through a geostrophic flow. *Journal of Marine Research, 55*, 735-766. doi:10.1357/0022240973224283

Zaron, E. D. (2017). Mapping the nonstationary internal tide with satellite altimetry. *Journal of Geophysical Research: Oceans, 122*(1), 539-554. doi:10.1002/2016jc012487

Zaron, E. D., & Egbert, G. D. (2014). Time-Variable Refraction of the Internal Tide at the Hawaiian Ridge. *Journal of Physical Oceanography, 44*(2), 538-557. doi:10.1175/jpo-d-12-0238.1

Zedler, S. E. (2009). Simulations of the Ocean Response to a Hurricane: Nonlinear Processes. *Journal of Physical Oceanography, 39*(10), 2618-2634. doi:10.1175/2009jpo4062.1

Zhai, X., Greatbatch, R. J., & Eden, C. (2007). Spreading of near-inertial energy in a 1/12° model of the North Atlantic Ocean. *Geophysical Research Letters, 34*(10). doi:10.1029/2007gl029895

Zhai, X., Greatbatch, R. J., Eden, C., & Hibiya, T. (2009). On the Loss of Wind-Induced Near-Inertial Energy to Turbulent Mixing in the Upper Ocean. *Journal of Physical Oceanography, 39*(11), 3040-3045. doi:10.1175/2009jpo4259.1

Zhai, X., Greatbatch, R. J., & Zhao, J. (2005). Enhanced vertical propagation of storm-induced near-inertial energy in an eddying ocean channel model. *Geophysical Research Letters, 32*(18). doi:10.1029/2005gl023643

Zhai, X., Johnson, H. L., Marshall, D. P., & Wunsch, C. (2012). On the Wind Power Input to the Ocean General Circulation. *Journal of Physical Oceanography, 42*(8), 1357-1365. doi:10.1175/jpo-d-12-09.1

Zhao, Z. (2018). The Global Mode-2 M2 Internal Tide. *Journal of Geophysical Research: Oceans, 0*(0). doi:doi:10.1029/2018JC014475

Zhao, Z., & Alford, M. H. (2009). New Altimetric Estimates of Mode-1 M2 Internal Tides in the Central North Pacific Ocean. *Journal of Physical Oceanography, 39*(7), 1669-1684. doi:10.1175/2009jpo3922.1

Zhao, Z., Alford, M. H., Girton, J., Johnston, T. M. S., & Carter, G. (2011). Internal tides around the Hawaiian Ridge estimated from multisatellite altimetry. *Journal of Geophysical Research: Oceans, 116*(C12). doi:10.1029/2011jc007045

Zhao, Z., Alford, M. H., & Girton, J. B. (2012). Mapping low-mode internal tides from multisatellite altimetry. *Oceanography 25(2):42–51*. doi: https://doi.org/10.5670/oceanog.2012.40.

Zhao, Z., Alford, M. H., Girton, J. B., Rainville, L., & Simmons, H. L. (2016). Global Observations of Open-Ocean Mode-1 M2Internal Tides. *Journal of Physical Oceanography, 46*(6), 1657-1684. doi:10.1175/jpo-d-15-0105.1

Zhao, Z., Alford, M. H., MacKinnon, J. A., & Pinkel, R. (2010). Long-Range Propagation of the Semidiurnal Internal Tide from the Hawaiian Ridge. *Journal of Physical Oceanography, 40*(4), 713-736. doi:10.1175/2009jpo4207.1

Zhao, Z., & D'Asaro, E. (2011). A perfect focus of the internal tide from the Mariana Arc. *Geophysical Research Letters, 38*(14). doi:10.1029/2011gl047909

Zilberman, N. V., Merrifield, M. A., Carter, G. S., Luther, D. S., Levine, M. D., & Boyd, T. J. (2011). Incoherent Nature of M2 Internal Tides at the Hawaiian Ridge. *Journal of Physical Oceanography, 41*(11), 2021-2036. doi:10.1175/jpo-d-10-05009.1